ELECTROMAGNETIC FIELD ANALYSIS OF SPHERICALLY GEOMETRICAL CAVITIES USING THE FINITE-DIFFERENCE TIME-DOMAIN METHOD

EKAJIT KHOOMWONG

A THESIS SUBMITTED IN PARTIAL FULFILLMENT
OF THE REQUIREMENT FOR THE DEGREE OF
MASTER OF ENGINEERING IN ELECTRICAL ENGINEERING
SCHOOL OF GRADUATE STUDIES
KING MONGKUT'S INSTITUTE OF TECHNOLOGY LADKRABANG
1999

ISBN 974-622-570-7

หัวข้อวิทยานิพนธ์	การวิเคราะห์สนามแม่เหล็กไฟฟ้าภายในคาวิตี้ตัวนำที่มีรูปร่างเป็นทรงกลม และส่วนของทรงกลม โดยวิธีผลต่างสืบเนื่องเชิงเวลา
นักศึกษา	นายเอกจิต คุ้มวงศ์
รหัสประจำตัว	40061032
ปริญญา	วิศวกรรมศาสตรมหาบัณฑิต
สาขาวิชา	วิศวกรรมไฟฟ้า
พ.ศ.	2542
อาจารย์ผู้ควบคุมวิทยานิพนธ์	รศ.ดร.โมไนย ไกรฤกษ์

บทคัดย่อ

วิทยานิพนธ์นี้เป็นการศึกษาหลักการ และการประยุกต์ใช้วิธีการเชิงเลขที่เรียกว่า ผลต่างสืบเนื่องเชิงเวลา (Finite-Difference Time-Domain Method) เพื่อวิเคราะห์หาสนามแม่เหล็กไฟฟ้าภายในคาวิตี้สามรูปแบบ คือ คาวิตี้ตัวนำที่มีรูปร่างเป็นส่วนของทรงกลม คาวิตี้ตัวนำทรงกลมสองใบซ้อนกันปิดด้วยส่วนของกรวยตัวนำ และคาวิตี้ตัวนำทรงกลมทั้งใบ ในการวิเคราะห์เชิงเลขนั้นได้ทำในระบบพิกัดทรงกลม และนำเสนอเงื่อนไขการแพร่กระจายคลื่นขึ้นใหม่ รวมถึงสมการเกณฑ์เสถียรภาพ ในส่วนของการวิเคราะห์นั้นได้กระทำทั้งในกรณีที่ไม่มีแบบจำลองโพรบซึ่งถือว่าเป็นบริเวณที่ปราศจากแหล่งกำเนิด และกรณีที่มีแบบจำลองโพรบถือว่าเป็นบริเวณที่มีแหล่งกำเนิด สำหรับแบบจำลองโพรบ และร่องบนผิวตัวนำ ได้นำเสนอไว้ทั้งแบบจำลองโดยละเอียด และแบบจำลองโดยประมาณ จากนั้นนำแบบจำลองข้างต้นไปสร้างเป็นแบบจำลองสายอากาศร่องเดี่ยว และร่องแถวลำดับบนผิวคาวิตี้ตัวนำครึ่งทรงกลม ซึ่งการวิเคราะห์สายอากาศทำโดยหาพารามิเตอร์สองตัว คือ อิมพีแดนซ์ขาเข้าของสายอากาศ และแบบรูปการแพร่กระจายคลื่น ในส่วนของแบบรูปการแพร่กระจายคลื่นสามารถหาได้จากสนามระยะใกล้โดยใช้วิธีการแปลงสนามจากระยะใกล้ไประยะไกลเชิงความถี่ ผลจากการคำนวณเชิงเลขบางส่วนถูกนำไปเปรียบกับผลที่ได้จากวิธีเชิงวิเคราะห์และผลจากการทดลอง

Thesis Title	Electromagnetic Field Analysis of the Spherically Geometrical Cavities Using the Finite-Difference Time-Domain Method
Student	Mr.Ekajit Khoomwong
Student ID	40061032
Degree	Master of Engineering
Programme	Electrical Engineering
Year	1999
Thesis Advisor	Assoc.Prof.Dr.Monai Krairiksh

ABSTRACT

This thesis presents the implementations of the finite-difference time-domain (FD-TD) method to numerically analyze electromagnetic field inside spherically geometrical cavities, such as a conducting spherical segmented cavity, a concentric conducting spherical cavity enclosed by a conducting conical surface and a conducting spherical cavity. The FD-TD algorithm is calculated in spherical coordinates. Additionally, the radiation boundary conditions and the numerical stability criterion are formulated. The numerical computations are simulated for two cases, source and source-free region. The effects of the probe excitation are considered in case of source region. Two approaches in probe and slot modeling, viz., detailed and approximate models, which are utilizing geometry of fine resolutions and near-field physical assumptions, respectively, are also introduced. Then, the models are integrated to analyze an antenna model, a slot and slot array on a hemispherical cavity. The analysis is done by determining two parameters of the antenna, input impedance and radiation pattern. Radiation patterns can be obtained from the near-field results by using the frequency-domain near-to-far field transformation. Some of the numerical results are compared with analytical and experimental ones.

ACKNOWLEDGEMENT

I would like to take this opportunity to express my gratitude to many individuals who concerned in the completion of this thesis.

First of all, I am so grateful to my advisor, Associate Professor Monai Krairiksh, who has been giving me many helpful suggestions and stimulating the progress of this research, since the first day I have presented with it. I also appreciate his kindness in accepting me as one of his advisees.

I would like to thank to Associate Professor Jun-ichi Takada of Tokyo Institute of Technology whom I have discussed with. Although there are few times of discussions, the obtained ideas can be greatly expanded, later. Also, I would like to acknowledge Professor Toshio Wakabayashi of Tokai University who introduced the FD-TD method to us at our laboratory.

I would like to extend my sincere dedication to Associate Professor Wiwat Kiranon who gave me some recommendations in the past Seminar MII's hours. Also, I am grateful to Associate Professor Charray Surawatpunya for some useful numerical techniques that he taught. Additionally, I would like to acknowledge Associate Professor Tawil Paungma, Associate Professor Nuttaka Homsup and Assistant Professor Sompol Kosulvit as the committee examiners.

Conclusively, I would like to distribute the dedication to all of my teachers along my student life.

I would like to express my gratitude to my senior, Mr.Komsak Meksamoot, who gave many discussions with his kindness. Also, to an unforgetable person, Mr.Chuwong Phongcharoenpanich who has introduced me to the FD-TD method, then I could conduct the advancements in this thesis. I also appreciate miscellaneous things that he has done for me.

I would like to thank all of my friends in Monai's laboratory for proof-reading and preparing the manuscript of this thesis. I also appreciate their sincere friendship and generousity.

Above all, I am so grateful to my parents who have been supporting me for so long. For me, they are the greatest donors that I have ever known.

Ekajit Khoomwong

TABLE OF CONTENTS

TABLE OF CONTENTS (to)

LIST OF TABLES

LIST OF FIGURES

Fig. page

LIST OF FIGURES (to)

Fig. page

LIST OF FIGURES (to)

Fig. page

Chapter 1

Introduction

As an introductory chapter, the background of the Finite-Difference Time-Domain (FD-TD) method is firstly introduced, including some interesting up-to-date applications and references. Then, the scope of this thesis is outlined chapter by chapter.

1.1 Background of the FD-TD Method

For about three decades, the FD-TD method has been being advanced its applications by many researchers who interested and believed in it. K. S. Yee [1], the pioneer, introduced the idea of using numerical finite-difference approximation for solving Maxwell's equations in rectangular coordinates. The derived algorithm is firstly illustrated in the two-dimensional problem by injecting the plane wave in the conducting box with the conducting cylindrical obstacle at the center of the solution region. Because the simulation is bounded within the conducting box, the FD-TD method was unpopular, in that time. After that, many explorers have been conducting advancements in this method permitting open-region applications. A. Taflove is the dominant one who substantially developed the FD-TD method by improving the stability criterion formulation [2] and applying this method to analyze several problems [3]-[4], subsequently. R. Holland has also extended this method to the problem in three dimensions, referred to as THREDE code [5]-[6]. He also proposed the so-called THREDS [7], which will be applied in this thesis.

Presently, there are many active research areas involving the FD-TD method. For example, microwave devices [8], digital signal processing techniques [9] and radiating objects [10], and many more works are gathered and summarized in [11].

1.2 Scope of the Thesis

The main objective of this thesis is to rigorously derive the FD-TD algorithm in spherical coordinates. The obtained algorithm is firstly applied to model cavities. Then, mathematical probe and slot models are derived. Finally, the knowledge about cavity, probe and slot modeling are applied to analyze an antenna model. The remaining chapters are outlined chapter by chapter as below.

Chapter 2 introduces three basic finite-difference schemes and the discretized-space notations. Then, the knowledge of errors and stability of the finite-difference schemes are reviewed. Finally, the finite-difference time-domain (FD-TD) method in rectangular coordinates is discussed. Some analysis on the stability criterion and the numerical dispersion are also included.

Chapter 3 shows the derivation of the FD-TD equations in spherical coordinates. The singularities of the derived algorithm are also introduced together with some means to treat them. Then, the radiation boundary conditions are derived to truncate the FD-TD problem space properly (i.e. with minimum reflected waves). The numerical stability for spherical coordinates is also derived from the known stability criterion for general curvilinear coordinates. Eventually, some numerical results are illustrated to check whether the derived FD-TD algorithm in spherical coordinates is applicable. The problems are involving the radiations of the known-solution electric and magnetic dipoles. The numerical results and the known solutions are compared.

Chapter 4 considers the modeling of cavities of spherical geometry. The numerical analysis is done in source-free region by simply assuming that all field components in the cavities simultaneously vary with time. There are three configurations of cavities considered: (1) a conducting spherical segmented cavity, (2) a concentric conducting spherical cavity enclosed by a conducting conical surface and (3) a conducting spherical cavity.

Chapter 5 presents the modeling of probe and slot models. The modeling schemes are presented for both detailed (or fine) models and approximate models. Additionally, the subgridding algorithm is introduced to relief the cost constraints due to the detailed models. As the last discussed material, the near-to-far field transformations are derived. Two transformation schemes are presented, the frequency-domain near-to-far field transformation (FD-NFFF) and the time-domain near-to-far field transformation (TD-NFFF).

Chapter 6 analyzes an antenna model, slot and slot array on a hemispherical cavity. The analysis is done by determining two parameters of the antenna: (1) input impedance, and (2) radiation pattern. The numerical results of input impedance are compared with the experimental ones.

Chapter 7 summarizes all of the materials that have been discussed in the preceding chapters.

Finally, Appendix A through Appendix D present general knowledge of vector analysis in spherical coordinates, Spherical Bessel and Associated Legendre functions and details in deriving the stability criterion and numerical dispersion, subsequently.

Chapter 2

Basis of Finite-Difference and Finite-Difference Time-Domain Method in Rectangular Coordinates

Frequently, some electromagnetic problems are too hard, or sometimes impossible, to be solved by analytical methods. For example, a boundary of a problem is unusual (looked *shapeless*) and the inside medium is inhomogeneous or anisotropic. Thus, numerical approaches are alternative means to deal with these problems efficiently. Typically, the well-known numerical techniques are method of moment, finite-element and finite-difference methods.

The methods of finite differences are the popular ones because they are easy to understand and applicable to many wide ranges of problems. In this chapter, some basic schemes of finite differences are generally introduced and a basic finite-difference time-domain method in rectangular coordinates is specifically discussed.

2.1 Finite-Difference Schemes

A finite-difference scheme is simply an approximation of a continuous derivative in terms of values at a discrete set of points. Since the further uses (construction of FD-TD equations) involve only the first derivative, the finite-difference schemes presenting here will be concerned with the first-order derivative, only. Given a plot of a function $f(x)$ shown in Fig. 2.1, the first derivative of the function at point P_O can be basically approximated by three finite-difference schemes. The first one is determining the slope of the line segment $P_R P_O$. This scheme is called *forward-difference* formula

$$f'(x_o) \approx \frac{f(x_o + \Delta x) - f(x_o)}{\Delta x}. \tag{2.1a}$$

The function $f(x_o+\Delta x)$ can also be obtained by expanding the Taylor's series around x_o in forward direction,

$$f(x_o + \Delta x) = f(x_o) + \Delta x f'(x_o) + \frac{(\Delta x)^2}{2!} f''(x_o) + \frac{(\Delta x)^3}{3!} f'''(x_o) + \dots . \tag{2.1b}$$

After rearranging the terms in (2.1b), one obtains (2.1a), which has errors due to truncation of infinite series,

$$e_f = \frac{(\Delta x)}{2!} f''(x_o) + \frac{(\Delta x)^2}{3!} f'''(x_o) + \frac{(\Delta x)^3}{4!} f^{(IV)}(x_o) + \dots , \tag{2.1c}$$

and is said having order of Δx, or simply $O(\Delta x)$. In other words, this scheme provides the first order of accuracy.

The second finite-difference scheme is called the *backward-difference* formula, found from the slope of the line segment $P_O P_L$,

$$f'(x_o) \approx \frac{f(x_o) - f(x_o - \Delta x)}{\Delta x}. \tag{2.2a}$$

Also, this can be achieved by expanding the Taylor's series around x_o in backward direction,

$$f(x_o-\Delta x)=f(x_o)-(\Delta x)f'(x_o)+\frac{(\Delta x)^2}{2!}f''(x_o)-\frac{(\Delta x)^3}{3!}f'''(x_o)+\dots . \quad (2.2b)$$

Again, by rearranging the terms in (2.2b), (2.2a) is obtained which has errors due to truncation,

$$e_b=\frac{(\Delta x)}{2!}f''(x_o)-\frac{(\Delta x)^2}{3!}f'''(x_o)+\frac{(\Delta x)^3}{4!}f^{(IV)}(x_o)-\dots , \quad (2.2c)$$

and approximately provides the first order of accuracy as in the first scheme. The final basic scheme is called the *central-difference* formula, which is simply the average of (2.1a) and (2.2a), or the slope of the line segment P_RP_L,

$$f'(x_o)\approx\frac{f(x_o+\Delta x)-f(x_o-\Delta x)}{2\Delta x}. \quad (2.3a)$$

Similar to the previous schemes, this formula can be derived from the expanded Taylor's series by subtracting (2.2b) from (2.1b), which has errors of order $(\Delta x)^2$ or simply $O(\Delta x)^2$ as,

$$e_c=\frac{(\Delta x)^3}{3!}f'''(x_o)+\frac{(\Delta x)^4}{5!}f^{(V)}(x_o)+\frac{(\Delta x)^6}{7!}f^{(VII)}(x_o)+\dots . \quad (2.3b)$$

At this point, it is evident that the central-difference scheme yields more accuracy than the previous two schemes. Generally, the higher order of the derivative can be obtained by collecting more terms in the expanded Taylor's series. However, in practical, the second-order scheme (2.3a) is mostly used because it compromises between accuracy and computational costs (e.g. computer resources and time). This scheme will be mainly used in the remainder parts of this thesis.

To apply the central-difference formula to find the solution of the function $f(x, y, z; t)$, the computational space (solution region) is subdivided into many small grid cells as shown in Fig. 2.2. From Fig. 2.2, the discrete space and time relationship can be written,

$$\left.\begin{aligned} x&=i\Delta x, & i&=0,1,2,\dots\\ y&=j\Delta y, & j&=0,1,2,\dots\\ z&=k\Delta z, & k&=0,1,2,\dots\\ t&=n\Delta t, & n&=0,1,2,\dots \end{aligned}\right\}. \quad (2.4a)$$

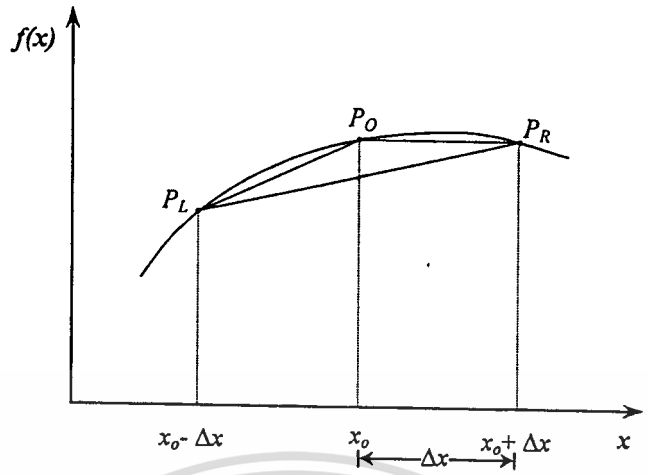

Fig. 2.1 Three basic schemes of numerical derivative of $f(x)$ at the point P_O:
The *forward difference* is the slope of the line segment $P_R P_O$.
The *backward difference* is the slope of the line segment $P_O P_L$.
The *central difference* is the slope of the line segment $P_R P_L$.

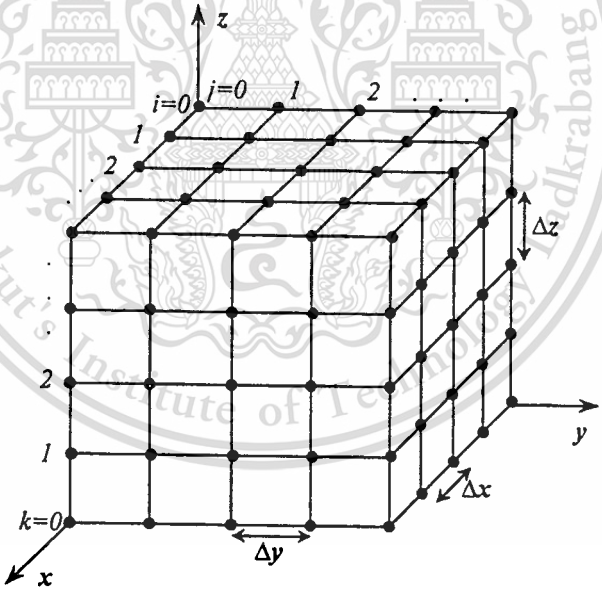

Fig. 2.2 Subdivisions of the 3-D solution region into discrete grid cells

Consider a notation for the discrete function, f, at any mesh point be,

$$f(i\Delta x, j\Delta y, k\Delta z; n\Delta t) = f(i,j,k)^n \quad (2.4b)$$

By using the above notation and (2.3a), the general space and time derivatives can be formulated as shown in the following two equations,

$$\frac{\partial f(i,j,k)^n}{\partial x} \approx \frac{f(i+1,j,k)^n - f(i-1,j,k)^n}{2\Delta x}, \quad (2.5a)$$

$$\frac{\partial f(i,j,k)^n}{\partial t} \approx \frac{f(i,j,k)^{n+1} - f(i,j,k)^{n-1}}{2\Delta t}, \tag{2.5b}$$

Equation (2.5a) shows only the space derivative with respect to x. The space derivatives with respect to y and z can be obtained by analogy.

The finite-difference methods are commonly used to solve many types of partial differential equations (PDEs), for example, parabolic PDEs, hyperbolic PDEs and elliptic PDEs. Even the application of solving the system of PDEs, such as Maxwell's equations, is known later as the finite-difference time-domain (FD-TD) method. Section 2.3 will be devoted for the basic FD-TD method in rectangular coordinates.

2.2 Errors and Stability of Finite-Difference Methods

All approximate computations always produce errors within the results obtained. The results are considered reliable and useful if the produced errors are in an acceptable level or small enough. Otherwise, they reflect meaningless results. In the finite-difference approaches, there are three main sources of errors as concluded in [12]. The first one is modeling errors. This type of errors occurs due to wrong assumptions made in achieving a mathematical model to describe or approximate a physical model. For example, the linear mathematical model is used while the behavior of a physical model is nonlinear. This will severely increase errors if the physical model is far from linearity. The second type of errors, truncation errors (or discretization errors) arise when one approximates infinite series by accounting for only the significant terms and neglecting all the less-significant terms. The best example for these, here, are the errors shown in (2.1c), (2.2c) and (2.3b). This source of errors can be reduced by decreasing the mesh sizes (i.e. Δx, Δy and Δz) and the time increment Δt. An alternative way to reduce truncation errors is using more terms (higher-order approximations) in the series expansion of derivatives. However, it is cautioned that the higher-order approximations may result in unstable computations if one applies these to the lower-order PDEs. The last source of errors, roundoff errors exist due to the fact that the computations on a digital computer can be done only with finite digits of precision. It is introduced that the only way to avoid these errors is to code all operations by using integer arithmetic but this seems impossible in most practical situations. Alternatively, roundoff errors can be minimized by relying on double-precision arithmetic. Roundoff errors almost behave the same as truncation errors except that they do in the opposite sense, which are increasing while the mesh sizes are decreasing. This means that one can not indefinitely reduce the mesh sizes. Hence, truncation errors and roundoff errors provide one optimum point where the total errors (addition of the two types of errors) is minimized, as shown in Fig. 2.3.

Since almost all of electromagnetic problems involve sinusoidal functions (e.g. sine and cosine), it is useful here to predict and compare errors due the use of the mentioned finite-difference schemes to evaluate the derivative of a sinusoidal function. This will also illustrate the nature of the described roundoff errors. Consider a pure sine function, $f(x) = sin(x)$, the function is to be evaluated the first derivative at the point $x_o = \pi/6$, by using a double-precision arithmetic. The results of total errors are shown in Fig. 2.4. From Fig. 2.4, it is clear that the central-difference scheme is the most precise of the three's. The figure also proofs that one cannot decreases Δx indefinitely because the roundoff errors effect the minus terms of the

three schemes. The optimum point can also be read from the figure that is Δx should be about 10^{-7}, for the central difference scheme. However, one may not choose the optimum point for Δx because of the computational costs as introduced in the previous section.

As mentioned before, one source of instability of finite-difference schemes is mathematical modeling errors. Another source might due to inconsistent or improper boundary conditions. The behavior of the instability is that small errors at any stage of computation producing the larger cumulative errors at the next stage. So, to determine the status of a finite-difference scheme (whether it is stable), the general equation for one-variable finite-difference scheme is given by

$$\varepsilon^{n+1} = g\varepsilon^n, \tag{2.6a}$$

where ε^n and ε^{n+1} are errors at the present and the next stage, respectively. The factor g is known as the *amplification factor*. A finite-difference scheme is considered stable if the factor g is less than or equal to unity. For the case of many independent variables the equation is given by

$$[\varepsilon]^{n+1} = [G][\varepsilon]^n, \tag{2.6b}$$

where $[G]$ is the amplification matrix. The requirement for a multi-variable finite-difference scheme to be stable is that the determinant of the matrix $[G]$ should be zero. Before one can proceed in a finite-difference calculation, it is very important to find a criterion that can be used to determine where the stable region is. Without this knowledge, it may be a hard work to find a stable point by trials and errors.

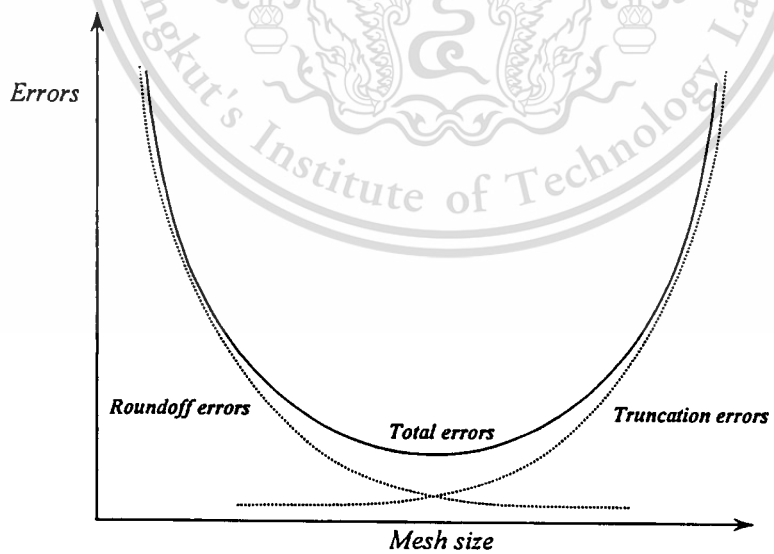

Fig. 2.3 Errors as a function of mesh size, the minimized total errors is at the intersection point of the truncation errors and roundoff errors

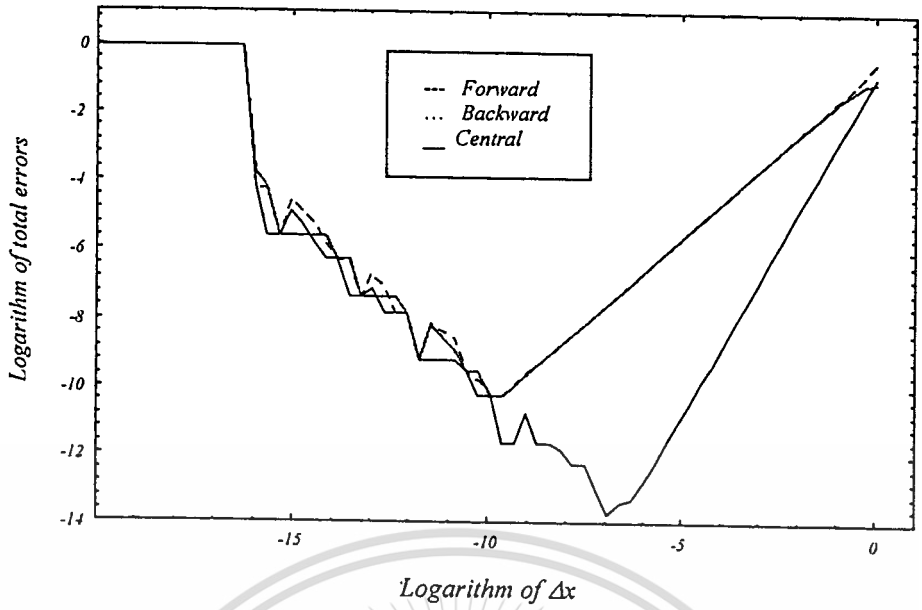

Fig. 2.4 Total errors of the finite-difference schemes as function of Δx. The finite difference schemes are used to approximate the first derivative of $sin(x)$ at $x = \pi/6$.

2.3 Finite-Difference Time-Domain Method in Rectangular Coordinates

Generally, there are three main steps to obtain a set of FD-TD algorithm for modeling electromagnetic problems. Firstly, the Maxwell's equations, in point form, must be written out in form of its corresponding three coordinate components, obtaining a system of six differential equations by using the vector identity for curl of a vector. Secondly, the obtained equations are approximated by utilizing the finite-difference schemes, as discussed in the previous section. Finally, the derivation for a stability criterion should be made to determine a stable region of FD-TD computations, which is depending on the FD-TD space and time parameters (i.e. Δx, Δy, Δz and Δt). In this section, the construction of the FD-TD equations in rectangular coordinates is introduced. This includes a stability criterion and a numerical velocity dispersion analysis. By analogy, the knowledge about this algorithm will help us to understand and obtain the finite-difference time-domain algorithm in spherical coordinates.

Consider Maxwell's equations in differential or point form,

$$\nabla \times \overline{E} = -\frac{\partial \overline{B}}{\partial t}, \tag{2.7a}$$

and

$$\nabla \times \overline{H} = \overline{J}_i + \overline{J}_c + \frac{\partial \overline{D}}{\partial t}, \tag{2.7b}$$

where $\overline{E}$ and $\overline{H}$ are electric and magnetic field intensities. $\overline{D}$ and $\overline{B}$ are electric and magnetic flux densities. $\overline{J}_i$ and $\overline{J}_c$ are impressed and conduction electric current densities, respectively. Additionally, for linear and isotropic nondispersive medium, $\overline{B}$ and $\overline{D}$ are related to $\overline{H}$ and $\overline{E}$, respectively, by simple constitutive relations as

$$\overline{B} = \mu \overline{H} \tag{2.8a}$$

$$\overline{D} = \varepsilon \overline{E}, \tag{2.8b}$$

where μ and ε are permeability and permittivity of the medium, respectively. Also, $\overline{J}_c$ relates to $\overline{E}$ as

$$\overline{J}_c = \sigma \overline{E}, \tag{2.8c}$$

where σ is conductivity.
By applying (2.8a) through (2.8c) to (2.7a) and (2.7b) and rearranging terms,

$$\mu \frac{\partial \overline{H}}{\partial t} = -\nabla \times \overline{E} \tag{2.9a}$$

and

$$\varepsilon \frac{\partial \overline{E}}{\partial t} + \sigma \overline{E} = -\overline{J}_i + \nabla \times \overline{H} \ . \tag{2.9b}$$

By using the vector identity for curl of a vector in rectangular coordinates,

$$\nabla \times \overline{A} = \overline{a}_x \left[\frac{\partial A_z}{\partial y} - \frac{\partial A_y}{\partial z} \right] + \overline{a}_y \left[\frac{\partial A_x}{\partial z} - \frac{\partial A_z}{\partial x} \right] + \overline{a}_z \left[\frac{\partial A_y}{\partial x} - \frac{\partial A_x}{\partial y} \right], \tag{2.10}$$

in conjunction with (2.9a) and (2.9b), then separating them into six field components,

$$\varepsilon \frac{\partial E_x}{\partial t} + \sigma E_x = -J_x + \frac{\partial H_z}{\partial y} - \frac{\partial H_y}{\partial z}, \tag{2.11a}$$

$$\varepsilon \frac{\partial E_y}{\partial t} + \sigma E_y = -J_y + \frac{\partial H_x}{\partial z} - \frac{\partial H_z}{\partial x}, \tag{2.11b}$$

$$\varepsilon \frac{\partial E_z}{\partial t} + \sigma E_z = -J_z + \frac{\partial H_y}{\partial x} - \frac{\partial H_x}{\partial y}, \tag{2.11c}$$

$$\mu \frac{\partial H_x}{\partial t} = \frac{\partial E_y}{\partial z} - \frac{\partial E_z}{\partial y}, \tag{2.11d}$$

$$\mu \frac{\partial H_y}{\partial t} = \frac{\partial E_z}{\partial x} - \frac{\partial E_x}{\partial z}, \tag{2.11e}$$

$$\mu \frac{\partial H_z}{\partial t} = \frac{\partial E_x}{\partial y} - \frac{\partial E_y}{\partial x}. \tag{2.11f}$$

K. S. Yee [1] introduced using the central differences to approximate the solution of the system of (2.11a) through (2.11f). The electric and magnetic fields are computed by a *leapfrog* algorithm. It is illustrated as one-dimensional wave, for example, in

Fig. 2.5. In three dimensions, the electric and magnetic fields are positioned on a grid cell as shown in Fig. 2.6.

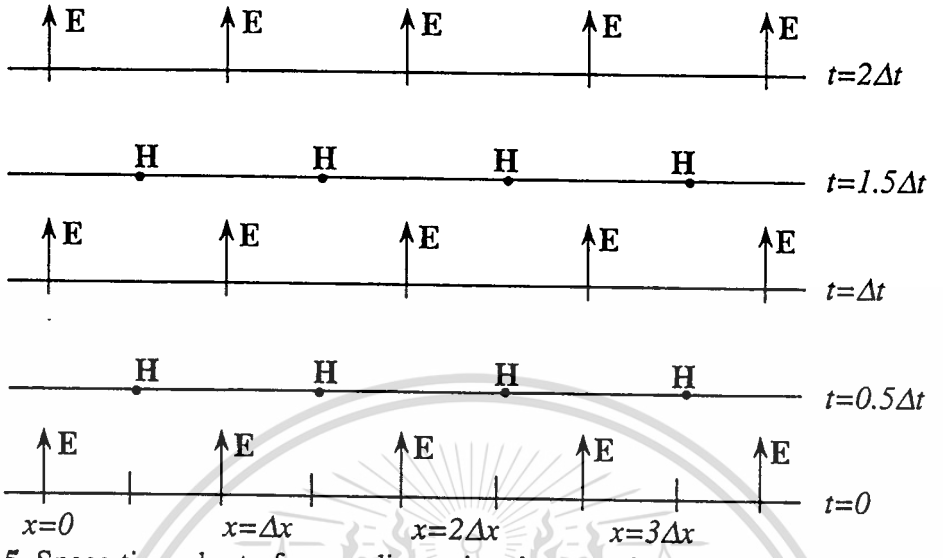

Fig. 2.5 Space-time chart of a one-dimensional wave of the Yee algorithm showing electric and magnetic fields are to be computed by the central differences for space derivatives, and by the leapfrog algorithm for time derivatives

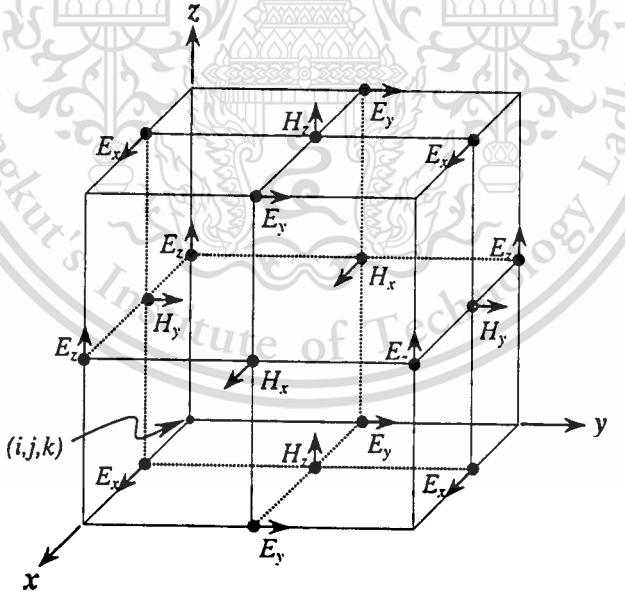

Fig. 2.6 Positions of six field components on the Yee cell

From Fig. 2.6 and (2.11a) together with the central-difference (2.5a) and (2.5b), one obtains the FD-TD equation for the electric field component E_x as

$$\varepsilon\frac{E_x(i,j,k)^{n+1/2}-E_x(i,j,k)^{n-1/2}}{\Delta t}+\frac{\sigma}{2}(E_x(i,j,k)^{n+1/2}+E_x(i,j,k)^{n-1/2})$$
$$=-J_x(i,j,k)^n+\left[\frac{H_z(i,j+1/2,k)^n-H_z(i,j-1/2,k)^n}{\Delta y}\right. \quad (2.12a)$$
$$\left.-\frac{H_y(i,j,k+1/2)^n-H_y(i,j,k-1/2)^n}{\Delta z}\right],$$

after rearranging the terms, the recurrence relation can be obtained as

$$E_x(i,j,k)^{n+1/2}=\frac{\varepsilon/\Delta t-\sigma/2}{\varepsilon/\Delta t+\sigma/2}E_x(i,j,k)^{n-1/2}$$
$$+\frac{1}{\varepsilon/\Delta t+\sigma/2}\left\{-J_x(i,j,k)^n+\frac{H_z(i,j+1/2,k)^n-H_z(i,j-1/2,k)^n}{\Delta y}\right. \quad (2.12b)$$
$$\left.-\frac{H_y(i,j,k+1/2)^n-H_y(i,j,k-1/2)^n}{\Delta z}\right\}.$$

Similarly, (2.11b) and (2.11c) can be derived to get recurrence relations, respectively, as

$$E_y(i,j,k)^{n+1/2}=\frac{\varepsilon/\Delta t-\sigma/2}{\varepsilon/\Delta t+\sigma/2}E_y(i,j,k)^{n-1/2}$$
$$+\frac{1}{\varepsilon/\Delta t+\sigma/2}\left\{-J_y(i,j,k)^n+\frac{H_x(i,j,k+1/2)^n-H_x(i,j,k-1/2)^n}{\Delta z}\right. \quad (2.12c)$$
$$\left.-\frac{H_z(i+1/2,j,k)^n-H_z(i-1/2,j,k)^n}{\Delta x}\right\},$$

$$E_z(i,j,k)^{n+1/2}=\frac{\varepsilon/\Delta t-\sigma/2}{\varepsilon/\Delta t+\sigma/2}E_z(i,j,k)^{n-1/2}$$
$$+\frac{1}{\varepsilon/\Delta t+\sigma/2}\left\{-J_z(i,j,k)^n+\frac{H_y(i+1/2,j,k)^n-H_y(i-1/2,j,k)^n}{\Delta x}\right. \quad (2.12d)$$
$$\left.-\frac{H_x(i,j+1/2,k)^n-H_x(i,j-1/2,k)^n}{\Delta y}\right\}.$$

Additionally, the σE terms in (2.11a) through (2.11c) can be approximated by averaging electric-field components at present *(n+1/2)* and previous *(n-1/2)* time steps. This method is known as *semi-implicit approximation* [13].

Similar to the derivation of the electric fields, the FD-TD equations for magnetic-field components H_x, H_y and H_z, are obtained, respectively,

$$H_x(i,j,k)^{n+1} = H_x(i,j,k)^n + \frac{\Delta t}{\mu}\left[\frac{E_y(i,j,k+1)^{n+1/2} - E_y(i,j,k)^{n+1/2}}{\Delta z} - \frac{E_z(i,j+1,k)^{n+1/2} - E_z(i,j,k)^{n+1/2}}{\Delta y}\right], \tag{2.12d}$$

$$H_y(i,j,k)^{n+1} = H_y(i,j,k)^n + \frac{\Delta t}{\mu}\left[\frac{E_z(i+1,j,k)^{n+1/2} - E_z(i,j,k)^{n+1/2}}{\Delta x} - \frac{E_x(i,j,k+1)^{n+1/2} - E_x(i,j,k)^{n+1/2}}{\Delta z}\right], \tag{2.12e}$$

$$H_z(i,j,k)^{n+1} = H_z(i,j,k)^n + \frac{\Delta t}{\mu}\left[\frac{E_x(i,j+1,k)^{n+1/2} - E_x(i,j,k)^{n+1/2}}{\Delta y} - \frac{E_y(i+1,j,k)^{n+1/2} - E_y(i,j,k)^{n+1/2}}{\Delta x}\right]. \tag{2.12f}$$

In addition, for (2.12a) through (2.12f), ε's and μ's should be values at the medium that we want to determine the corresponding fields.

As mentioned in the previous section, the stability criterion of a finite-difference scheme is important for determination of stable region. For FD-TD in rectangular coordinates, the derivation has done [2, 13] by applying space and time eigenvalue problems. The derivation is included in Appendix D of this thesis. The derived stability criterion is

$$\Delta t \le \frac{1}{v\sqrt{\frac{1}{(\Delta x)^2} + \frac{1}{(\Delta y)^2} + \frac{1}{(\Delta z)^2}}}, \tag{2.13a}$$

where v is maximum phase velocity in solution region. The above equation provides the upper bound of the time increment Δt that makes the computations still be stable. Frequently in practical, the mesh sizes Δx, Δy and Δz are equally defined. Hence, the more compact equation is obtained

$$\Delta t \le \frac{\delta}{v\sqrt{3}}, \tag{2.13b}$$

where $\delta = \Delta x = \Delta y = \Delta z$. From (2.13a) and (2.13b), the mesh sizes are usually be defined in terms of a wavelength of applying source, for example, one-tenth of a wavelength for normal situations. Practically, we usually take Δt slightly far from the upper bound because the derived stability condition accounts for only the truncation

or discretization errors, while the other sources of errors are not included. For example, a factor *2* instead of $\sqrt{3}$ in (2.13b) is used [1, 2].

Besides the errors mentioned before in the parts of general finite-difference methods, FD-TD algorithms also produce one kind of errors known as *numerical velocity errors* or *numerical dispersion*. This source of errors exists due to the fact that the phase velocity of the simulating wave modes in the computational grid cells differs from the ideal vacuum speed of light. The velocity errors vary with many parameters such as the wavelength of the numerical waves, the direction of propagation and the resolution of grid cells (mesh sizes). The behavior of this type of errors is that the phase velocity of the simulating wave is accumulatively delayed resulting in numerical (lagged) phase errors. There are some electromagnetic problems directly affected by these errors, such as problems involving pulse sources (obtaining broadening and ringing waveforms), and problems about multiple reflections (resulting in imperfect cancellations). The equation describing these errors is obtained in [13, 14] and also included in Appendix D,

$$\left[\frac{1}{v\Delta t}\sin\left(\frac{\omega\Delta t}{2}\right)\right]^2=\left[\frac{1}{\Delta x}\sin\left(\frac{\tilde{k}_x\Delta x}{2}\right)\right]^2+\left[\frac{1}{\Delta y}\sin\left(\frac{\tilde{k}_y\Delta y}{2}\right)\right]^2+\left[\frac{1}{\Delta z}\sin\left(\frac{\tilde{k}_z\Delta z}{2}\right)\right]^2, \tag{2.14a}$$

where ω is the wave angular frequency, and $\tilde{k}_x$, $\tilde{k}_y$ and $\tilde{k}_z$ are the numerical wave constants in *x*-, *y*- and *z*-directions, respectively. From the above equation, it is seen that when Δx, Δy and Δz approach to zero (Δt automatically approaches to zero, from (2.13a)) the ideal dispersion is obtained,

$$\left(\frac{\omega}{v}\right)^2=k_x^{\,2}+k_y^{\,2}+k_z^{\,2}. \tag{2.14b}$$

This also holds for the case when Δt relates exactly to Δx, Δy and Δz as shown in (2.13b). The phase velocity errors produced can be obtained by solving (2.14a) for the numerical wave constant $\tilde{k}$ and relating it to the ideal wave constant as $2\pi/\tilde{k}$, incase of the normalized wavelength. The illustrations of the velocity errors are shown in Fig. 2.7 and Fig. 2.8. Fig. 2.7 shows the percentages of phase velocity errors as function of wave angles, θ and ϕ, for the case $\Delta t=\delta/2c$. As shown in the figure, it is evident that when grid resolutions increase (grid sizes decrease) the errors decrease, and the maximum errors are found where θ and ϕ are equal to $0°$ or $90°$. In practical sense, for example, when the grid sizes are $\lambda_o/10$ and the propagated distance is *50* cells ($5\lambda_o$), the maximum phase errors is about $23°$ (lagging). In Fig. 2.8, the percentages of phase velocity errors are shown versus the variation of grid sizes, for the case $\Delta t=\delta/2c$. From the figure, it is seen that the phase velocity errors increase abruptly near the *3 cells/*λ_o resolution, and actually approach to infinity when the *breakdown* resolution range, *2* to *3 cells/*λ_o, is reached (when θ or $\phi = 0°$ or $90°$ the breakdown resolution is about *3 cells/*λ_o, θ or $\phi = 45°$ the breakdown resolution is about *2 cells/*λ_o, and for each of the other wave-angle pairs the breakdown resolution is somewhere between *2* and *3 cells/*λ_o).

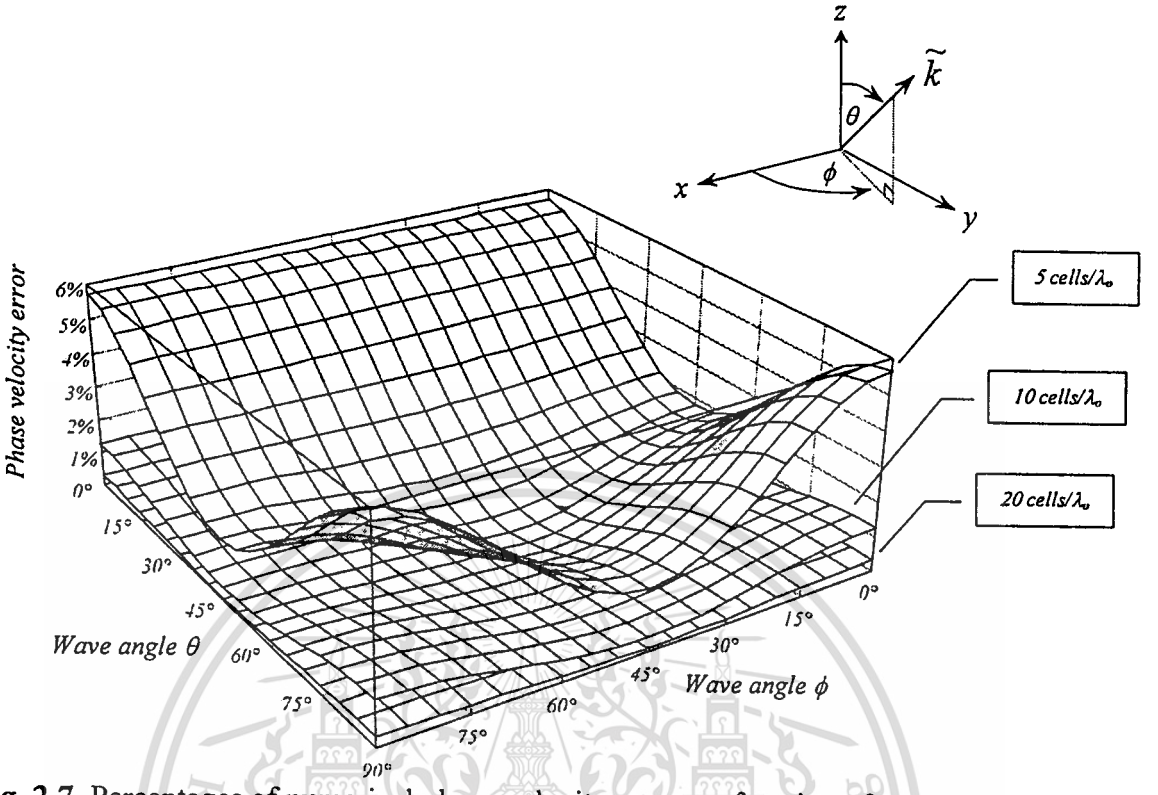

Fig. 2.7 Percentages of numerical phase velocity errors as function of wave angles, θ and ϕ

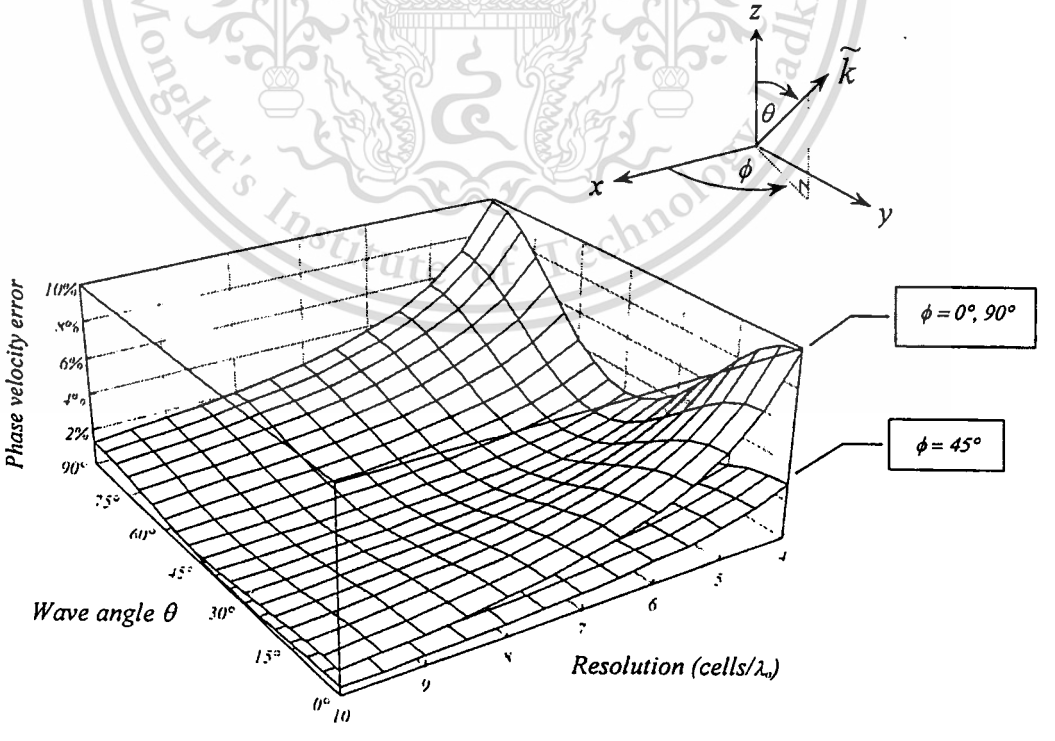

Fig. 2.8 Percentages of numerical phase velocity errors as function of resolutions (*cells*/λ_o) and wave angle θ. The wave angle ϕ is fixed at $0°$, $45°$ and $90°$.

In case of the propagating waves are pulse waveforms, the lower-frequency components of the pulses will propagate, in FD-TD grids, faster than the higher-frequency components, so these cause broadening and ringing pulse waveforms. The figure also means that when a non-uniform FD-TD algorithm (containing various cell sizes) is used, the nonphysical reflection and refraction will occur in the simulation at the interfaces of the different-size cells. As mentioned before, to reduce the numerical phase errors the grid sizes should be kept as small as possible. Alternatively, the higher-order FD-TD algorithms, such as the forth-order, are often be chosen if the errors cause serious phase lagging, or (2.14a) is often use to predict and correct the lagged phase.

The last material to be included here is about the boundary conditions. The boundary conditions for closed-region FD-TD problems are often made by simple classical boundary conditions. For example, a problem of resonating waves inside a very high-conductivity cavity can be approximately treated by using a perfect conductor's boundary conditions. Unlike the closed-region problems, the opened-region problems need more sophisticated boundary conditions to truncate the solution regions with as less as possible nonphysical reflections. These conditions are known as *radiation boundary conditions* (RBCs) or *absorbing boundary conditions* (ABCs). The early age of RBC theory is in the 1970s and 1980s, including the methods of Bayliss-Turkel, Engquist-Majda, Trefethen-Halpern, Higdon, and Liao and Mei-Fang [13]. These boundary conditions are found producing nonphysical reflection coefficients in the range of about *–10* dB to *–25* dB (power). In the new era of ABC technology, the dominant one is the *artificial* ABC called *perfectly matched layer* (*PML*) conducted by Berenger [15]. This technique can suppress the nonphysical reflections deeper than *–80* dB (power). Because of their sophistication, the details about all ABCs cannot be included, here. Some useful ABCs will be discussed in details in the next chapter.

2.4 Conclusions

The basic finite-difference schemes, backward, forward and central differences are commonly used to approximate solutions of PDEs. These schemes always produced some errors in the results obtained. The main sources of errors are modeling errors, truncation (discretization) errors and roundoff errors. The first one can be avoided by studying well about the physical behaviors of the being modeled problems, so it helps us to decide what order of accuracy should be used. The second type of errors can be reduced by keeping the mesh sizes small. The third type of errors seems unavoidable; however, it can be minimized by using double-precision arithmetic. It should be noted that the last two types of errors are dependent, and must be considered in the same time. Besides the mentioned errors above, the stability of a finite-difference scheme is also important and needs to be considered before one can process further in the finite-difference method. The stability criterion of a finite-difference scheme can be determined by finding the ratio of errors (amplification factor). If the ratio is not greater than unity, the finite-difference computation is stated as stable. Otherwise, it is considered unstable.

The finite-difference time-domain (FD-TD) algorithm can be constructed directly from Maxwell's equations in differential form. The basic FD-TD equations in rectangular coordinates can be obtained by applying the halved-step central differences to the decomposed Maxwell's equations (six coupled PDEs) together with referring to the Yee's unit cell (Fig. 2.6). To proceed further in FD-TD calculations, the stability criterion must be determined. One approach to achieve the criterion is

solving the space and time eigenvalue problems. The obtained stability criterion must be used to find a time step Δt by using a minimum size of grid cells in solution region. Furthermore, the calculated Δt should be backed off from its upper limit to compensate the instability due to other sources of errors that are not included in the criterion. An important source of errors that one should be awared in working with FD-TD simulations is numerical velocity errors or numerical dispersion. When the solution region contains large number of grid cells, these errors seriously affect the phase of the resulting waves. Decreasing the grid sizes can reduce these effects; however, when encounter with the severe phase lagging one may need to correct the lagged phase by utilizing (2.14a), or alternatively, use higher-order FD-TD algorithms. Included as the last topic, the boundary conditions are found easy to apply when the problems are involving closed regions, but they are more sophisticated when the being model problems are in open regions. The boundary conditions with small nonphysical reflections that are used to truncate solution regions are called radiation boundary conditions (RBCs) or absorbing boundary conditions (ABCs). Recently, the most powerful ABC is the perfectly matched layer (PML) which provides the smallest nonphysical reflection coefficient, less than *–80* dB (power).

Chapter 3

Finite-Difference Time-Domain Method in Spherical Coordinates

After the finite-difference time-domain method in rectangular coordinates have been found as the versatile tool for solving electromagnetic problems [1, 2, 5, 6, 16, 17], many researchers of this and relating fields conducted advancements in this method [7, 13, 18-23]. Especially, some of them aimed at finding FD-TD algorithms for other coordinate systems, started from simple systems such as cylindrical and spherical coordinates [7] to the most sophisticated system, general curvilinear coordinates [18, 19]. Although the latest one can override all the simpler-coordinate FD-TD algorithms, it will always be the last choice for users (i.e. when one can not solve his problem by using the simpler coordinates). This is true because of its complexity and extreame resource requirements. The best way in choosing a coordinate system of FD-TD algorithm for solving a problem is using the simplest one that can best fit to the boundary of the problem. So in this thesis, the FD-TD algorithm in spherical coordinates is selected as a numerical tool. This algorithm is first induced by R. Holland [7], but in his presentation was lacking of a stability criterion and effective ways in treating singularities. These missing points will also be fulfilled in this chapter. The derivation procedures are mostly the same as described in the section of FD-TD in rectangular coordinates, except that the part of radiation boundary conditions will be substantially discussed. To complete this chapter, some numerical results will be illustrated by testing the derived FD-TD algorithm with various types of applying sources such as pulse and continuous waves, and using different types of radiation boundary conditions.

3.1 Construction of FD-TD Equations

The configuration of the subdivided spherical solution region is shown in Fig.3.1(a). Solutions within the region are to be approximated by using a FD-TD algorithm in spherical coordinates. The steps for deriving the FD-TD equations are the same as mentioned in the derivation of FD-TD equations in rectangular coordinates. By using (2.9a) and (2.9b) in conjunction with the vector identity for curl of a vector in spherical coordinates

$$\begin{aligned}\nabla\times\bar{A} = &\frac{\bar{a}_r}{r\sin\theta}\left[\frac{\partial}{\partial\theta}(A_\phi\sin\theta)-\frac{\partial A_\theta}{\partial\phi}\right]\\ &+\frac{\bar{a}_\theta}{r}\left[\frac{1}{\sin\theta}\frac{\partial A_r}{\partial\phi}-\frac{\partial}{\partial r}(rA_\phi)\right]\\ &+\frac{\bar{a}_\phi}{r}\left[\frac{\partial}{\partial r}(rA_\theta)-\frac{\partial A_r}{\partial\theta}\right],\end{aligned} \tag{3.1}$$

one can write out the system of six-coupled partial differential equations as follows:

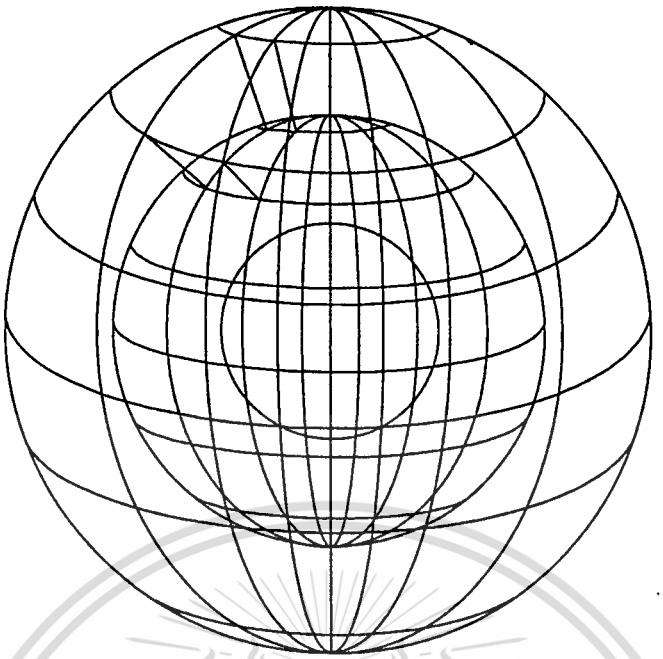

Fig. 3.1(a) The subdivided spherical solution region

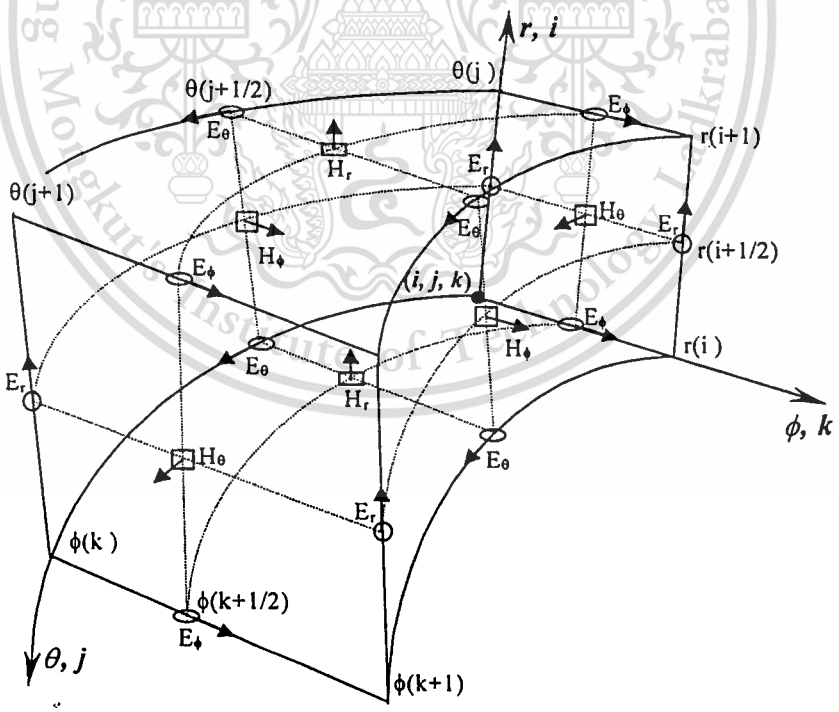

Fig. 3.1(b) Positions of the six field components on each subdivided volume cell

$$\varepsilon\frac{\partial E_r}{\partial t}+\sigma E_r=-J_r+\frac{1}{r\sin\theta}\left[\frac{\partial}{\partial\theta}(H_\phi\sin\theta)-\frac{\partial H_\theta}{\partial\phi}\right], \tag{3.2a}$$

$$\varepsilon\frac{\partial E_\theta}{\partial t}+\sigma E_\theta=-J_\theta+\frac{1}{r}\left[\frac{1}{\sin\theta}\frac{\partial H_r}{\partial\phi}-\frac{\partial}{\partial r}(rH_\phi)\right], \tag{3.2b}$$

$$\varepsilon\frac{\partial E_\phi}{\partial t}+\sigma E_\phi=-J_\phi+\frac{1}{r}\left[\frac{\partial}{\partial r}(rH_\theta)-\frac{\partial H_r}{\partial\theta}\right], \tag{3.2c}$$

$$\mu\frac{\partial H_r}{\partial t}=\frac{1}{r\sin\theta}\left[\frac{\partial E_\theta}{\partial\phi}-\frac{\partial}{\partial\theta}(E_\phi\sin\theta)\right], \tag{3.2d}$$

$$\mu\frac{\partial H_\theta}{\partial t}=\frac{1}{r}\left[\frac{\partial}{\partial r}(rE_\phi)-\frac{1}{\sin\theta}\frac{\partial E_r}{\partial\phi}\right], \tag{3.2e}$$

$$\mu\frac{\partial H_\phi}{\partial t}=\frac{1}{r}\left[\frac{\partial E_r}{\partial\theta}-\frac{\partial}{\partial r}(rE_\theta)\right]. \tag{3.2f}$$

These are the ready forms for constructing FD-TD equations by approximating the time derivatives (left-hand side) and the space derivatives (right-hand side) with the second (or higher) order central-difference approximation. To perform the derivation, at first, the locations of the six field components must be assigned on a volume cell as illustrated in Fig.3.1(b). Before processing further in the derivation, the following notations should be made to get the compact forms of FD-TD equations.

In radial direction, Fig.3.2(a) shows the entire problem space subdivided into many layers by many constant-radius spherical surfaces. The distance between two adjacent surfaces is Δr and an index 'i' is used to denote the constant radius surfaces. Assuming that $i = 0$ at the origin ($r = 0$) and is increased by one at each outer surface, and finally $i = I_{max}$ at the outermost surface ($r = R_{max}$). In θ-direction, Fig.3.2(b) shows the subdivided problem space by θ-constant surfaces which each is denoted by an index 'j'. The angle is divided into $\Delta\theta$. The index, $j = 0$ at $\theta = 0°$ (north pole), is increased by one at the next θ-constant surface and so on, until the final surface is reached at $j = J_{max}$ ($\theta = 180°$, south pole). In ϕ-direction (Fig.3.2(c)), the problem space is subdivided into many volume segments in azimuth-angle (ϕ-) direction by ϕ-constant surfaces (angle between two adjacent surfaces is $\Delta\phi$). Each surface is represented by an index 'k', $k = 0$ at $\phi = 0°$ (prime meridian) with a step of one and finally, $k = K_{max}$ at $\phi = 360°$ which is exactly the same surface as $k = 0$. In addition to the three orthogonal variables in spherical coordinate (r, θ and ϕ), they are sometimes assigned to be functions of i ($r(i)$), j ($\theta(j)$) and k ($\phi(k)$), respectively.

Practically, aforementioned incremental distance in radial direction (Δr) and angle in θ- and ϕ- directions ($\Delta\theta$ and $\Delta\phi$, respectively) may not be constant over the entire problem space. Thus, normally, Δr, $\Delta\theta$ and $\Delta\phi$ are considered as functions of i ($\Delta r(i)$), j ($\Delta\theta(j)$) and k ($\Delta\phi(k)$), respectively. Alternatively, if Δr, $\Delta\theta$ and $\Delta\phi$ are assigned to be constant over the entire problem space, we simply get $\Delta r(i) = \Delta r$, $\Delta\theta(j) = \Delta\theta$ and $\Delta\phi(k) = \Delta\phi$ for any values of i, j and k, respectively.

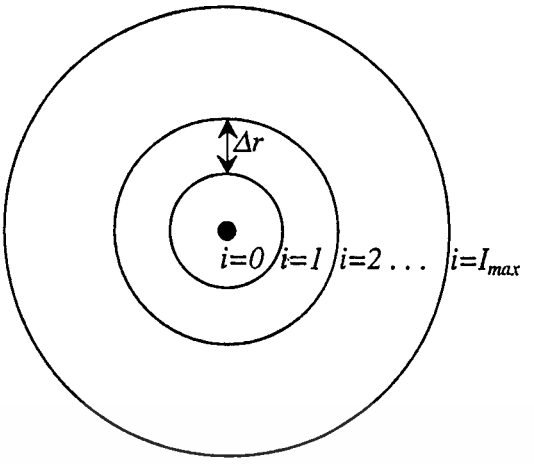

Fig. 3.2(a) Subdivision of solution region in radial direction

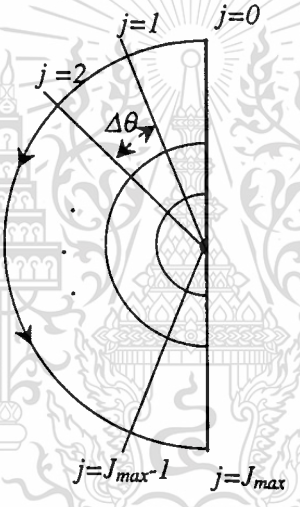

Fig. 3.2(b) Subdivision of solution region in θ-direction

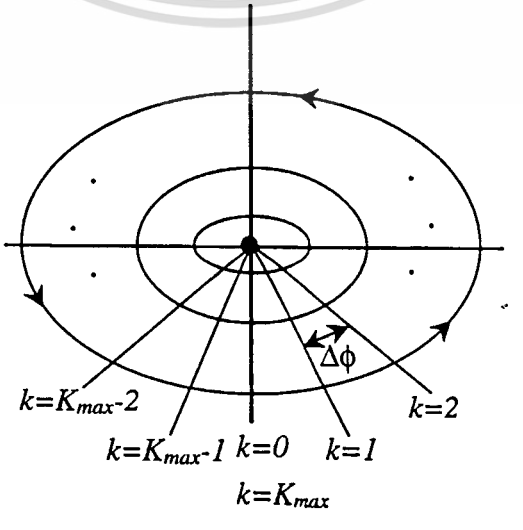

Fig. 3.2(c) Subdivision of solution region in ϕ-direction

The notations described above can be summarized as follows:
In *r-direction*,

$$r(0) = 0, \quad r(I_{max}) = R_{max} \text{ and } \Delta r(i) = r(i+1) - r(i). \tag{3.3a}$$

In *θ-direction*,

$$\theta(0) = 0°, \quad \theta(J_{max}) = 180° \text{ and } \Delta\theta(j) = \theta(j+1) - \theta(j). \tag{3.3b}$$

In *ϕ-direction*,

$$\phi(0) = 0°, \quad \phi(K_{max}) = 360° \text{ and } \Delta\phi(k) = \phi(k+1) - \phi(k). \tag{3.3c}$$

Similar to that in rectangular coordinates (2.4b), the discrete function for spherical coordinates is defined as

$$f(i,j,k)^n \equiv f(r(i),\theta(j),\phi(k);n\Delta t). \tag{3.3d}$$

From the discussed central finite-difference formula (2.5a) and (2.5b), the half-step approximation for time and space derivatives in spherical coordinates are found to be

$$\frac{\partial f(i,j,k)^n}{\partial r} \approx \frac{f(i+1/2,j,k)^n - f(i-1/2,j,k)^n}{\Delta r}, \tag{3.4a}$$

and

$$\frac{\partial f(i,j,k)^n}{\partial t} \approx \frac{f(i,j,k)^{n+1/2} - f(i,j,k)^{n-1/2}}{\Delta t}. \tag{3.4b}$$

By applying (3.4a) and (3.4b) to (3.2a), the recurrence E_r field components can be written as

$$\begin{aligned} E_r(i,j,k)^{n+1/2} = {} & \frac{\varepsilon/\Delta t - \sigma/2}{\varepsilon/\Delta t + \sigma/2} E_r(i,j,k)^{n-1/2} \\ & + \frac{1}{\varepsilon/\Delta t + \sigma/2}\left\{ -J_r(i,j,k)^n + \frac{1}{r(i+1/2)\sin\theta(j)} \right. \\ & \times \left[\frac{\sin\theta(j+1/2)H_\phi(i,j+1/2,k)^n - \sin\theta(j-1/2)H_\phi(i,j-1/2,k)^n}{\Delta\theta(j-1/2)} \right. \\ & \left. \left. - \frac{H_\theta(i,j,k+1/2)^n - H_\theta(i,j,k-1/2)^n}{\Delta\phi(k-1/2)} \right] \right\}, \end{aligned} \tag{3.5a}$$

which is valid for $i = 0$ to $I_{max}-1$, $j = 1$ to $J_{max}-1$ and $k = 1$ to K_{max}.
Similarly, (3.2b) and (3.2c) can be derived to get recurrence relations, respectively, as

$$E_\theta(i,j,k)^{n+1/2} = \frac{\varepsilon/\Delta t - \sigma/2}{\varepsilon/\Delta t + \sigma/2} E_\theta(i,j,k)^{n-1/2} + \frac{1}{\varepsilon/\Delta t + \sigma/2}\left\{ -J_\theta(i,j,k)^n + \frac{1}{r(i)} \times \left[\frac{H_r(i,j,k+1/2)^n - H_r(i,j,k-1/2)^n}{\sin\theta(j)\Delta\phi(k-1/2)} - \frac{r(i+1/2)H_\phi(i+1/2,j,k)^n - r(i-1/2)H_\phi(i-1/2,j,k)^n}{\Delta r(i-1/2)} \right] \right\}, \quad (3.5b)$$

which is valid for $i = 1$ to $I_{max}-1$, $j = 0$ to $J_{max}-1$ and $k = 1$ to K_{max},

$$E_\phi(i,j,k)^{n+1/2} = \frac{\varepsilon/\Delta t - \sigma/2}{\varepsilon/\Delta t + \sigma/2} E_\phi(i,j,k)^{n-1/2} + \frac{1}{\varepsilon/\Delta t + \sigma/2}\left\{ -J_\phi(i,j,k)^n + \frac{1}{r(i)} \times \left[\frac{r(i+1/2)H_\theta(i+1/2,j,k)^n - r(i-1/2)H_\theta(i-1/2,j,k)^n}{\Delta r(i-1/2)} - \frac{H_r(i,j+1/2,k)^n - H_r(i,j-1/2,k)^n}{\Delta\theta(j-1/2)} \right] \right\}, \quad (3.5c)$$

which is valid for $i = 1$ to $I_{max}-1$, $j = 1$ to $J_{max}-1$ and $k = 0$ to $K_{max}-1$. Additionally, the σE terms in (3.2a) through (3.2c) can be approximated by using the *semi-implicit approximation* [13], as described in the previous chapter.

Similarly, by applying (3.4a) and (3.4b) to (3.2d) through (3.2f) the results are obtained as

$$H_r(i,j,k)^{n+1} = H_r(i,j,k)^n + \frac{\Delta t}{\mu r(i)\sin\theta(j+1/2)}\left[\frac{E_\theta(i,j,k+1)^{n+1/2} - E_\theta(i,j,k)^{n+1/2}}{\Delta\phi(k)} - \frac{\sin\theta(j+1)E_\phi(i,j+1,k)^{n+1/2} - \sin\theta(j)E_\phi(i,j,k)^{n+1/2}}{\Delta\theta(j)} \right], \quad (3.6a)$$

which is valid for $i = 1$ to I_{max}, $j = 0$ to $J_{max}-1$ and $k = 0$ to $K_{max}-1$,

$$H_\theta(i,j,k)^{n+1} = H_\theta(i,j,k)^n + \frac{\Delta t}{\mu r(i+1/2)}\left[\frac{r(i+1)E_\phi(i+1,j,k)^{n+1/2} - r(i)E_\phi(i,j,k)^{n+1/2}}{\Delta r(i)} - \frac{E_r(i,j,k+1)^{n+1/2} - E_r(i,j,k)^{n+1/2}}{\sin\theta(j)\Delta\phi(k)} \right], \quad (3.6b)$$

which is valid for $i = 0$ to $I_{max}-1$, $j = 1$ to $J_{max}-1$ and $k = 0$ to $K_{max}-1$,

$$H_\phi(i,j,k)^{n+1} = H_\phi(i,j,k)^n + \frac{\Delta t}{\mu r(i+1/2)}\left[\frac{E_r(i,j+1,k)^{n+1/2} - E_r(i,j,k)^{n+1/2}}{\Delta\theta(j)} - \frac{r(i+1)E_\theta(i+1,j,k)^{n+1/2} - r(i)E_\theta(i,j,k)^{n+1/2}}{\Delta r(i)}\right], \quad (3.6c)$$

which is valid for $i = 0$ to $I_{max}-1$, $j = 0$ to $J_{max}-1$ and $k = 0$ to $K_{max}-1$. In addition to (3.5a) through (3.6c), ε's and μ's should be values at the medium that we want to determine the corresponding fields.

3.2 Singularity Considerations

Singularities of the FD-TD in spherical coordinates will be considered and treated in this section. From the formulated FD-TD (3.5a) through (3.6c), the indices i, j and k have their own valid intervals such as the index j in (3.5a) can be run from 1 to $J_{max}-1$ only. The points that can not be advanced by using (3.5a) through (3.6c) are considered here as *singularities*. There are three main singularities occur in this FD-TD algorithm. Typically, some singular points can be treated to find some field components and others can not.

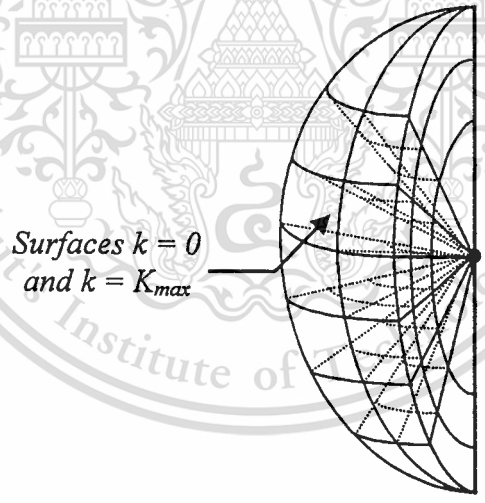

Fig. 3.3(a) Singularity at $k = 0$ ($\phi = 0°$) and $k = K_{max}$ ($\phi = 360°$) surfaces

The first singularity occurs at the prime meridian which is on the ϕ-constant surface at $\phi = 0°$ and $360°$ as shown in Fig.3.3(a). From (3.5a) through (3.6c), it is evident that all of the six field components are affected by this singularity. If we simply run the index k from 0 to K_{max}, the field components at this surface will be calculated twice. We can treat this problem by means of *joining conditions* [7] which can be derived directly from (3.5a) through (3.6c) by expecting the joining points of field components at the surfaces $k = 0$ and K_{max}. The resultant conditions can be obtained as

$$E_r(i,j,0)^{n+1/2} = E_r(i,j,K_{max})^{n+1/2}, \quad (3.7a)$$

$$E_\theta(i, j, 0)^{n+1/2} = E_\theta(i, j, K_{max})^{n+1/2}, \tag{3.7b}$$

$$E_\phi(i, j, K_{max})^{n+1/2} = E_\phi(i, j, 0)^{n+1/2}, \tag{3.7c}$$

$$H_r(i, j, K_{max})^{n+1} = H_r(i, j, 0)^{n+1}, \tag{3.7d}$$

$$H_\theta(i, j, K_{max})^{n+1} = H_\theta(i, j, 0)^{n+1} \tag{3.7e}$$

and

$$H_\phi(i, j, K_{max})^{n+1} = H_\phi(i, j, 0)^{n+1}. \tag{3.7f}$$

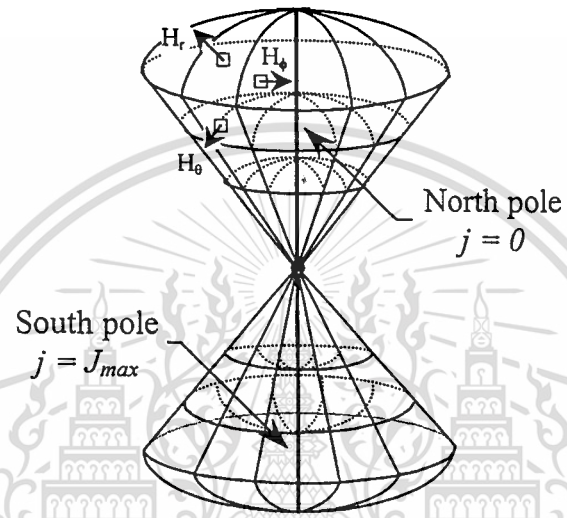

Fig. 3.3(b) Singularity at north ($\theta = 0°$) and south ($\theta = 180°$) poles

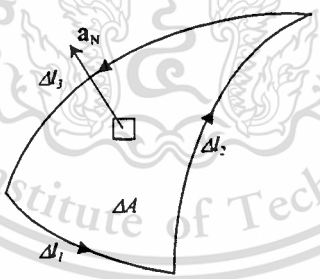

Fig. 3.3(c) A closed path (by Δl_1, Δl_2 and Δl_3) and a differential area (ΔA) near the north pole

The second singularity, which is more difficult to treat, occurs at the north ($\theta = 0°$) and south ($\theta = 180°$) poles as shown in Fig.3.3(b). Evidently, there are three field components (i.e. E_r, E_ϕ and H_θ) gathered in these poles. Presently, we can approximate only the E_r field component using the encircling H_r fields (while E_ϕ and H_θ are kept unevaluated). By utilizing the integral form of the curl $\overline{H}$ equation

$$\oint_C \overline{H} \cdot d\overline{l} = \iint (\overline{J}_i + \sigma \overline{E} + \varepsilon \frac{\partial \overline{E}}{\partial}) \cdot d\overline{A}, \tag{3.8a}$$

where $\oint_C$ denotes integral along closed-path C and then recast (3.8a) into an approximated form as

$$\frac{\oint_C \bar{H} \cdot d\bar{l}_{\Delta A}}{\Delta A} \approx (\bar{J}_i + \sigma \bar{E} + \varepsilon \frac{\partial \bar{E}}{\partial t})_N , \tag{3.8b}$$

where the ΔA subscript of $d\bar{l}$ indicates that the differential path is the perimeter of the differential area ΔA, and the subscript N denotes the right-hand normal to ΔA, as shown in Fig. 3.3(c).

By applying (3.4b) to the right side of (3.8b) and rearranging, this yields

$$E_r(i,j,k)^{n+1/2} = \frac{\varepsilon/\Delta t - \sigma/2}{\varepsilon/\Delta t + \sigma/2} E_r(i,j,k)^{n-1/2} + \frac{1}{\varepsilon/\Delta t + \sigma/2} \left\{ -J_r(i,j,k)^n + \frac{\oint_C H_\phi \cdot dl_{\Delta A}}{\Delta A} \right\}. \tag{3.8c}$$

For the north pole ($j = 0$), the closed-path C is defined by the $\theta(1/2)$-circle on $r(i+1/2)$-surfaces. The integral term of (3.8c) can be approximated by a summation of products of H_ϕ and $dl_{\Delta A}$ as

$$\oint_C H_\phi \cdot dl_{\Delta A} \approx \sum_{k=0}^{K_{max}-1} H_\phi r(i+1/2) \sin\theta(1/2) \Delta\phi(k), \tag{3.8d}$$

and the differential area ΔA is replaced by the area on the $r(i+1/2)$-surface bounded by the closed-path C

$$\Delta A = \int_0^{2\pi} \int_0^{\theta(1/2)} r^2 (i+1/2) \sin\theta \, d\theta d\phi = 2\pi r^2 (i+1/2)[1 - \cos\theta(1/2)] \tag{3.8e}$$

Finally, by substituting (3.8d) and (3.8e) into (3.8c), one obtains

$$E_r(i,1,k)^{n+1/2} = \frac{\varepsilon/\Delta t - \sigma/2}{\varepsilon/\Delta t + \sigma/2} E_r(i,1,k)^{n-1/2} + \frac{1}{\varepsilon/\Delta t + \sigma/2} \left\{ -J_r(i,1,k)^n + \frac{\sin\theta(1/2)}{2\pi r(i+1/2)[1-\cos\theta(1/2)]} \sum_{k=0}^{K_{max}-1} H_\phi \Delta\phi(k) \right\}. \tag{3.9a}$$

Similarly, for the south pole, the closed-path C is defined by the $\theta(J_{max}-1/2)$-circle on the $r(i+1/2)$-surfaces. By following the above procedures, one obtaines

$$E_r(i,J_{max},k)^{n+1/2} = \frac{\varepsilon/\Delta t - \sigma/2}{\varepsilon/\Delta t + \sigma/2} E_r(i,J_{max},k)^{n-1/2} + \frac{1}{\varepsilon/\Delta t + \sigma/2}\left\{-J_r(i,J_{max},k)^n - \frac{\sin\theta(J_{max}-1/2)}{2\pi r(i+1/2)\left[1+\cos\theta(J_{max}-1/2)\right]} \sum_{k=0}^{K_{max}-1} H_\phi \Delta\phi(k)\right\}. \quad (3.9b)$$

Moreover, the H_r field component needs to be estimated by some means. The method introduced here is using Faraday's law,

$$\mu \frac{\partial}{\partial t} \iint_S \bar{H} \cdot d\bar{S} = -\oint_C \bar{E} \cdot d\bar{l} \,. \quad (3.10a)$$

By applying (3.10a) to the H_r field component near the north pole yields

$$H_r(i,0,k)^{n+1} = H_r(i,0,k)^n + \frac{\Delta t}{\mu r(i)\Delta\phi\left[1-\cos(\Delta\theta)\right]} \times \left\{ \begin{array}{l} -\sin(\theta(j))\Delta\phi \;\; E_\phi(i,1,k)^{n+1/2} \\ +\Delta\theta\left[E_\theta(i,0,k+1)^{n+1/2} - E_\theta(i,0,k)^{n+1/2}\right] \end{array} \right\}. \quad (3.10b)$$

Similarly, the equation for treating the H_r field component near the south pole can be obtained as

$$H_r(i,J_{max}-1,k)^{n+1} = H_r(i,J_{max}-1,k)^n + \frac{\Delta t}{\mu r(i)\Delta\phi\left[1-\cos(\Delta\theta)\right]} \times \left\{ \begin{array}{l} \sin(\theta(j))\Delta\phi \;\; E_\phi(i,J_{max}-1,k)^{n+1/2} \\ +\Delta\theta\left[E_\theta(i,J_{max}-1,k+1)^{n+1/2} - E_\theta(i,J_{max}-1,k)^{n+1/2}\right] \end{array} \right\}. \quad (3.10c)$$

Conclusively, one can avoid this second singularity by using (3.9a) and (3.9b) to approximate E_r fields in the poles, and applying (3.10b) and (3.10c) to H_r fields near to the poles; while the E_ϕ and H_θ in the poles are kept unevaluated.

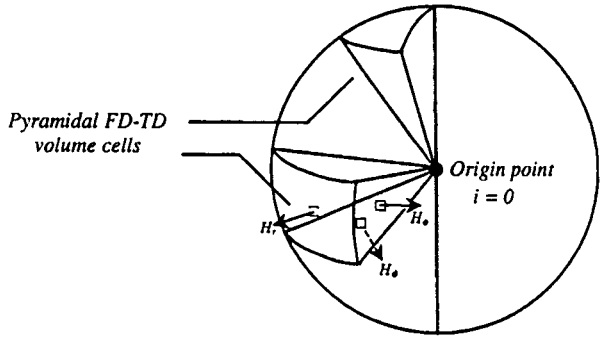

Fig. 3.3(d) Singularity at the origin point, due to pyramidal FD-TD volume cells

The third singularity takes place at the origin, as shown in Fig.3.3(d). Because of the pyramidal shapes of the volume cells, the three field components E_θ, E_ϕ and H_r are merged in the origin point. So, the algorithm can not be advanced at these cells as usual, thus limits utilities itself. There are some possible schemes that can be used to treat this problem such as defining a new style of finite difference approximation (e.g. forward-difference formula) or assuming a perfect conductor of finite radius at the origin. However, the first choice may reduce accuracy of the algorithm, and the second one sometimes causes severe reflections and leads to instability. Here, the Faraday's law (3.10a) is applied, again, to approximate the H_θ and H_ϕ fields near the origin. By referring to Fig.3.3(d) and utilizing Faraday's law, the equations needed to update the H_θ and H_ϕ fields, respectively, on the rectangular-base and triangular-base pyramidal cells can be obtained as

$$H_\theta(0,j,k)^{n+1} = H_\theta(0,j,k)^n + \frac{2\Delta t}{\mu(\Delta r)^2 \sin(\theta(j))\Delta\phi} \times \left\{ \begin{array}{l} r(i)\sin(\theta(j))\Delta\phi \;\; E_\phi(1,j,k)^{n+1/2} \\ +\Delta r \;\; \left[E_r(0,j,k)^{n+1/2} - E_r(0,j,k+1)^{n+1/2}\right] \end{array} \right\} \tag{3.11a}$$

and

$$H_\phi(0,j,k)^{n+1} = H_\phi(0,j,k)^n + \frac{2\Delta t}{\mu(\Delta r)^2 \Delta\theta} \times \left\{ \begin{array}{l} -r(i)\Delta\theta \;\; E_\theta(1,j,k)^{n+1/2} \\ +\Delta r \;\; \left[E_r(0,j+1,k)^{n+1/2} - E_r(0,j,k)^{n+1/2}\right] \end{array} \right\}. \tag{3.11b}$$

In case of triangular-base pyramidal FD-TD cells (Fig.3.3(d)), not only the above equations ((3.11a) and (3.11b)) must be used, but also (3.9a) and (3.9b) are required for updating FD-TD calculations near the origin point. By utilizing (3.10a) through (3.11b), the H_r, H_θ and H_ϕ fields near the origin can be approximated, while again, the E_θ, E_ϕ and H_r field components in the origin point are kept unevaluated.

In addition to all of the equations obtained by approximating integrals, it is found that they produce some modeling errors. These errors occur because all the integrands are assumed to be constant over their corresponding integration paths and surfaces, while the physical paths and surfaces are curvatures which far from linearity. However, these errors can be controlled by keeping the pyramidal FD-TD cells as small as possible.

3.3 Radiation Boundary Conditions

Besides described before in the part of singularities, the outermost (truncated) boundary is another surface where one can not advance the algorithm as usual. Thus, some schemes are needed to approximate the field components (e.g. E_θ and E_ϕ) at this surface that cause reflections as less as possible. The method which are simple for implementing in spherical coordinates are deriving in this section.

Assuming that any outgoing waves can be represented in a form

$$U = \frac{f(t - r/v)}{r}, \tag{3.12}$$

where U denotes any outgoing waves, t is time, r is radial distance from a reference point or an origin and v is phase velocity of waves.

Here, only electric field components (E_θ and E_ϕ) are enforced by (3.12) at the truncated boundary. By using E instead of U, and the remainder parameters are written in forms of the conventional FD-TD notations as defined before, yields

$$E(i,j,k)^{n+1/2} = \frac{f((n+1/2)\Delta t - r(i)/v)}{r(i)}. \tag{3.13a}$$

Furthermore, by using (3.13a) at the truncated boundary, we obtain

$$E(I_{max},j,k)^{n+1/2} = \frac{f((n+1/2)\Delta t - r(I_{max})/v)}{r(I_{max})}. \tag{3.13b}$$

As mentioned before, the electric field components at the outermost boundary can not be advanced by the algorithm, so they should be approximated by using some known values of electric field components at an inner layer. The wisest concept is to use electric field components at the inner surface adjacent to it, such as $E(I_{max}\text{-}1, j, k)^{n-1/2}$, and $E(I_{max}\text{-}1, j, k)^{n-1/2}$ can be represented in form of (3.13a) as

$$E(I_{max}-1,j,k)^{(n-1/2)-\zeta} = \frac{f((n-1/2)\Delta t - r(I_{max}-1)/v - \zeta\Delta t)}{r(I_{max}-1)}, \tag{3.13c}$$

where ζ denotes previous time steps of $E(I_{max}\text{-}1, j, k)^{n-1/2}$ which is usually an integer value. For example, $\zeta = -1$ means the present time step $E(I_{max}\text{-}1, j, k)^{n+1/2}$. Also, $E(I_{max}, j, k)^{n+1/2}$ can be written in a similar form of (3.13c) as

$$E(I_{max},j,k)^{n+1/2} = \frac{f((n-1/2)\Delta t - r(I_{max}-1)/v + \xi\Delta t)}{r(I_{max})}, \tag{3.13d}$$

where $\xi = 1 - \dfrac{(r(I_{max}) - r(I_{max}-1))}{v\Delta t} = 1 - \dfrac{(\Delta r(I_{max}-1))}{v\Delta t}$.

From (3.13c) and (3.13d), it is clear that the arguments in both functions, f's, are in the similar form if $-\zeta$ and ξ are thought as equivalence. If $E(I_{max}\text{-}1, j, k)^{n-1/2}$ can be described by (3.13c), one can also describe (approximate) $E(I_{max}, j, k)^{n+1/2}$ by utilizing the known values of $E(I_{max}\text{-}1, j, k)^{n-1/2}$ and (3.13d). From (3.13c) and (3.13d), it is evident that the arguments of f's are similar, except the terms $-\zeta\Delta t$ and $\xi\Delta t$ so f's can be defined as follows:

$$f((n\text{-}1/2)\Delta t\text{-}r(I_{max}\text{-}1)/v\text{-}\zeta\Delta t) \equiv f((n\text{-}1/2)\Delta t\text{-}r(I_{max}\text{-}1)/v+\xi\Delta t) \equiv f(u), \tag{3.13e}$$

where u can be either $-\zeta\Delta t$ or $\xi\Delta t$. Thus, we can use $E(I_{max}\text{-}1, j, k)^{(n-1/2)-\zeta}$ and (3.13c) for approximating $E(I_{max}, j, k)^{n+1/2}$ at the outer boundary. The constant ζ can be selected to have different styles of approximations (e.g. interpolations or extrapolations) and the function f's often be chosen to have the order of accuracy equal to the algorithm's. Here, the central-difference approximation is used, which is the second order of accuracy, so the second-order polynomials is chosen for f's (the

higher order polynomials may yield more accurate results but stability of FD-TD algorithms will be rapidly degraded)

$$f(u) = A + Bu + Cu^2, \tag{3.13f}$$

where A, B and C are coefficients to be determined.

In order to interpolate $E(I_{max}, j, k)^{n+1/2}$ by the known field values $E(I_{max}\text{-}1, j, k)^{(n-1/2)-\zeta}$, the following equations, which recasted from (3.13c) in conjunction with the convention in (3.13e), are to be solved simultaneously

$$f(-\zeta_1\Delta t) = A - B\zeta_1\Delta t + C(\zeta_1\Delta t)^2 = r(I_{max}\text{-}1)E(I_{max}\text{-}1, j, k)^{(n-1/2)-\zeta_1}, \tag{3.14a}$$

$$f(-\zeta_2\Delta t) = A - B\zeta_2\Delta t + C(\zeta_2\Delta t)^2 = r(I_{max}\text{-}1)E(I_{max}\text{-}1, j, k)^{(n-1/2)-\zeta_2} \tag{3.14b}$$

and

$$f(-\zeta_3\Delta t) = A - B\zeta_3\Delta t + C(\zeta_3\Delta t)^2 = r(I_{max}\text{-}1)E(I_{max}\text{-}1, j, k)^{(n-1/2)-\zeta_3}. \tag{3.14c}$$

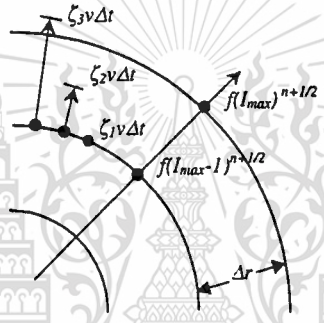

Fig. 3.4 Locations of $f(I_{max})^{n+1/2}$ and $f(I_{max}\text{-}1)^{n+1/2}$, and proper positions of $\zeta_1 v\Delta t$, $\zeta_2 v\Delta t$ and $\zeta_3 v\Delta t$

The constants ζ_1, ζ_2 and ζ_3 must be chosen as shown in Fig.3.4, such that $\zeta_1 v\Delta t$ should be at $I_{max}\text{-}1$ (or inner) surface, $\zeta_3 v\Delta t$ should be at I_{max} (or outer) surface and $\zeta_2 v\Delta t$ is between these two surfaces. Typical values for ζ_1, ζ_2 and ζ_3 (in case of $\Delta r/2v\Delta t = 1$) are -1, 0 and 1, respectively, which yields an interpolation with time. In spherical coordinates, sometimes the ratio $\Delta r/2v\Delta t$ is much greater than 1 (typically, exceeds ten times, so as ζ_3) that leads to inaccurate results. So the less stable, but easy-to-implement, extrapolations are used instead by using $\zeta_1 = -1$, $\zeta_2 = 0$ and $\zeta_3 = 1$ and doing the extrapolation for every time steps.

Once the coefficients A, B and C are determined (from (3.14a) to (3.14c)) $E(I_{max}, j, k)^{n+1/2}$ can be found by applying (3.13f) together with (3.13d)

$$E(I_{max}, j, k)^{n+1/2} = \frac{f(\xi\Delta t)}{r(I_{max})}. \tag{3.15}$$

Another approach is to use linear (first-order polynomial) interpolations which simply utilizing a distance ratio, $r(I_{max}\text{-}1)/r(I_{max})$, but it needs additional (not excessive) computers' storage spaces to store each of the electric field components (i.e. E_θ and E_ϕ) for about $\Delta r/v\Delta t$ time steps in the past. Let $N = \Delta r/v\Delta t$, we can approximate $E(I_{max}, j, k)^{n+1/2}$ by using the $(N\text{-}1)th$ values of the stored $E(I_{max}\text{-}1, j, k)^{n+1/2}$ in the past

$$E(I_{max}, j, k)^{n+1/2} = \frac{r(I_{max}-1)E_{(N-1)}(I_{max}-1, j, k)^{n+1/2}}{r(I_{max})}, \tag{3.16}$$

where the subscript *(N-1)* indicates the *(N-1)th* stored values of $E(I_{max}-1, j, k)^{n+1/2}$ in the past.

3.4 Numerical Stability

The objective of deriving a stability criterion is to have a guiding rule for determining a time step Δt, which can maintain stability of FD-TD algorithms throughout a program run. Here, the derived stability criterion for a nonorthogonal curvilinear FD-TD algorithm is used to derive a stability criterion for a 3-D FD-TD in spherical coordinates.

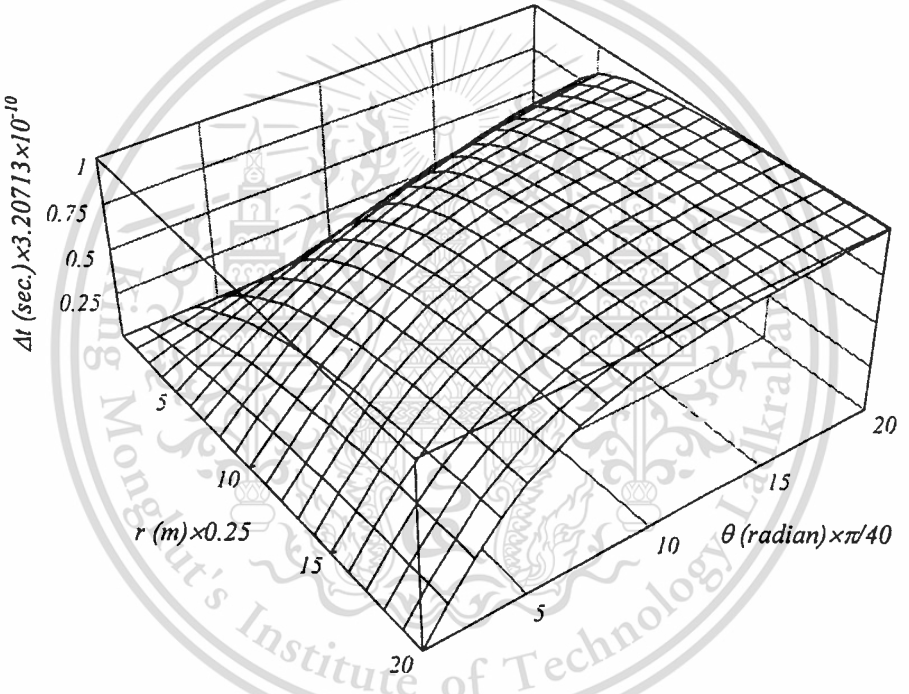

Fig. 3.5 Variation of Δt as function of r and θ

A stability criterion for nonorthogonal curvilinear coordinates is found to be [13]

$$\Delta t \le \frac{1}{v}\sqrt{\frac{g^{i,j}}{\sum_{i=1}^{3}\sum_{j=1}^{3}\Delta u^i \Delta u^j}}, \tag{3.17a}$$

where $g^{i,j}$ is an inverse metric tensor of a metric tensor $g_{i,j}$ and Δu's are increments in directions of coordinate parameters.

In spherical coordinates, and other orthogonal coordinates, $g^{i,j} = g^{i,i} = 1/g_{i,i} = 1/(h_i)^2$ for $i \neq j$ and $g^{i,j} = 0$ for $i = j$. By substituting $\Delta u^1 = \Delta r$, $\Delta u^2 = \Delta\theta$, $\Delta u^3 = \Delta\phi$, $h_1 = 1$, $h_2 = r$ and $h_3 = r\sin\theta$ into (3.17a), we obtain

$$\Delta t \le \frac{1}{v\sqrt{\frac{1}{(\Delta r)^2}+\frac{1}{(r\Delta\theta)^2}+\frac{1}{(r\sin\theta\Delta\phi)^2}}}. \qquad (3.17b)$$

Because its behavior depends on r and θ as shown in Fig.3.5, all parameters in (3.17b) must be determined from the smallest volume cell in problem space to ensure stability. However, the upper limit of Δt which calculated from (3.17b), may not last stability of the algorithms very long. Practically, ones divide Δt (upper limit) by some constant factors such as *5* or *10*, or use one-half of increments (e.g. $\Delta t/2$, $\Delta\theta/2$ and $\Delta\phi/2$) in (3.17b) which stability can be long lasting.

3.5 Numerical Results

To test for the reliability of the algorithm, two problems are considered here. The first problem is done by applying Gaussian pulse sources in the solution region, and using the extrapolation and linear radiation boundary conditions as formulated before at the outer boundary. The second problem is considered by applying continuous wave sources such as infinitesimal electric and magnetic dipoles.

In the first problem, a Gaussian pulse source is applied

$$\overline{f}(r;t) = \overline{a}_i I_o \exp\left[\frac{-(t-r/v-t_o)^2}{\tau^2}\right], \qquad (3.18a)$$

where $\overline{a}_i$, I_o, t_o and τ are unit vector, amplitude, time delay and pulsewidth, respectively.

Consider an electric dipole aligned along z-axis at the origin and the configurations of parameters are as follows: $R_{max} = 10$ m, $\Delta r = 0.5$ m ($I_{max} = 20$), $\Delta\theta = \pi/12$ radian (15°, $J_{max} = 12$), $\Delta\phi = \pi/9$ radian (20°, $K_{max} = 18$) and $\tau = 2\times10^{-8}$. The corresponding electric field components are found to be [7]

$$E_r = \frac{\cos\theta}{2\pi\varepsilon_o}\left[\frac{f'(t-r/v)}{r^2 v}+\frac{f(t-r/v)}{r^2}\right], \qquad (3.18b)$$

$$E_\theta = \frac{\sin\theta}{4\pi\varepsilon_o}\left[\frac{f''(t-r/v)}{rv^2}+\frac{f'(t-r/v)}{r^2 v}+\frac{f(t-r/v)}{r^3}\right], \qquad (3.18c)$$

where f' and f'' represent the first and second derivatives of f, respectively. By applying (3.18c) as electric-field boundary condition for E_θ in the algorithm at $i = 4$ ($r = 2$ m), $\Delta t \approx 1.85\times10^{-11}$ *seconds* (from (3.17b)) and using $t_o = 6\times10^{-8}$ seconds, the results are shown in Fig.3.6(a) and Fig.3.6(b) at $r = 10$ m ($i = I_{max}$) and $\theta = 97.5°$. In Fig.3.6(a) and Fig.3.6(b), a second-order extrapolating and a linear interpolating RBCs, respectively, has been used which are shown by the fine dash lines (with labeling *no extended cell*).

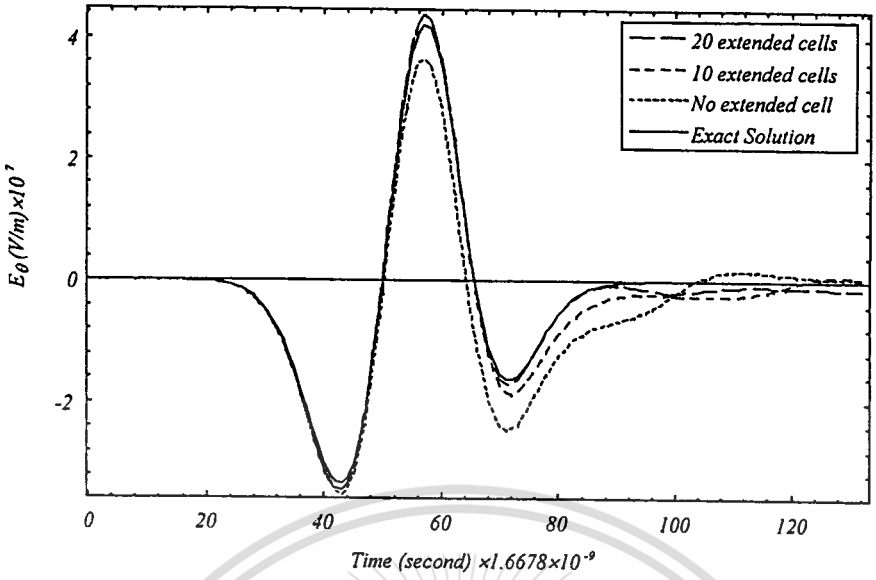

Fig. 3.6(a) E_θ detected at $r=20$ m and $\theta=97.5°$, excited by the electric dipoles (Gaussian pulse) and using the second-order extrapolating RBC at the outer boundary

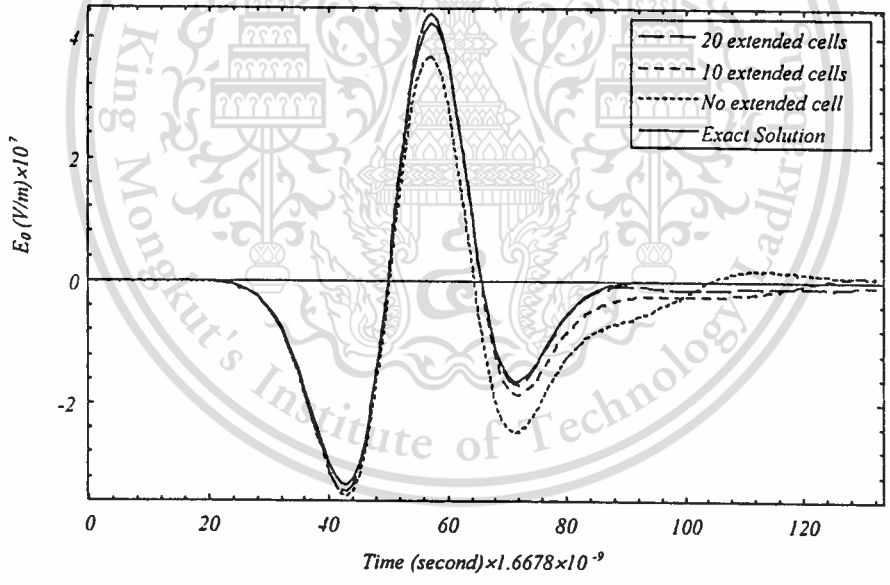

Fig. 3.6(b) E_θ detected at $r=20$ m and $\theta=97.5°$, excited by the electric dipoles (Gaussian pulse) and using the linear interpolating RBC at the outer boundary

It is evident that both alternative RBCs yield similar results and comparable with those in [7] using second-order interpolating RBCs. Furthermore, the effects of RBCs on results are studied by adding *10* and *20* extended cells between an $i = 20$ surface (where the results are detected) and a RBC surface (where extrapolations and interpolations are performed). It is seen in Fig.3.6(a) and Fig.3.6(b) that the further the approximating RBCs are taken away from the point of detection, the better results are achieved (but one should note that increasing spacing cells more than *20* (I_{max}) will not yield much better results).

In case of magnetic dipole, the corresponding electric field component is found to be [7]

$$E_\phi = -\frac{\sin\theta}{4\pi r}\left[\frac{f''^*(t-r/v)}{v} + \frac{f'^*(t-r/v)}{r}\right], \tag{3.18d}$$

where f'^* and f''^* are complex conjugates of the first and second derivatives of f, respectively.

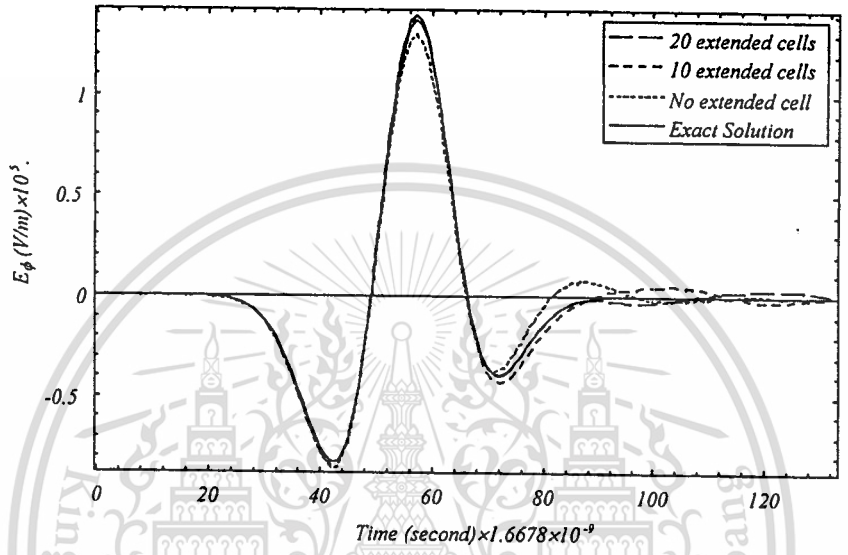

Fig. 3.7(a) E_ϕ detected at $r=20$ m and $\theta = 90°$, excited by the magnetic dipoles (Gaussian pulse) and using the second-order extrapolating RBC at the outer boundary

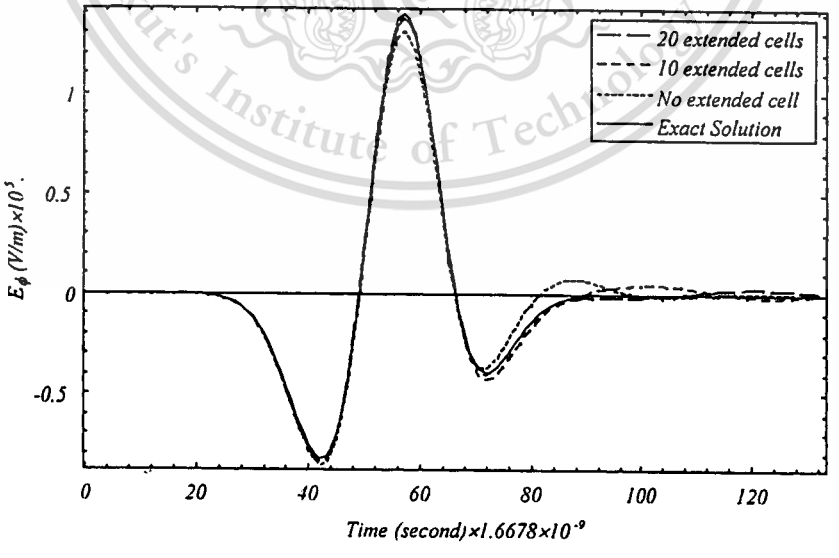

Fig. 3.7(b) E_ϕ detected at $r=20$ m and $\theta = 90°$, excited by the magnetic dipoles (Gaussian pulse) and using the linear interpolating RBC at the outer boundary

By applying (3.18d) as electric-field boundary condition for E_ϕ in the algorithm and using the same values of parameters as defined before, the results obtained are shown in Fig.3.7(a) and Fig.3.7(b). Again, a second-order extrapolating and a linear interpolating RBCs are applied and yield results in Fig.3.7(a) and Fig.3.7(b), respectively. Effects of RBCs on results can be concluded as in case of electric dipole. Evidently, the algorithm behaves better for the case of magnetic dipole.

In the second problem, the continuous wave are excited by utilizing equations derived for an infinitesimal dipole. A corresponding electric field excited by current source as

$$\bar{I} = \bar{a}_z I_o \cos(\omega t). \tag{3.19a}$$

In θ-direction, E_θ, is found to be [24]

$$E_\theta = \frac{I_o d\eta \sin\theta}{4\pi r}\left[\frac{\cos\omega(t-r/v)}{r} + \frac{k\sin\omega(t-r/v)}{r^2} - \frac{\sin\omega(t-r/v)}{k}\right], \tag{3.19b}$$

where d, η and k are, respectively, length of a dipole, wave impedance and wave number (phase constant). The operating frequency is chosen to be *30* MHz and $I_o = 40\pi r/d\eta$. The values of other parameters are $R_{max} = 40$ m, $\Delta r = 1$ m $(I_{max} = 40)$, $\Delta\theta = \pi/12$ radian *(15°, $J_{max} = 12$)* and $\Delta\phi = \pi/9$ radian *(20°, $K_{max} = 18$)*. By applying (3.19b) in the algorithm as boundary condition for the field component, E_θ, yields results as shown in Fig.3.8(a) (at $r = 40$ m and $\theta = 97.5°$). For the case of infinitesimal magnetic dipole, the corresponding electric field component, E_ϕ, produced is [24]

$$E_\phi = -\frac{I_o d\eta \sin\theta}{4\pi r}\left[\frac{\cos\omega(t-r/v)}{r} - k\sin\omega(t-r/v)\right]. \tag{3.19c}$$

The same procedures as in the infinitesimal electric dipole are done for case of infinitesimal magnetic dipole, using the same values of the parameters, by applying (3.19c) to the algorithm as boundary condition for the field component, E_ϕ, yields results as shown in Fig.3.8(b). As seen in Fig.3.8(a) and Fig.3.8(b), both electric and magnetic dipoles have the similar behavior when compare with their exact solutions. Furthermore, the additional (extended) cells and different types of RBCs like in the first problem have been tried, but the results are not better than that shown in Fig.3.8(a) and Fig.3.8(b).

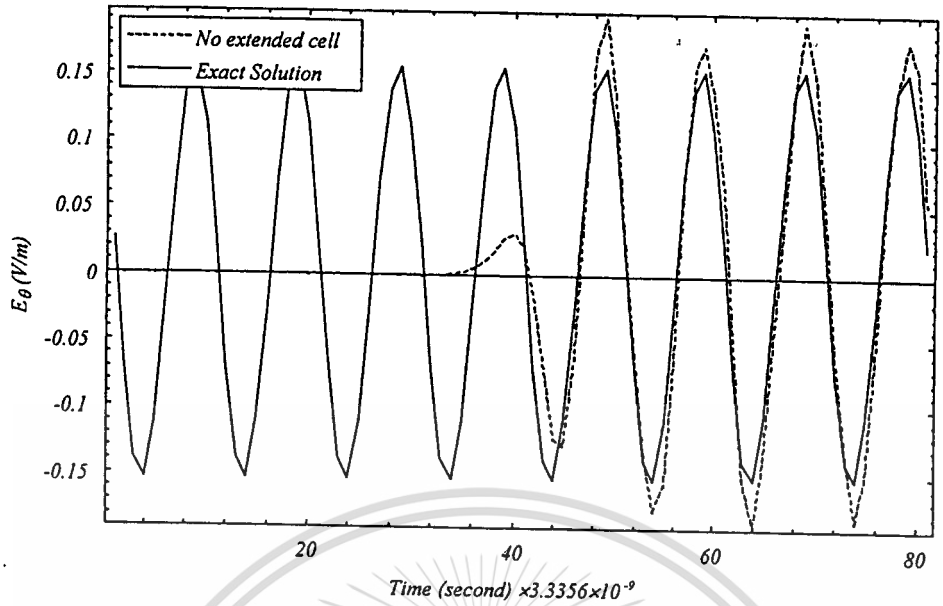

Fig. 3.8(a) E_θ detected at $r=40$ m and $\theta = 97.5°$, excited by the infinitesimal electric dipoles

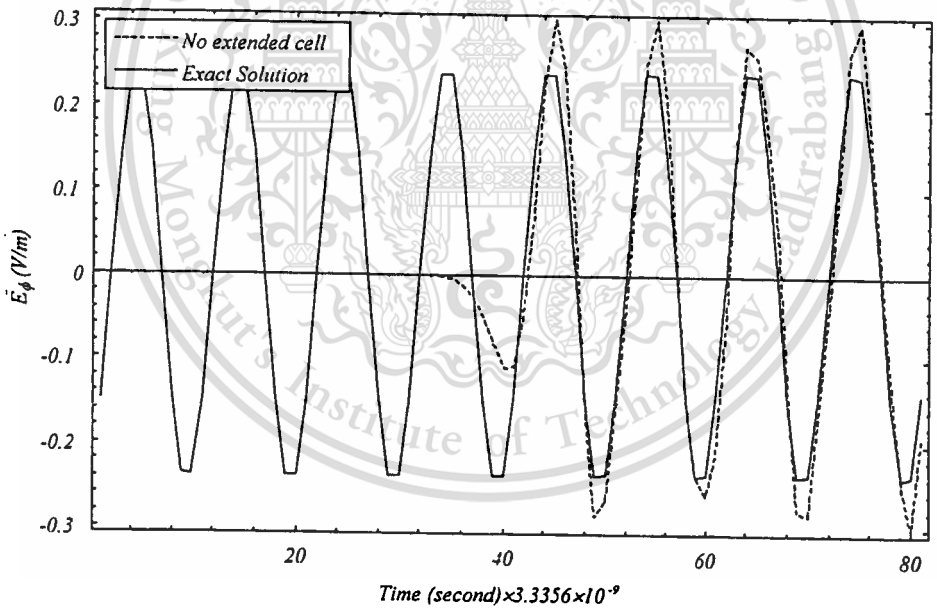

Fig. 3.8(b) E_ϕ detected at $r=40$ m and $\theta = 90°$, excited by the infinitesimal magnetic dipoles

3.6 Conclusions

The construction of FD-TD equations for spherical coordinates are accomplished by using the similar procedures to that for rectangular coordinates. However, the important dissimilar point is that FD-TD algorithms in spherical coordinates contain singularities. The three main singularities occur at the prime meridian, the poles and the origin. The first one can be treated by using simple joining conditions, while the others need more sophisticate integral approximations. Besides the extra treatments for singularities, the extra conditions (radiation boundary

conditions) must also be applied at the outermost boundary to properly truncate the computations. The introduced RBCs are the second-order extrapolation and the linear interpolation. From the numerical results, the two alternative RBCs yield good approximations at the truncated surface when compared with the previous work [7]. Also, it can be concluded that using this FD-TD algorithm with problems involving magnetic dipole sources yields better results than those with electric dipole sources, but this may be true only for cases of pulse sources. In cases of continuous wave sources (infinitesimal dipoles), it is not observable that the problems involving magnetic dipole sources behaved better than those involving electric dipole sources. From these results, it can be concluded that continuous wave sources are immune to certain types of RBCs. Effects of simulating RBCs on the calculated field components in cases of pulse sources are more serious than those in cases of continuous wave sources. However, in cases of pulse sources, results can be improved by adding extended cells whereas in events of continuous sources the results can not be improved by these means. Also included in this chapter, the stability criterion for the 3-D FD-TD algorithms in spherical coordinates is derived from the criterion of the nonorthogonal coordinates. Ultimately, it has been suggested that using one-halves of the increments (i.e. $\Delta t/2$, $\Delta\theta/2$ and $\Delta\phi/2$) in the derived stability equation yields good stability.

Chapter 4

Electromagnetic Field Analysis inside Cavities of Spherical Geometry in Source-Free Region

The formulated FD-TD algorithm in spherical coordinates is utilized to numerically analyze electromagnetic fields inside three configurations of cavities: a conducting segmented cavity (Fig.4.1(a)), a concentric conducting spherical cavity enclosed by a conducting conical surface (Fig.4.1(b)) and a conducting spherical cavity (Fig.4.1(c)). The analysis will be done in source-free region, assuming that all field components inside cavities are changing simultaneously in every time step. The method of applying source is implemented by simply adding small amount of sinusoidal waves to some proper field components, for the whole region of cavities. After numerical processes, the resulting mode patterns in the cavities will be compared with the analytical solutions. To check whether the derived algorithm works well with cavity problems.

Generally, there are three steps in modeling a cavity by using the FD-TD method. Firstly, use analytical solutions (here, spherical wave) to find the dimensions of a resonant cavity of a desired mode and dimensional configurations. Secondly, compute FD-TD parameters using proper resolutions that based on wavelength. Finally, match boundary conditions for FD-TD electric and magnetic field unknowns by referring to the configurations of the designed cavity. The last step also includes considerations of singularities and treatments.

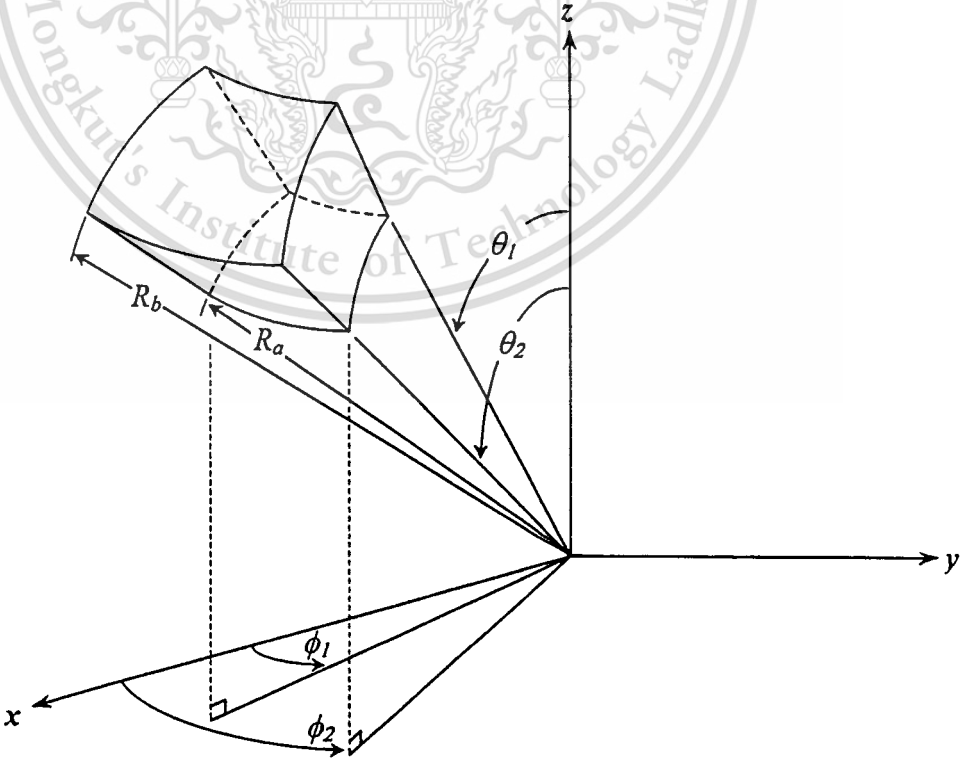

Fig. 4.1(a) A spherical segmented cavity

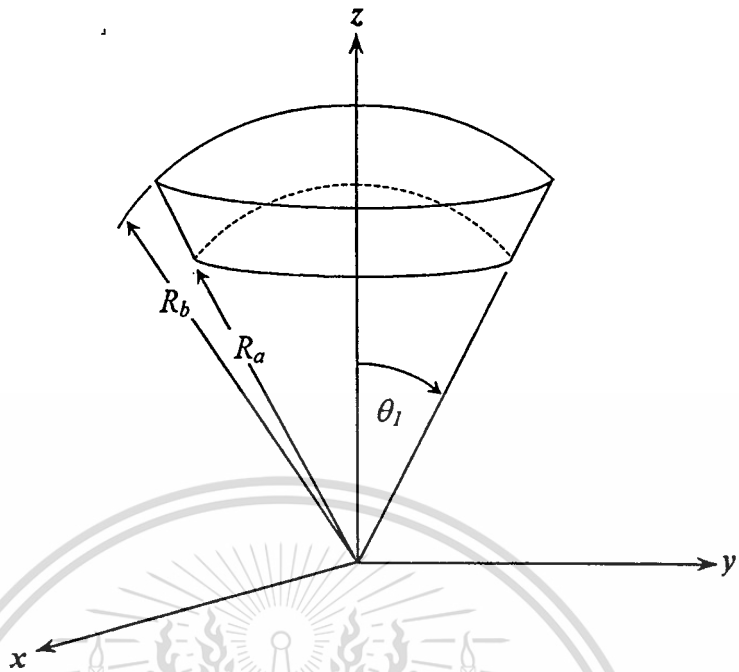

Fig. 4.1(b) A concentric spherical cavity enclosed by a conical surface

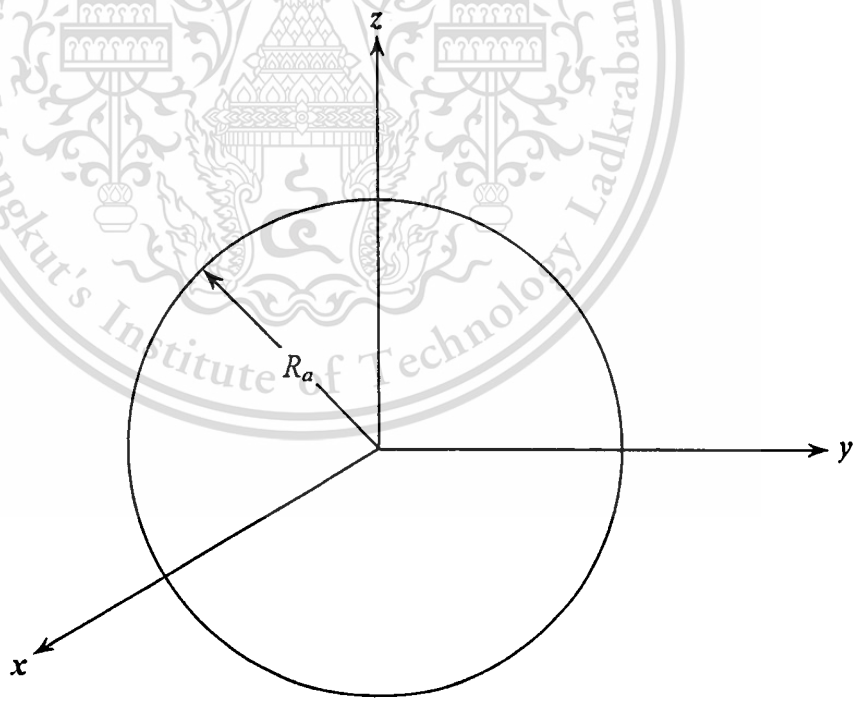

Fig. 4.1(c) A spherical cavity

4.1 Analytical solutions of spherical wave

As mentioned above, one must determine dimensions of the desired cavity before proceed in FD-TD simulations. Thus, it is convenient to consider the analytical solutions of spherical wave, first. It is well-known that only the TE^r and

TM^r waves exist in this geometrical configuration. The TE^r wave solution is found [25-28] to be

$$E_r = 0, \tag{4.1a}$$

$$E_\theta = -\frac{m}{\varepsilon\ r\sin\theta}\tilde{B}_n(kr)L_n^m(\cos\theta)\frac{df(m\phi)}{d\phi}, \tag{4.1b}$$

$$E_\phi = \frac{1}{\varepsilon\ r}\tilde{B}_n(kr)\frac{dL_n^m(\cos\theta)}{d\theta}f(m\phi), \tag{4.1c}$$

$$H_r = \frac{1}{j\omega\mu\varepsilon}\left(\frac{d^2}{dr^2}+k^2\right)\tilde{B}_n(kr)L_n^m(\cos\theta)f(m\phi), \tag{4.1d}$$

$$H_\theta = \frac{1}{j\omega\mu\varepsilon\ r}\frac{d\tilde{B}_n(kr)}{dr}\frac{dL_n^m(\cos\theta)}{d\theta}f(m\phi), \tag{4.1e}$$

$$H_\phi = \frac{1}{j\omega\mu\varepsilon\ r\sin\theta}\frac{d\tilde{B}_n(kr)}{dr}L_n^m(\cos\theta)\frac{df(m\phi)}{d\phi}. \tag{4.1f}$$

Also, the TM^r wave solution is obtained as

$$E_r = \frac{1}{j\omega\mu\varepsilon}\left(\frac{d^2}{dr^2}+k^2\right)\tilde{B}_n(kr)L_n^m(\cos\theta)f(m\phi), \tag{4.2a}$$

$$E_\theta = \frac{1}{j\omega\mu\varepsilon\ r}\frac{d\tilde{B}_n(kr)}{dr}\frac{dL_n^m(\cos\theta)}{d\theta}f(m\phi), \tag{4.2b}$$

$$E_\phi = \frac{1}{j\omega\mu\varepsilon\ r\sin\theta}\frac{d\tilde{B}_n(kr)}{dr}L_n^m(\cos\theta)\frac{df(m\phi)}{d\phi}, \tag{4.2c}$$

$$H_r = 0, \tag{4.2d}$$

$$H_\theta = \frac{m}{\mu\ r\sin\theta}\tilde{B}_n(kr)L_n^m(\cos\theta)\frac{df(m\phi)}{d\phi}, \tag{4.2e}$$

$$H_\phi = -\frac{1}{\mu\ r}\tilde{B}_n(kr)\frac{dL_n^m(\cos\theta)}{d\theta}f(m\phi). \tag{4.2f}$$

For problems involving cavities, $\tilde{B}_n$, L_n^m and f should be defined in forms of standing wave functions as follows:

$$\tilde{B}_n(kr) = A\tilde{J}_n(kr) + B\tilde{Y}_n(kr), \tag{4.3a}$$

$$L_n^m(\cos\theta) = CP_n^m(\cos\theta) + DQ_n^m(\cos\theta), \tag{4.3b}$$

$$f(m\phi) = E\cos(m\phi) + F\sin(m\phi), \tag{4.3c}$$

where $\tilde{J}_n$ and $\tilde{Y}_n$ are the Schelkunoff spherical Bessel functions of the first and second kind, respectively. P_n^m and Q_n^m are, respectively, the associated Legendre functions of the first and second kind of the cosine function. *A, B, C, D, E* and *F* are constants that can be determined by matching boundary conditions.

In order to determine dimensions of resonant cavities (R_a, R_b, θ_1, θ_2, ϕ_1 and ϕ_2), the boundary conditions must be applied. For the case of TE^r wave, the following procedures show one possible way to get those dimensional parameters for the desired wave mode.

In radial direction, for a spherical segmented cavity and a concentric spherical cavity enclosed by a conical surface, E_θ, E_ϕ and H_r must vanish at the perfectly electric conductor (PEC) surfaces; when $r = R_a$ and R_b. Thus a condition is obtained as

$$-\frac{A}{B} = \frac{\tilde{Y}_n(kR_a)}{\tilde{J}_n(kR_a)} = \frac{\tilde{Y}_n(kR_b)}{\tilde{J}_n(kR_b)}. \tag{4.4a}$$

By solving the right-most equation of (4.4a), the dimensions, R_a and R_b can be determined. For a spherical cavity, the $\tilde{Y}_n$ function in (4.4a) should be vanished. Thus only the parameter R_a needs to be determined by solving the following equation,

$$\tilde{J}_n(kR_a) = 0. \tag{4.4b}$$

In θ-direction, E_o and H_θ at the PEC surfaces, $\theta = \theta_1$ and θ_2, must disappear. One obtains

$$-\frac{C}{D} = \frac{\left.\frac{\partial}{\partial\theta} Q_n^m(\cos\theta)\right|_{\theta=\theta_1}}{\left.\frac{\partial}{\partial\theta} P_n^m(\cos\theta)\right|_{\theta=\theta_1}} = \frac{\left.\frac{\partial}{\partial\theta} Q_n^m(\cos\theta)\right|_{\theta=\theta_2}}{\left.\frac{\partial}{\partial\theta} P_n^m(\cos\theta)\right|_{\theta=\theta_2}}. \tag{4.5a}$$

Similarly, the dimensional parameters for a segmented cavity, θ_1 and θ_2 can be obtained by solving (4.5a) which yields resonance in θ-direction. Additionally, for a concentric spherical cavity enclosed by a conical surface, the Q_n^m functions should be enforced to be zero. Hence, only the θ_1 parameter is to be solved from

$$\left.\frac{\partial}{\partial\theta} P_n^m(\cos\theta)\right|_{\theta=\theta_1} = 0. \tag{4.5b}$$

In ϕ-direction, for the case of segmented cavity, E_θ and H_ϕ at the surfaces, $\phi = \phi_1$ and ϕ_2, must vanish. This yields

$$-\frac{E}{F}=\frac{\left.\frac{\partial}{\partial\phi}sin(m\phi)\right|_{\phi=\phi_1}}{\left.\frac{\partial}{\partial\phi}cos(m\phi)\right|_{\phi=\phi_1}}=\frac{\left.\frac{\partial}{\partial\phi}sin(m\phi)\right|_{\phi=\phi_2}}{\left.\frac{\partial}{\partial\phi}cos(m\phi)\right|_{\phi=\phi_2}}. \tag{4.6}$$

Again, by solving (4.6), the parameters ϕ_1 and ϕ_2 can be obtained, which yield resonance in ϕ-direction. For a spherical cavity and a concentric spherical cavity enclosed by a conical surface, one can freely select either $sin(m\phi)$ or $cos(m\phi)$ as a solution in ϕ-direction, to obtain an odd mode or an even mode, respectively.

Similar to the case of TE^r wave, dimensions of cavities for handling TM^r wave can be determined by the following procedures. In radial direction, for a segmented cavity and a concentric spherical cavity enclosed by a conical surface, E_θ and E_ϕ must vanish at the PEC surfaces; when $r = R_a$ and R_b. Thus a condition is obtained as

$$-\frac{A}{B}=\frac{\left.\frac{\partial}{\partial r}\tilde{Y}_n(kr)\right|_{r=R_a}}{\left.\frac{\partial}{\partial r}\tilde{J}_n(kr)\right|_{r=R_a}}=\frac{\left.\frac{\partial}{\partial r}\tilde{Y}_n(kr)\right|_{r=R_b}}{\left.\frac{\partial}{\partial r}\tilde{J}_n(kr)\right|_{r=R_b}}. \tag{4.7a}$$

By solving equation of (4.7a), one will get the dimensions, R_a and R_b. For a spherical cavity, again, the $\tilde{Y}_n$ function should be vanished. Thus only the parameter R_a needs to be determined by solving the following equation,

$$\left.\frac{\partial}{\partial r}\tilde{J}_n(kr)\right|_{r=R_a}=0. \tag{4.7b}$$

In θ-direction, E_r, E_o and H_θ at the PEC surfaces, $\theta = \theta_1$ and θ_2, must vanish. One obtained

$$-\frac{C}{D}=\frac{Q_n^m(cos\theta_1)}{P_n^m(cos\theta_1)}=\frac{Q_n^m(cos\theta_2)}{P_n^m(cos\theta_2)}. \tag{4.8a}$$

Then the dimensional parameters for a segmented cavity, θ_1 and θ_2, can be obtained by solving (4.8a) which yield resonance in θ-direction. For a concentric spherical cavity enclosed by a conical surface, again, the Q_n^m functions should be enforced to be zero. Hence, only the θ_1 parameter is to be determined from

$$P_n^m(cos\theta_1)=0. \tag{4.8b}$$

In ϕ-direction, for a spherical segmented cavity, E_r, E_θ and H_ϕ at the PEC surfaces, $\phi = \phi_1$ and ϕ_2, must vanish. This yields

$$-\frac{E}{F} = \frac{sin(m\phi_1)}{cos(m\phi_1)} = \frac{sin(m\phi_2)}{cos(m\phi_2)}. \tag{4.9}$$

By solving (4.9), the parameters ϕ_1 and ϕ_2 can be obtained, which yield resonance in ϕ-direction. Additionally, for a spherical cavity and a concentric spherical cavity enclosed by a conical surface, either $sin(m\phi)$ or $cos(m\phi)$ can be freely selected as a solution in ϕ-direction to get an odd mode or an even mode, respectively.

After all the dimensional parameters have been determined, the designed cavities are now ready to be discretized and embedded in the FD-TD spaces.

4.2 Conducting Segmented Cavity

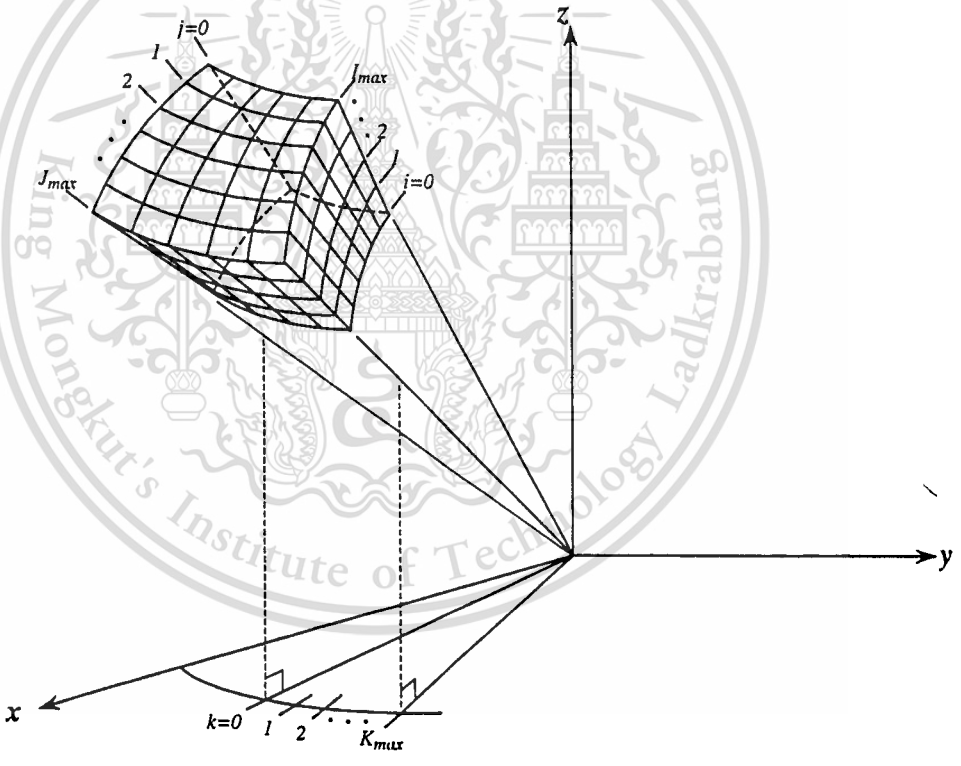

Fig. 4.2(a) A subdivided spherical segmented cavity

After the dimensional parameters, R_a, R_b, θ_1, θ_2, ϕ_1 and ϕ_2, are calculated. The designed segmented cavity is subdivided into many volume cells as shown in Fig.4.2 (a), which the FD-TD space parameters, Δr, $\Delta\theta$, $\Delta\phi$, I_{max}, J_{max} and K_{max}, can be obtained by using the dimensional parameters of the cavity. Then, the FD-TD time parameter, Δt, can be estimated by using (3.17b).

Since all field components propagate in radial direction, the parameter Δr usually be approximated based on wavelength as shown below,

$$\Delta r \approx \frac{\lambda}{N}, \tag{4.10a}$$

where N is number of sampling points per wavelength in radial direction. The maximum value of the index i (I_{max}) can be determined from the approximate value of Δr together with the dimensional parameters, R_a and R_b, from the previous section as follows:

$$I_{max} = Int\left(\frac{R_b - R_a}{\Delta r}\right) + 1. \tag{4.10b}$$

The $Int(\cdot)$ is the greatest integer function. The above equation is added by one to ensure that the FD-TD space increment will be less than or equal to the specified resolution. The maximum values of the indices j (J_{max}) and k (K_{max}) can be any proper integer values depending on the desired accuracy and the chosen solution from (4.5a) through (4.6) or (4.8a) through (4.9). For example, in ϕ-direction (4.6), if the mode parameter $m=3$ and the third solution is chosen (a complete cycle of sinusoidal wave is expected in that direction), so K_{max} should have value greater than or equal to 2 (from the Nyquist's sampling theory). However, in sense of the practical FD-TD method, the number of sampling points should be at least about 5 per wavelength of sinusoidal wave to get reasonable results [11]. After the maximum indices are found, the exact FD-TD space increments can be computed by using

$$\Delta r = \frac{R_b - R_a}{I_{max}}, \quad \Delta\theta = \frac{\theta_2 - \theta_1}{J_{max}}, \quad \Delta\phi = \frac{\phi_2 - \phi_1}{K_{max}}. \tag{4.10c}$$

Finally, the time increment Δt can be estimated by substituting the calculated space increments in a numerical stability equation for spherical coordinates (3.17b).

Furthermore, the boundary conditions of all field components (E_r, E_θ, E_ϕ, H_r, H_θ and H_ϕ) at the surfaces of cavity must be considered. The six field components on the FD-TD grid cell interfacing the PEC boundaries of the cavity is shown in Fig.4.2(b). From the PEC boundary conditions in conjunction with referring to Fig.4.2(b), one can easily obtain boundary conditions for the FD-TD field unknowns at the six PEC surfaces of the cavity, as introduced below,

$$E_r\Big|_{j=0,J_{max}\,or\,k=0,K_{max}} = 0, \tag{4.11a}$$

$$E_\theta\Big|_{i=0,I_{max}\,or\,k=0,K_{max}} = 0, \tag{4.11b}$$

$$E_\phi\Big|_{i=0,I_{max}\,or\,j=0,J_{max}} = 0, \tag{4.11c}$$

$$H_r\Big|_{i=0,I_{max}} = 0, \tag{4.11d}$$

$$H_\theta\Big|_{j=0,J_{max}} = 0, \tag{4.11e}$$

$$H_\phi\big|_{k=0,K_{max}} = 0. \qquad (4.11f)$$

These conditions must be inserted into FD-TD codes while simulating fields resonating in the cavity. Note that the conditions may have different forms for different styles of positioning the six field components.

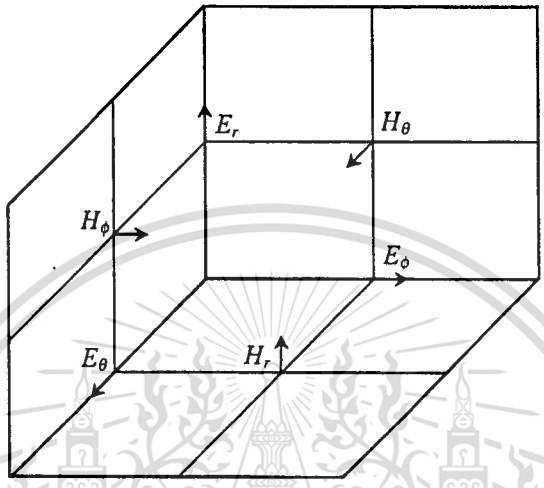

Fig. 4.2(b) The six field components on PEC surfaces

Table 4.1 The first five solutions to (4.4a), (4.5a) and (4.6); TE_{35} and $R_a/R_b = \theta_1/\theta_2 = \phi_1/\phi_2 = 1/5$.

Solution number	R_b *(m)*	θ_2 *(radian)*	ϕ_2 *(radian)*
1	*1.4890377*	*0.8183079*	*0.0000000*
2	*2.0640161*	*1.5589602*	*1.3089969*
3	*2.6056014*	*2.2394676*	*2.6179939*
4	*3.1395723*	-	*3.9269908*
5	*3.6789316*	-	*5.2359876*

As a numerical example, consider a TE_{35} wave mode resonates in an air-filled conducting segmented cavity. By substituting $mn = 35$ and the ratios $R_a/R_b = \theta_1/\theta_2 = \phi_1/\phi_2 = 1/5$ (for simplicity) to the analytical equations (4.4a), (4.5a) and (4.6), the first five solutions of the dimensional parameters R_b, θ_2 and ϕ_2 can be obtained as shown in Table 4.1. When a set of solutions is selected, one can further determine the left parameters R_a, θ_1 and ϕ_1. Let us choose the first practical solutions from Table 4.1. Hence, all dimensional parameters have values as follows: $R_a = 0.2978075$ *m*,

$R_b = 1.4890377\ m$, $\theta_1 = 0.1636616\ radian$, $\theta_2 = 0.8183079\ radian$, $\phi_1 = 0.2617994\ radian$ and $\phi_2 = 1{,}3089969\ radian$. From the calculated dimensional parameters and the discussion above (about determination of the FD-TD parameters ((4.10a) through (4.10c)), the FD-TD space parameters can be obtained as follows: $I_{max} = 6$, $J_{max} = 5$, $K_{max} = 8$, $\Delta r = 0.1985384\ m$, $\Delta\theta = 0.1309293\ radian$ and $\Delta\phi = 0.1308997\ radian$. In this case, five sampling points per wavelength ($N = 5$) is chosen. From the FD-TD space parameters and (3.17b), the time increment Δt can be estimated to be about 6×10^{-13} *seconds* (after backed off). At this point, all FD-TD parameters have been determined. It is left only a source condition to simulate the source-free region. As has been mentioned before at the beginning part of the chapter, the source-free region is achieved by recursively adding small amount of sinusoidal waves to some proper field components for the entire volume of the cavity. Thus, this can simulate simultaneous changes of all waves with time. The source condition can be simply written in form of a programming notation as

$$V(i,j,k)^{n-1} + sin(\omega n\Delta t) \rightarrow V(i,j,k)^n, \tag{4.12a}$$

where V is any proper field component. The arrow indicates *recursive* summation. Alternatively, if the large amount (amplitude) of sinusoidal waves is applied, the better source condition as introduced in [11] is considered. In this new condition, the process of adding source condition is similar to (4.12a) except that the sinusoidal function is replaced by the *ramped sine* as shown below,

$$ramped\ sine = \begin{cases} \dfrac{t\sin(\omega n\Delta t)}{mT}, & 0 \le t \le mT \\ \sin(\omega n\Delta t), & t > mT \end{cases}, \tag{4.12b}$$

where m is number of damped periods (T), and should not be confused with the m of wave mode. A typical value $m = 3$ is suggested in [11]. Moreover, good results are expected if V is chosen to be the E_θ or H_ϕ. This is true because the sinusoidal function is the solution in ϕ-direction, and the positions of both E_θ and H_ϕ in the subdivided solution region are exactly terminated at $k = 0$ and K_{max}.

In the FD-TD computations, the normalized wavelength ($\lambda=1$) is used, here. After about four periods of the applied sinusoidal wave, the mode patterns inside the segmented cavity, at $i = 4$, $j = 3$ and $k = 5$, are shown along with the analytical solutions in Fig.4.3 through Fig.4.7. From the figures, it is evident that the FD-TD solutions are very close to those from analytical method, although the solution region is subdivided into only 6×5×8 cells. Furthermore, all errors are found to be about 5-10%, when compared with the analytical results. However, it is found that the results in r- and θ-direction are less accurate than in ϕ-direction. This may be because of the severely nonlinear behavior of the algorithm near the origin and the pole ($\theta=0°$). The behavior can be illustrated, by varying r and θ (or indices i and j) in (3.17b), as shown in Fig.3.5. This can be cured by dividing up more volume cells near the singular points; however, this approach may effect stability of calculations and waste of time. Sometimes, using the higher-order (e.g. forth-order) algorithm is an alternative but it increases complexity and resource requirement.

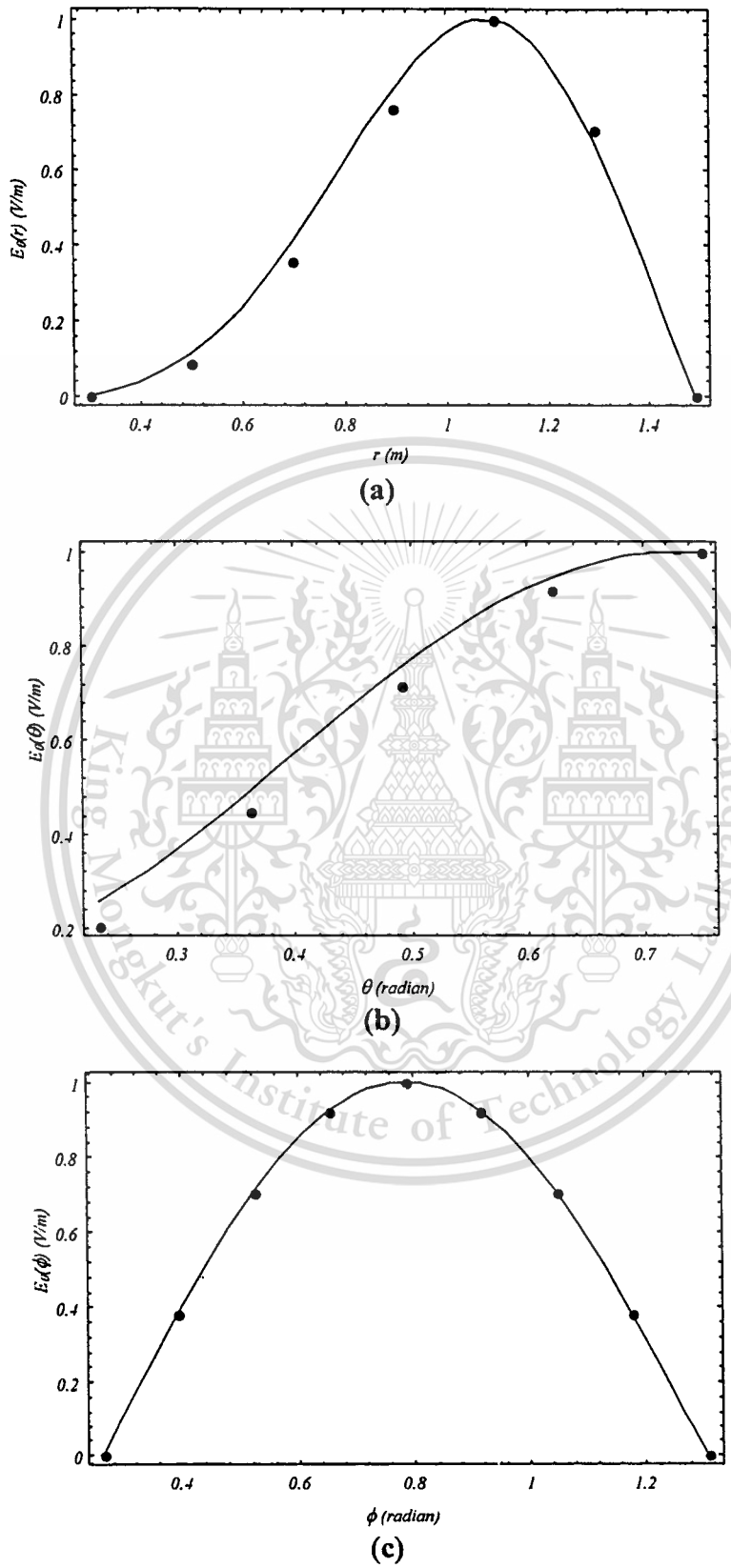

Fig. 4.3 Normalized E_θ : **(a)** in r-direction, **(b)** in θ-direction and **(c)** in ϕ-direction
• FD-TD solution — Analytical solution

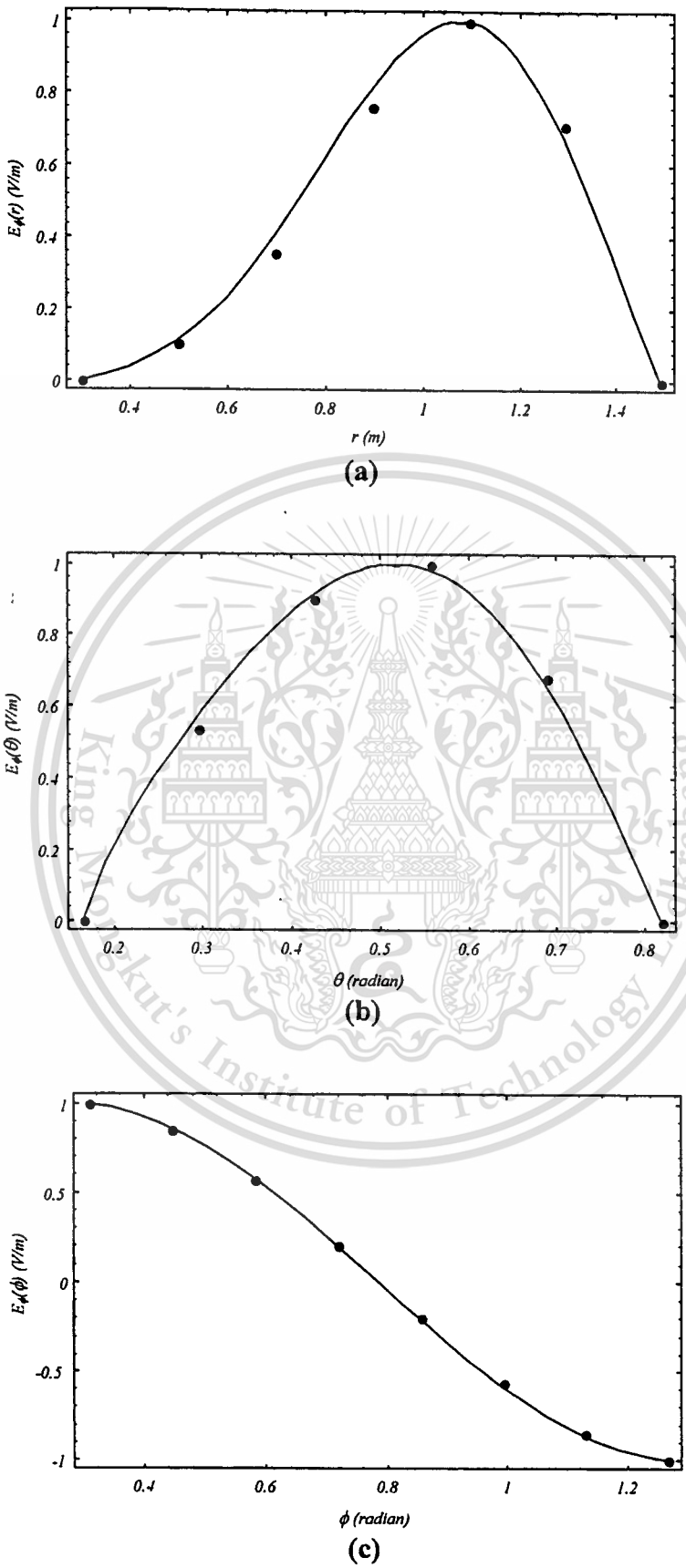

Fig. 4.4 Normalized E_ϕ : **(a)** in r-direction, **(b)** in θ-direction and **(c)** in ϕ-direction
• FD-TD solution — Analytical solution

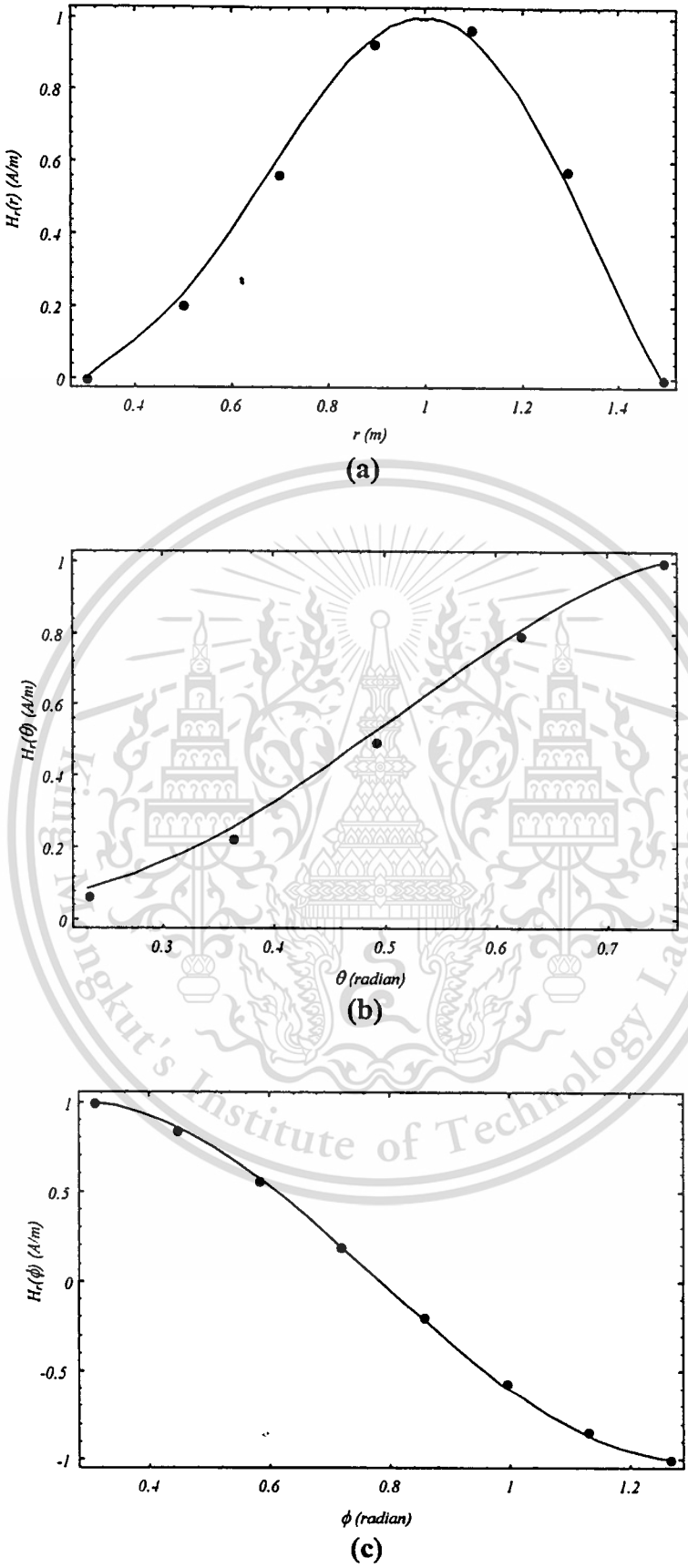

Fig. 4.5 Normalized H_r : **(a)** in r-direction, **(b)** in θ-direction and **(c)** in ϕ-direction
• FD-TD solution — Analytical solution

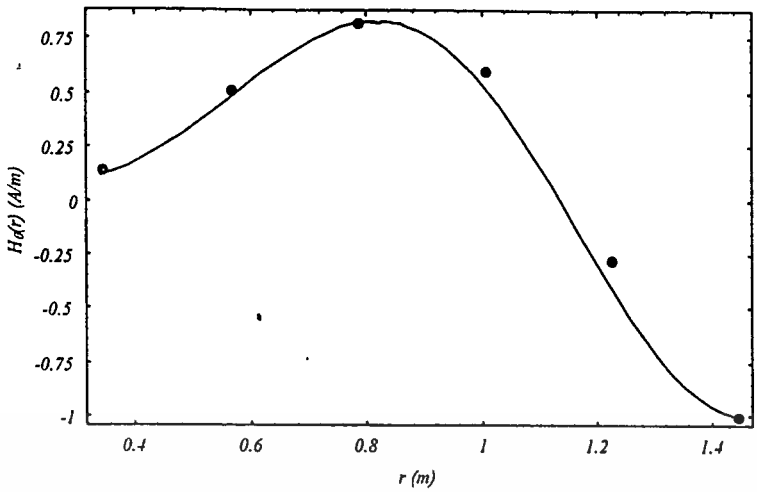

(a)

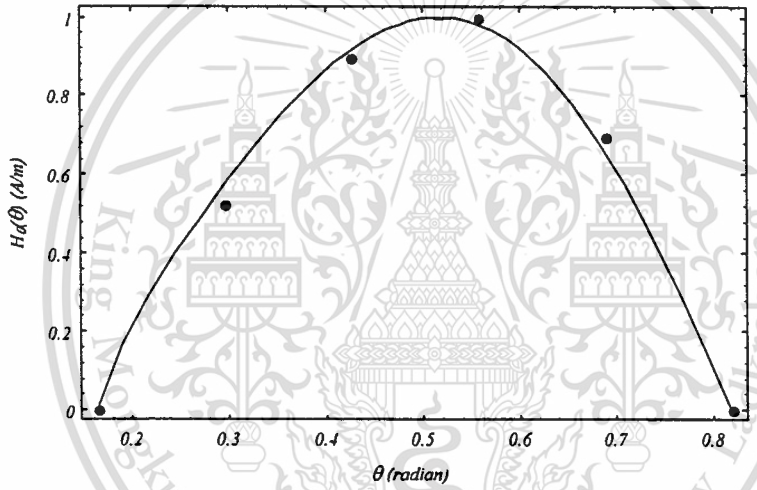

(b)

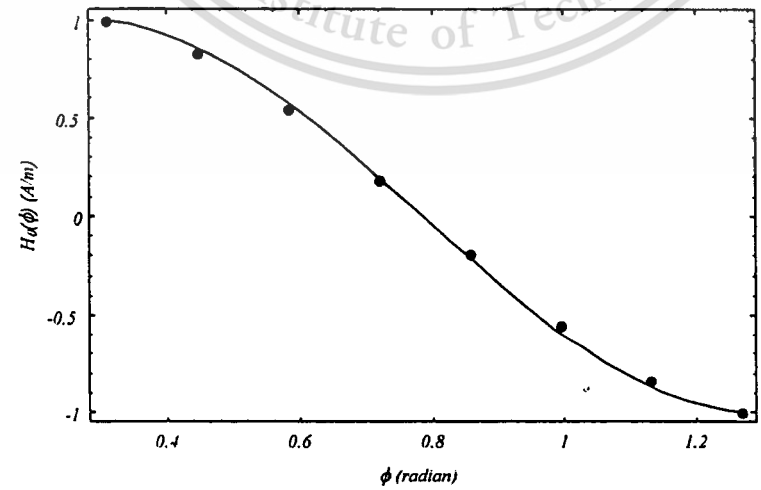

(c)

Fig. 4.6 Normalized H_θ : **(a)** in r-direction, **(b)** in θ-direction and **(c)** in ϕ-direction
• FD-TD solution — Analytical solution

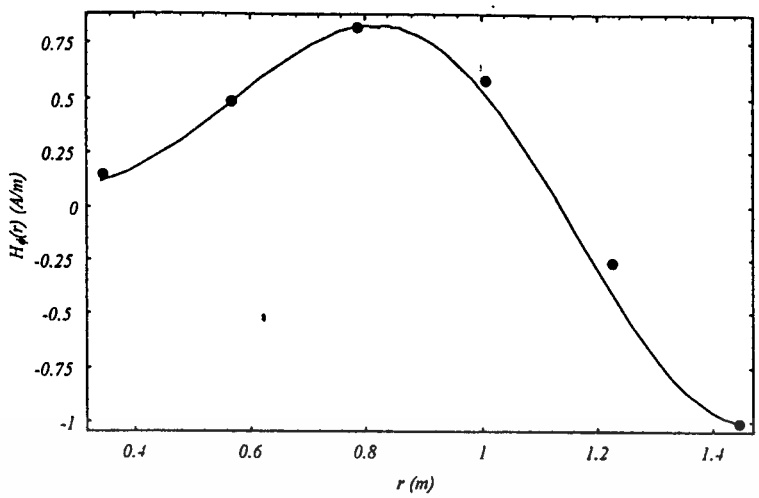

(a)

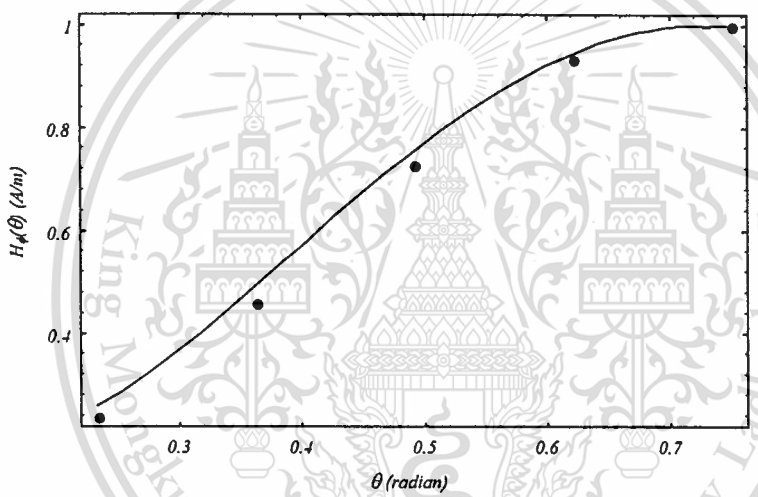

(b)

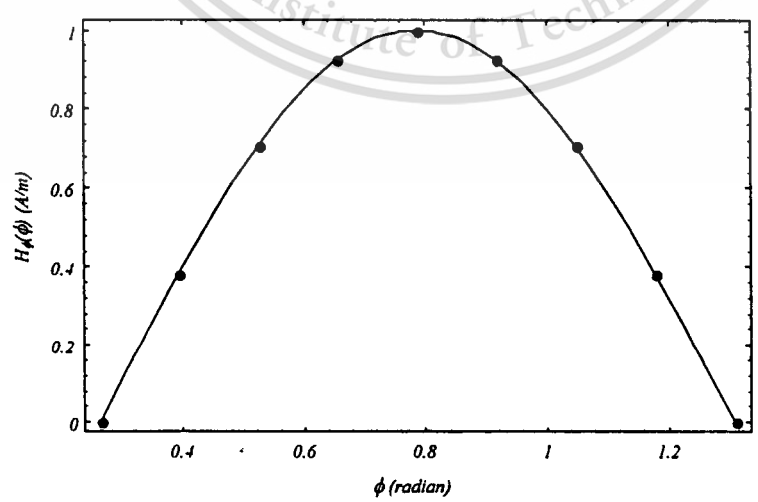

(c)

Fig. 4.7 Normalized H_ϕ : **(a)** in r-direction, **(b)** in θ-direction and **(c)** in ϕ-direction
• FD-TD solution — Analytical solution

4.3 Concentric Conducting Spherical Cavity Enclosed by a Conducting Conical Surface

In this section, the concentric conducting spherical cavity enclosed by a conducting conical surface, as shown in Fig.4.1b, is modeled by using the considered FD-TD algorithm. By means of the FD-TD algorithm, the solution region will be subdivided similar to that shown in Fig.4.8. The procedures of modeling the cavity are still the same except that the treatments of the singularity at the north pole must be considered. The singularity can be avoided by using the method discussed in the previous chapter ((3.9a) through (3.10c)).

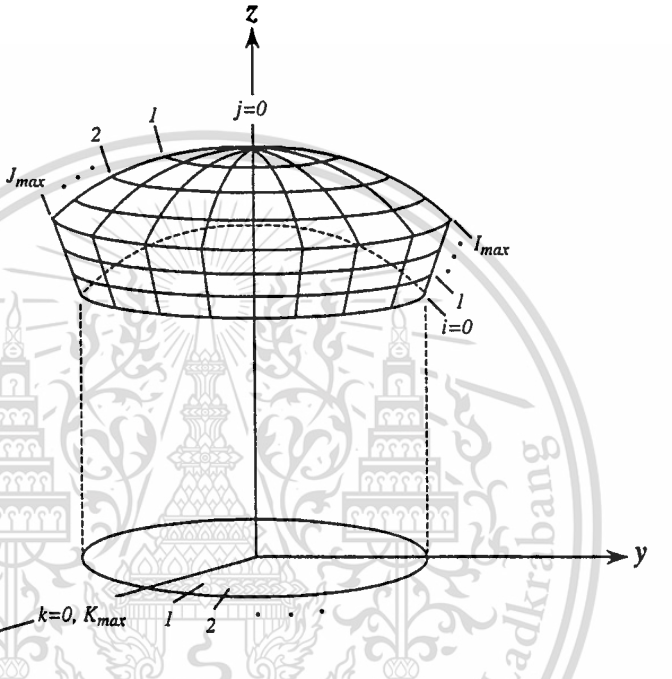

Fig.4.8 A subdivided concentric spherical cavity enclosed by a conical surface

Table 4.2 The first five solutions to (4.5b); TE_{35} and $\theta_1/\theta_2 = 1/5$

Solution number	θ_1 *(radian)*
1	*0.0000000*
2	*0.8187562*
3	*1.5707963*
4	*2.3228364*
5	*0.0000000*

Similar to the previous numerical example, the TE_{35} wave mode is selected to resonate in an air-filled concentric conducting cavity enclosed by a conducting conical surface. Starting with the analytical equation (4.5b), the first five solutions of θ_1' can be obtained as shown in Table 4.2. In radial direction, by using the same ratio R_a/R_b, the same set of solutions as shown Table 4.1 are obtained. For the ϕ-direction, the $sin(m\phi)$ function (even mode) is chosen. Consider the first practical solutions of Table 4.1 (for R_b) and Table 4.2, the dimensional parameters of the resonant cavity can be concluded as follows: $R_a = 0.2978075\ m$, $R_b = 1.4890377\ m$, $\theta_1 = 0.8187562\ radian$. Then, the calculated dimensional parameters together with (4.10a) through (4.10c) lead to the FD-TD space parameters as follows: $I_{max} = 6$, $J_{max} = 8$, $K_{max} = 15$, $\Delta r = 0.1985384\ m$, $\Delta\theta = 0.1023445\ radian$ and $\Delta\phi = 0.4188790\ radian$. Again, five sampling points per wavelength ($N = 5$) is chosen. Finally, from (3.17b), the time increment Δt can be estimated to be about 4×10^{-13} *seconds* (after backed off). The boundary conditions for the FD-TD field unknowns at the PEC surfaces of the cavity can be written as

$$E_r\Big|_{j=J_{max}} = 0, \tag{4.13a}$$

$$E_\theta\Big|_{i=0,I_{max}} = 0, \tag{4.13b}$$

$$E_\phi\Big|_{i=0,I_{max}\ or\ j=J_{max}} = 0, \tag{4.13c}$$

$$H_r\Big|_{i=0,I_{max}} = 0 \tag{4.13d}$$

$$H_\theta\Big|_{j=J_{max}} = 0. \tag{4.13e}$$

The source conditions similar to the previous discussion can be implemented by multiplying a function, $sin(2\pi mk)/K_{max}$, to the existing sine or ramped sine functions. For the multiplying function, m and k are the wave mode number and the index in ϕ-direction, respectively.

After about four periods of the applied sinusoidal wave, the mode patterns inside the segmented cavity, at $i = 4$, $j = 5$ and $k = 8$, are shown along with the analytical solutions in Fig.4.9 through Fig.4.13. From the figures, the FD-TD solutions are found very accurate when compared with the analytical results, and all errors are bounded within 5-10%. Similar to the previous numerical results, it is found that the results in r- and θ-direction are not as much accurate as in ϕ-direction. Also expected from the results, globally, the accuracy is poorer than those in the case of the segmented cavity. This additional expected behavior, for the case of the concentric spherical cavity enclosed by a conical surface, occurs due to the modeling errors (integral approximations near the north pole). As mentioned before, these modeling errors can be reduced by keeping the FD-TD volume cells as small as possible, or alternatively, studying well about the physical behaviors of all field components near the pole before approximating the integrands.

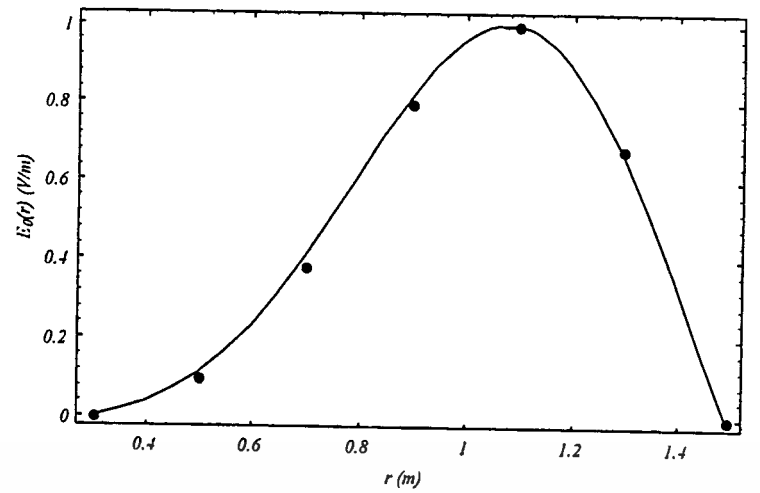

(a)

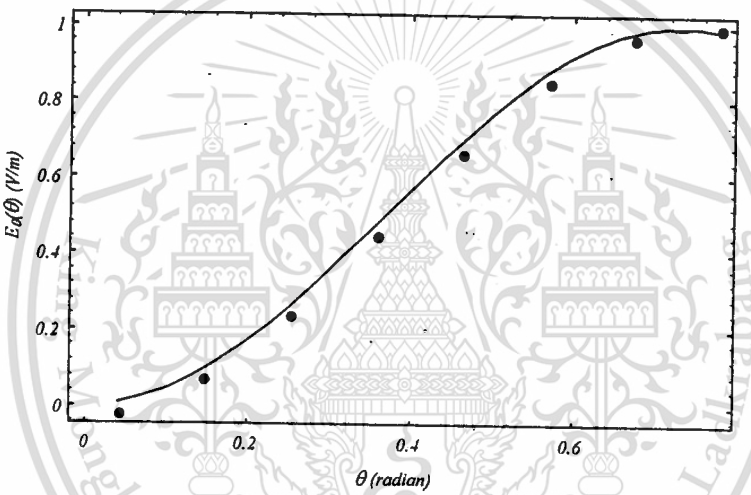

(b)

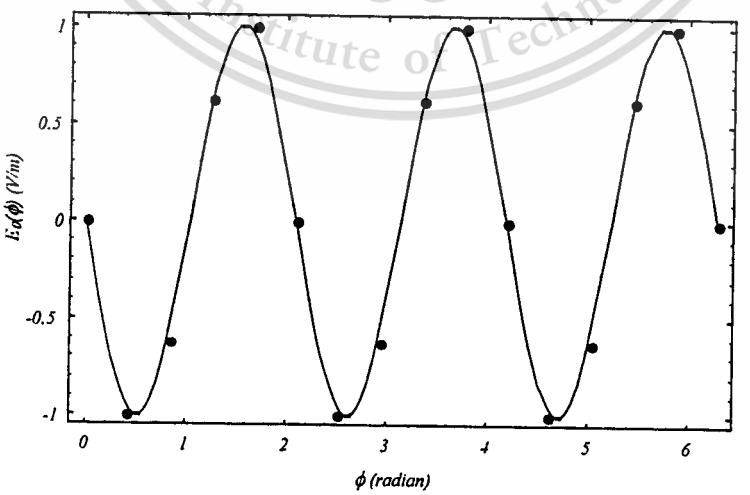

(c)

Fig. 4.9 Normalized E_θ : **(a)** in r-direction, **(b)** in θ-direction and **(c)** in ϕ-direction
• FD-TD solution — Analytical solution

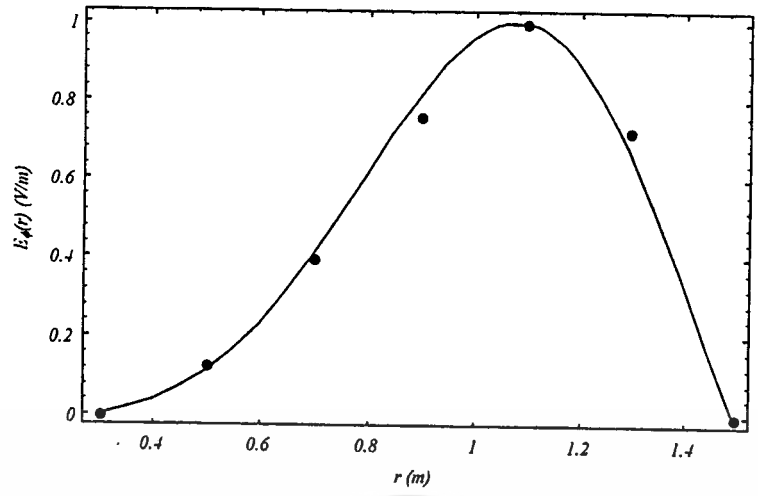

(a)

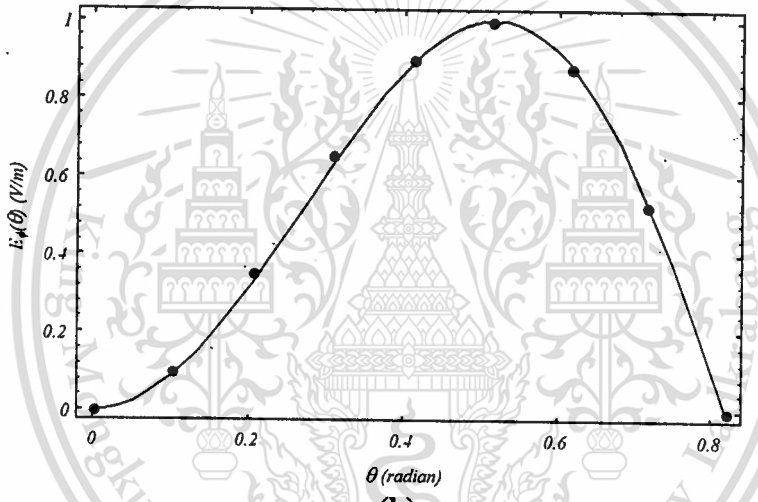

(b)

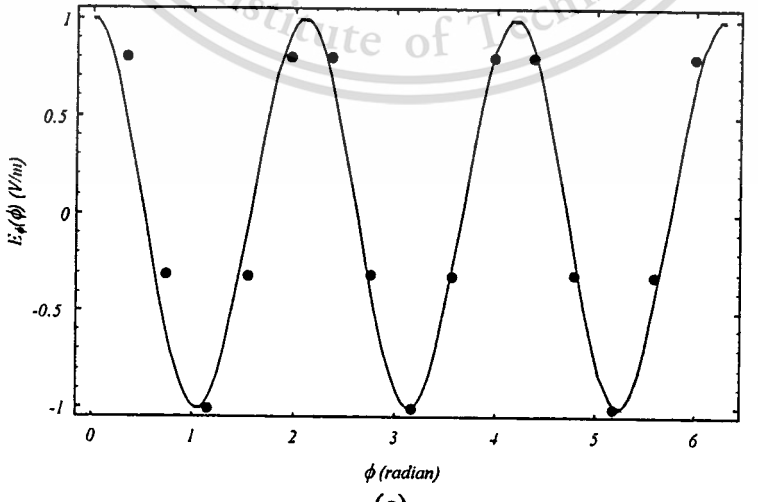

(c)

Fig. 4.10 Normalized E_ϕ : **(a)** in r-direction, **(b)** in θ-direction and **(c)** in ϕ-direction
• FD-TD solution — Analytical solution

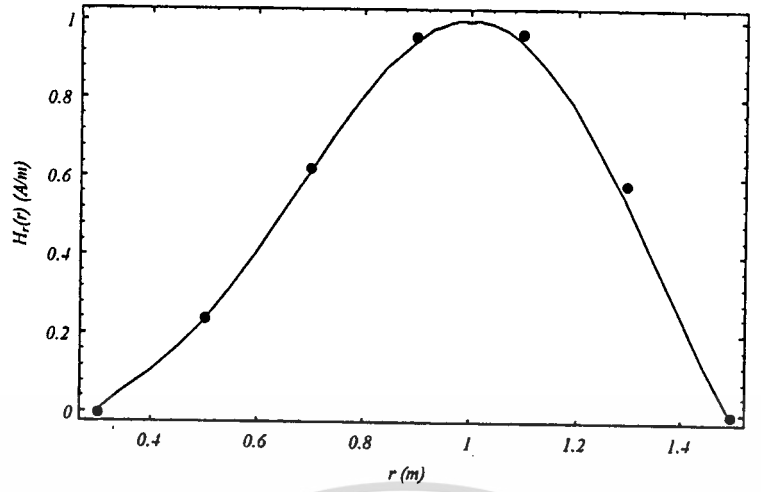

(a)

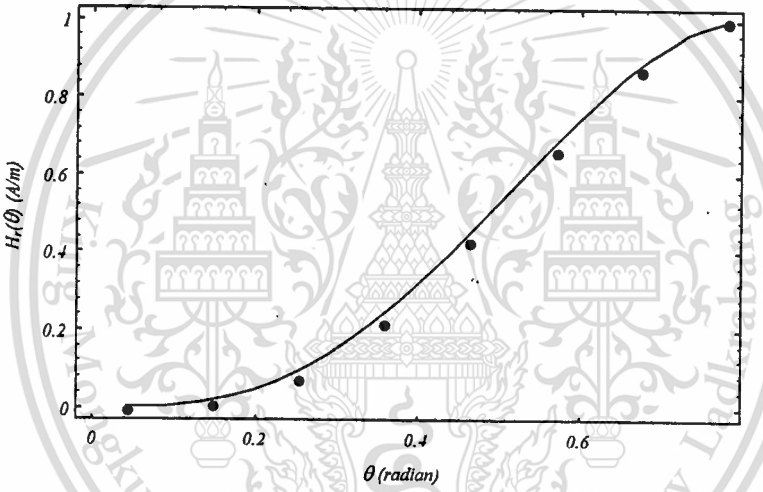

(b)

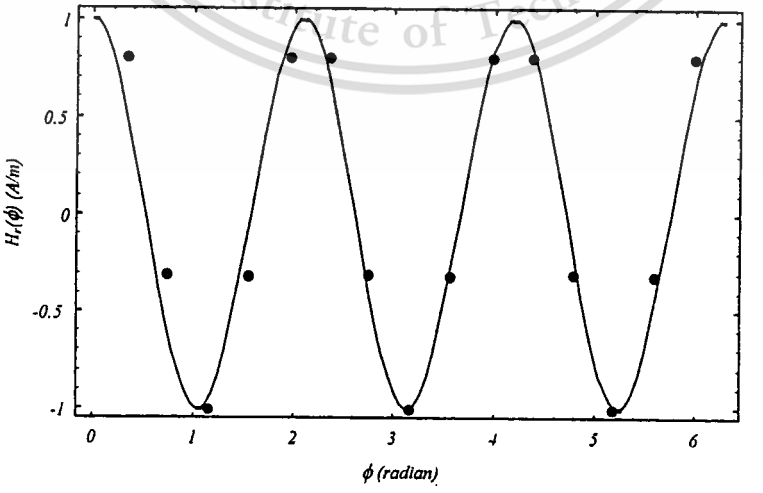

(c)

Fig. 4.11 Normalized H_r : **(a)** in r-direction, **(b)** in θ-direction and **(c)** in ϕ-direction
• FD-TD solution — Analytical solution

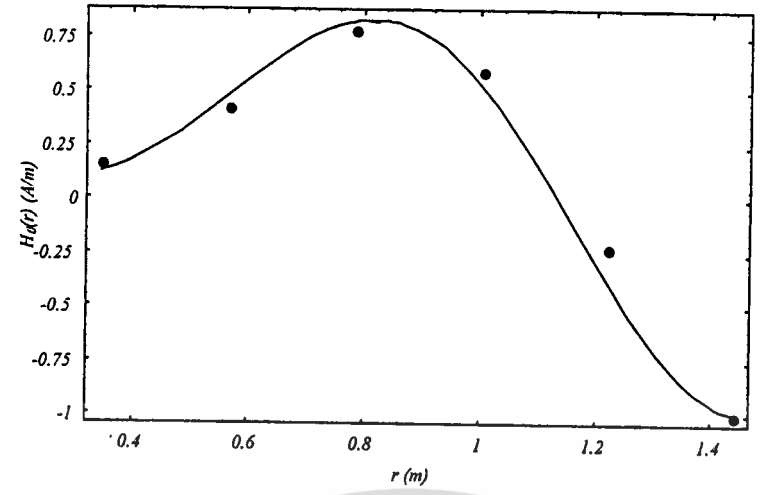

(a)

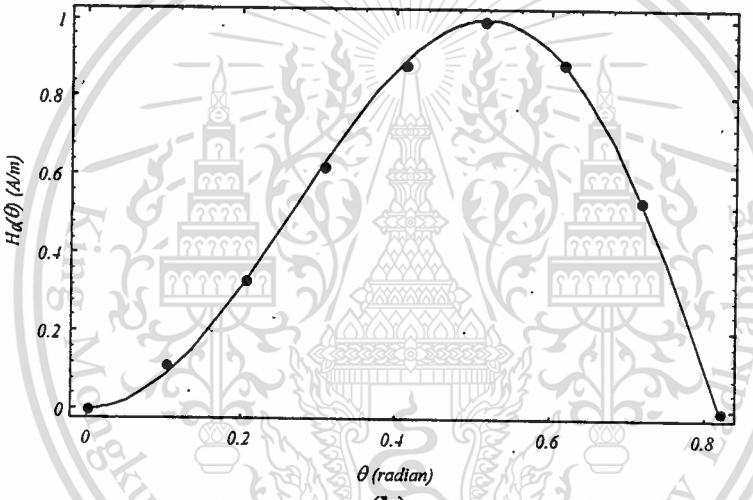

(b)

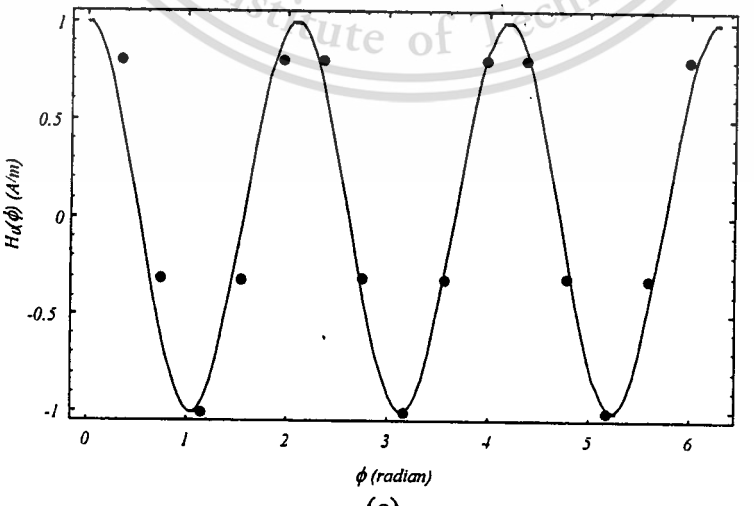

(c)

Fig. 4.12 Normalized H_θ : **(a)** in r-direction, **(b)** in θ-direction and **(c)** in ϕ-direction
• FD-TD solution — Analytical solution

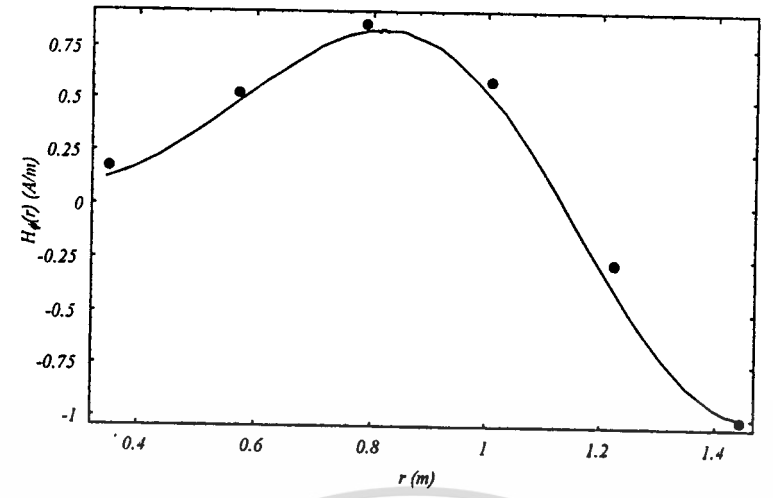

(a)

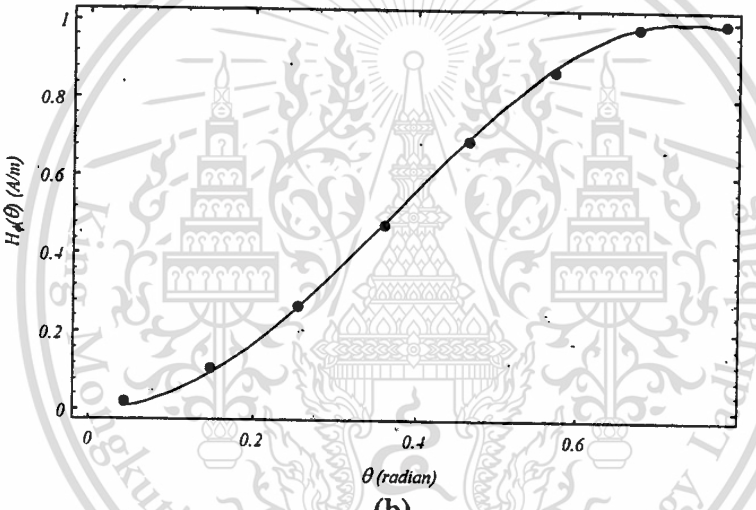

(b)

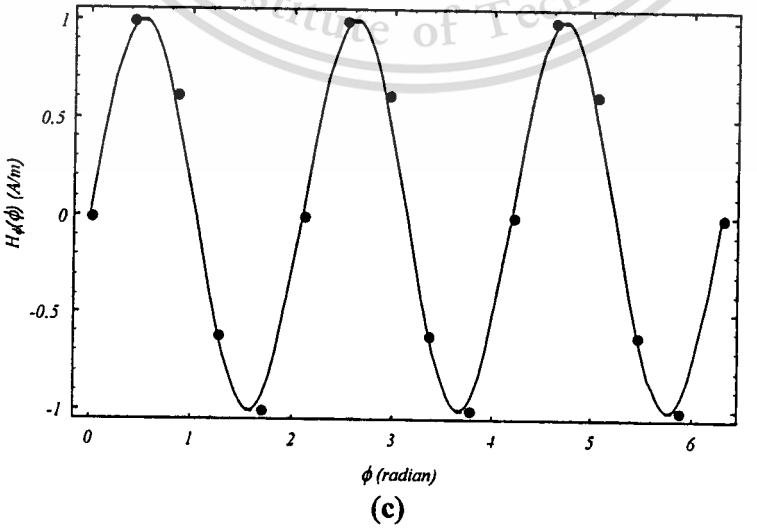

(c)

Fig. 4.13 Normalized H_ϕ : **(a)** in r-direction, **(b)** in θ-direction and **(c)** in ϕ-direction
• FD-TD solution — Analytical solution

4.4 Conducting Spherical Cavity

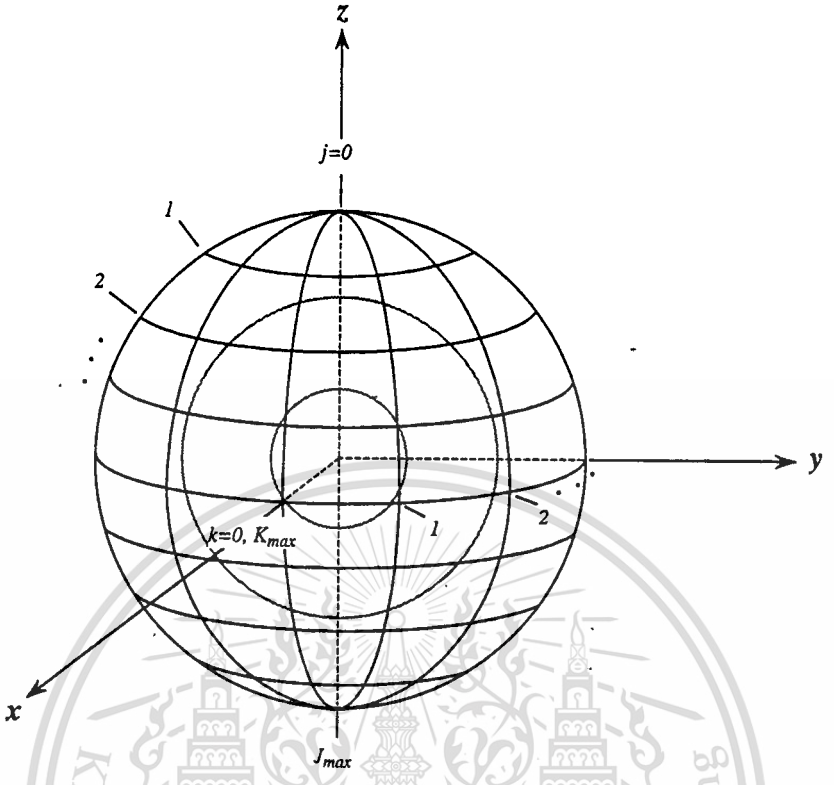

Fig. 4.14 A subdivided spherical cavity

As the last material to be considered here, the conducting spherical cavity, as shown in Fig.4.1(c), is to be analyzed by using the FD-TD algorithm in spherical coordinates. The solution region will be discretized as shown in Fig.4.14. The procedures of modeling the cavity are the same as the two previous examples except that the treatments of all the singularities, at the poles and the origin point, must be considered. The methods to avoid these singularities were explained in the section of singularity considerations of the previous chapter.

Consider a new wave mode, TE_{22}, resonating in an air-filled conducting spherical cavity. From the analytical equation (4.4b), the first five solutions of R_a can be obtained and shown in Table 4.3. In the ϕ-direction, again, the $sin(m\phi)$ function is selected. By choosing the first practical solution of Table 4.3 ($R_a = 0.9172830\ m$) and using $N = 10$, the FD-TD space parameters can be obtained as follows: $I_{max} = 10$, $J_{max} = 10$, $K_{max} = 10$, $\Delta r = 0.0917283\ m$, $\Delta\theta = 0.3141593$ *radian* and $\Delta\phi = 0.6283185$ *radian*. Finally, from (3.17b), the time increment Δt can be approximated to be about 2×10^{-13} *seconds* (after backed off). The boundary conditions for the FD-TD field unknowns at the PEC surfaces of the spherical cavity can be concluded as follows:

$$E_\theta\big|_{i=I_{max}} = 0, \tag{4.14a}$$

$$E_\phi\big|_{i=I_{max}} = 0, \tag{4.14b}$$

$$H_r\big|_{i=I_{max}} = 0, \tag{4.14c}$$

For source conditions, the same ones as discussed in the previous section can also be applied to this last numerical example.

Table 4.3 The first five solutions to (4.4b); TE_{22}

Solution number	R_a *(m)*
1	*0.0000000*
2	*0.9172830*
3	*1.4475160*
4	*1.96125670*
5	*2.4692258*

After about four periods of the applied sinusoidal wave, the mode patterns inside the segmented cavity, at $i = 6$, $j = 6$ and $k = 6$, are obtained and shown along with the analytical solutions in Fig.4.15 through Fig.4.19. From the results, it is evident that the FD-TD solutions almost fit to the analytical results. Globally, all errors are found less than 10%. In the similar manner as the previous numerical examples, the results in ϕ-direction are more accurate than in r- and θ-direction. In addition, it should be noted that even ten sampling points per wavelength are used, the accuracy of the results is not much better than those of the two previous cavity models. This maybe because the spherical cavity possesses all singularities within the solution region, at the two poles and at the origin. However, some means to achieve more accurate results, as mentioned in the previous sections, can be utilized.

4.5 Conclusions

The formulated FD-TD algorithm is applied to analyze the electromagnetic fields inside three configurations of conducting cavities: a segmented cavity, a concentric spherical cavity enclosed by a conical surface and a spherical cavity. The analysis is in source-free region and obtained the mode patterns within the cavities. The simulation of source-free region is achieved by simply adding small amount of sinusoidal waves to some proper field components, for the whole region of cavities. Here, the E_θ and H_ϕ are expected as the proper field components, because they are exactly terminated at $k = 0$ and K_{max} in the solution region. In addition to the source condition, the alternative ramped sine function is also introduced.

Three general steps in modeling a cavity by using the FD-TD method can be summarized as follows:

(1) Use analytical solutions to find the dimensions of the resonant cavity of the desired mode and dimensional configurations.
(2) Compute FD-TD parameters using proper resolutions that based on wavelength.
(3) Match boundary conditions for all FD-TD field unknowns referring to the configurations of the designed cavity, including considerations of singularities and treatments.

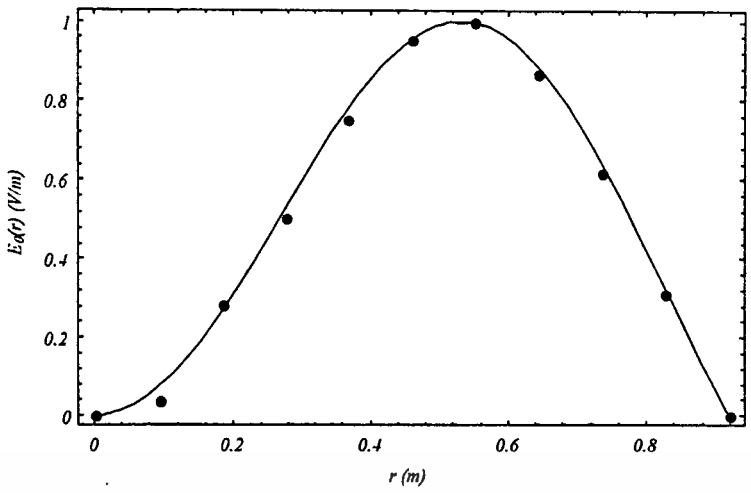

(a)

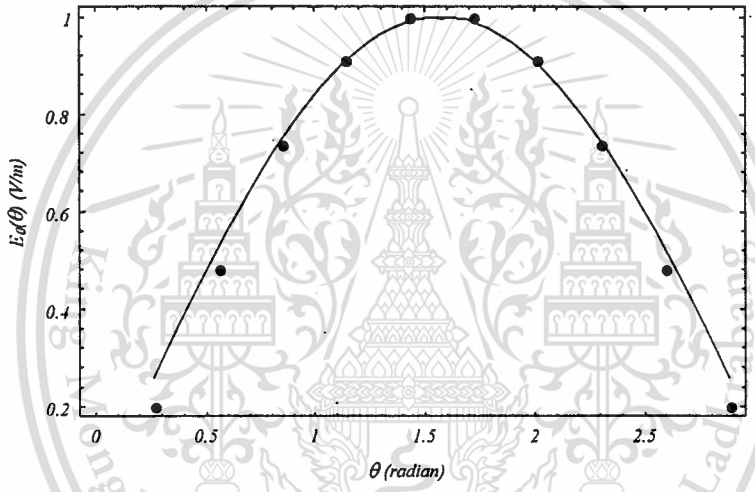

(b)

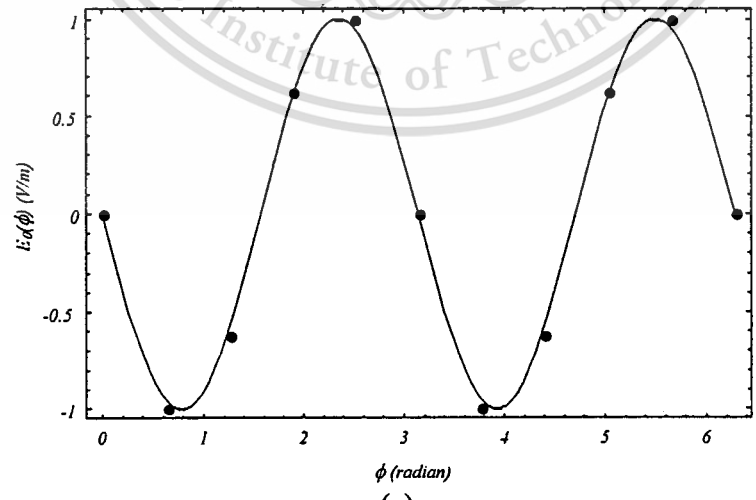

(c)

Fig. 4.15 Normalized E_θ : **(a)** in r-direction, **(b)** in θ-direction and **(c)** in ϕ-direction
• FD-TD solution — Analytical solution

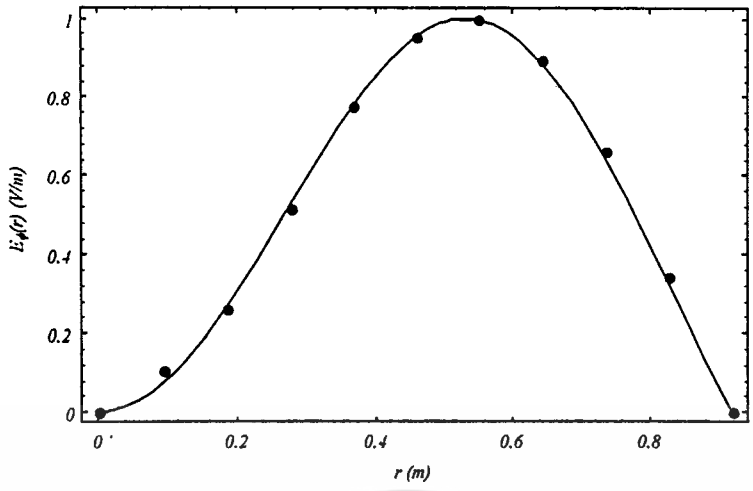

(a)

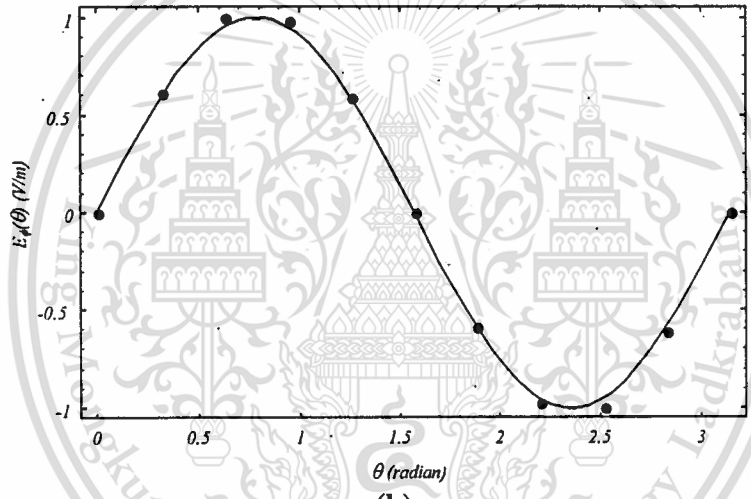

(b)

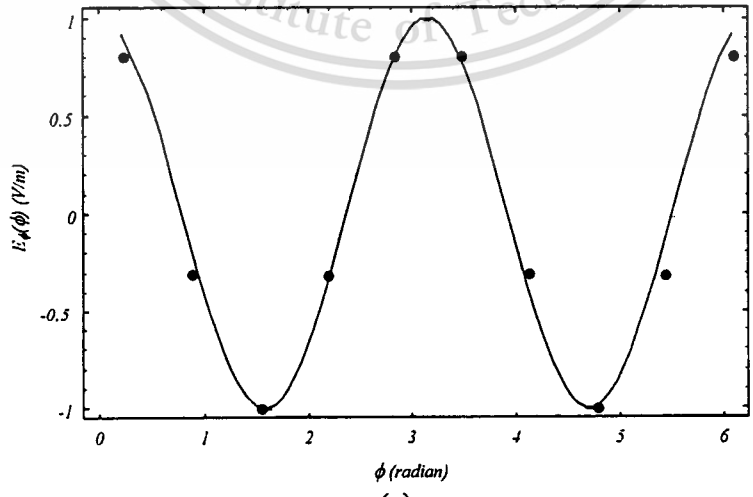

(c)

Fig. 4.16 Normalized E_ϕ : **(a)** in r-direction, **(b)** in θ-direction and **(c)** in ϕ-direction
• FD-TD solution — Analytical solution

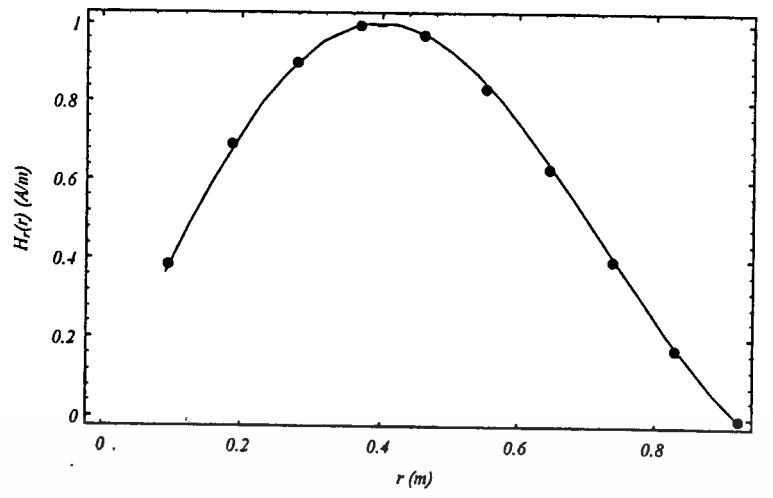

(a)

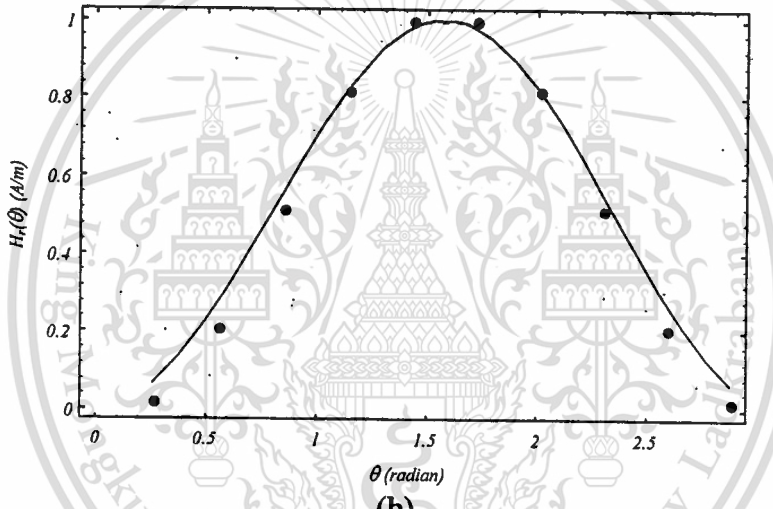

(b)

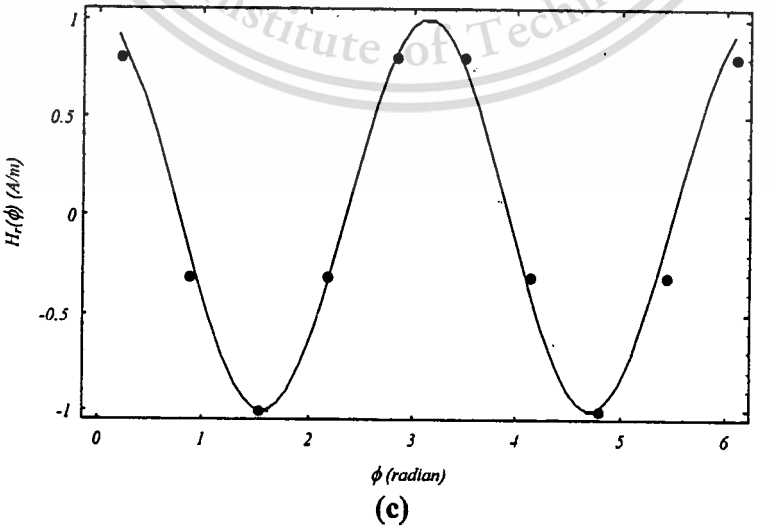

(c)

Fig. 4.17 Normalized H_r : **(a)** in r-direction, **(b)** in θ-direction and **(c)** in ϕ-direction
• FD-TD solution — Analytical solution

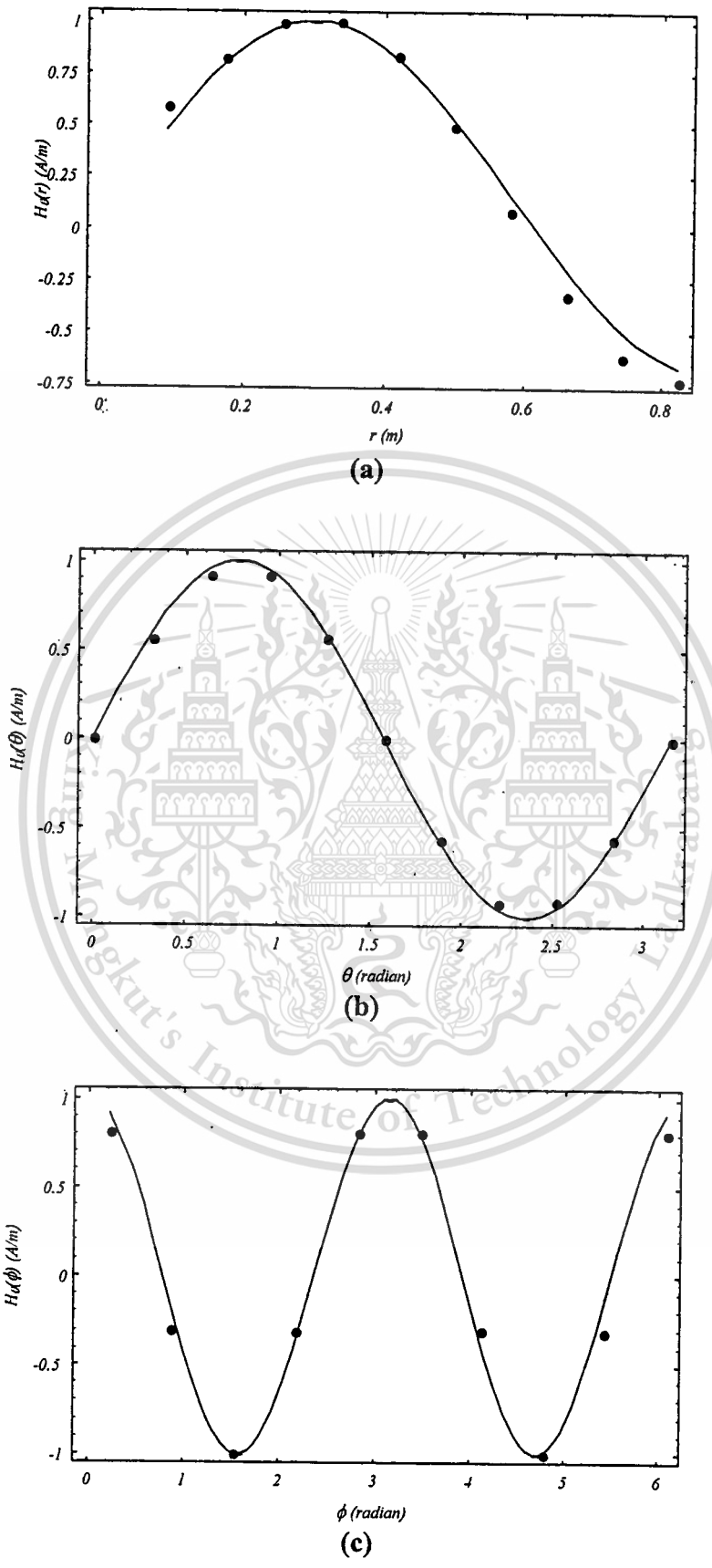

Fig. 4.18 Normalized H_θ : **(a)** in r-direction, **(b)** in θ-direction and **(c)** in ϕ-direction
• FD-TD solution — Analytical solution

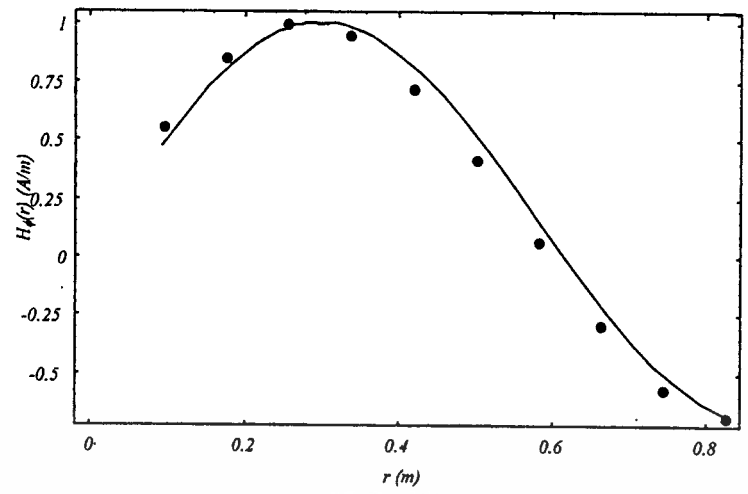

(a)

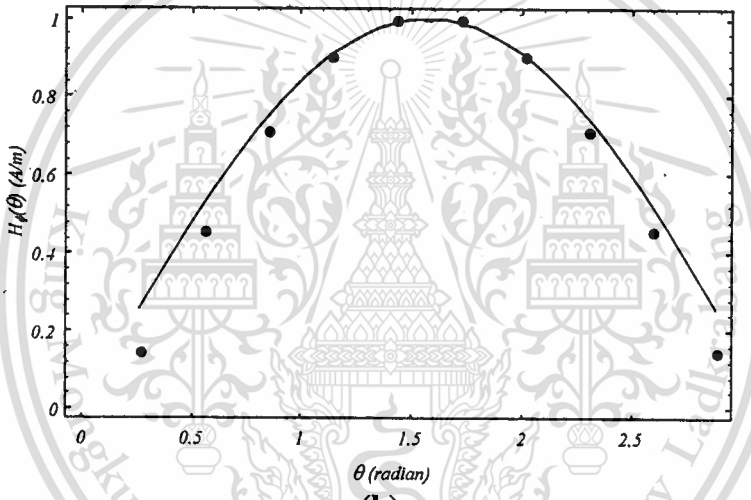

(b)

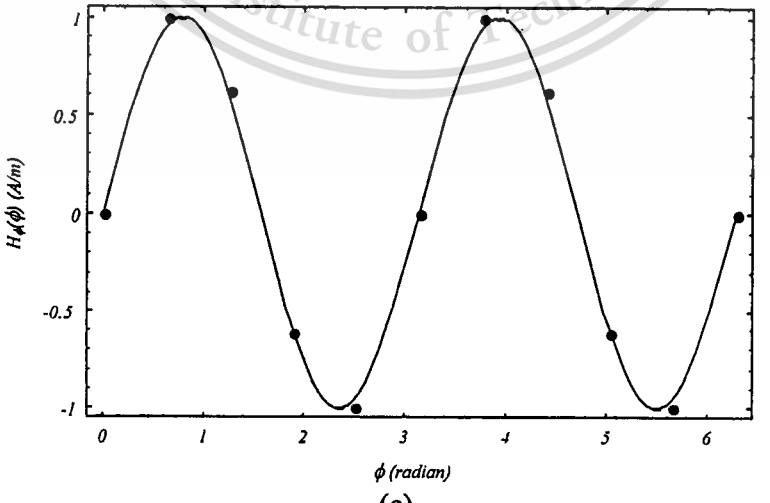

(c)

Fig. 4.19 Normalized H_ϕ : **(a)** in r-direction, **(b)** in θ-direction and **(c)** in ϕ-direction
• FD-TD solution — Analytical solution

From the three cavity models, the segmented cavity is found to be the easiest one for modeling by the FD-TD method, because there is no any singularity in the solution region. This also yields the most accurate numerical results when compared with the left two cavity models. However, because of its *hexahedral* shape, the boundary conditions must be applied to all of its six faces (and all six FD-TD field components). In case of the conducting concentric spherical cavity enclosed by a conducting conical surface, the model is found more difficult because there is a singularity at the north pole. Although there are some means to avoid this singularity as mentioned in the previous chapter, the accuracy of the results is still degraded by the integral approximations (modeling errors). The advantage of this cavity model over the segmented cavity is that there are only three PEC surfaces (i.e. $r = R_a$ and R_b, and $\theta = \theta_1$) at which need to be matched boundary conditions. For the spherical cavity, it is considered as the most difficult model to be analyzed by the FD-TD method. This is stated because this cavity configuration contains all singularities. Especially, the singularities at the two poles and at the origin cause severe errors due to their non-linearity, including modeling errors from all integral approximations. From the numerical results, the accuracy of the spherical cavity looked the same as those of the previous cavity model, even the number of sampling points per wavelength is doubled ($N = 10$). However, the spherical cavity has one advantage over the two previous cavity models. There is only one PEC surface at $r = R_a$ at which boundary conditions are applied. As mentioned before, errors due to non-linearity and integral approximations can be reduced by dividing finer volume cells, or alternatively, implementing higher-order algorithms.

Chapter 5

Probe Modeling, Slot Modeling and Near-to-Far Field Transformations

In the previous chapters, the discussions are mostly based on ideal theoretical models. In practical situations, these models can not be directly applied to obtain results that comparable with experimental ones. For example, the probe are to be used as a source excitation in place of the ideal source conditions as illustrated in the previous chapter. To get more reasonable results, somehow, a mathematical model at a feeding point should be constructed and included in the analysis. Thus, this chapter involves preparations of FD-TD models for an antenna feed by a probe and radiating through a slot. These models together with the knowledge of cavity modeling from the previous chapter will be integrated to construct an antenna having slotted hemispherical cavity, in the next chapter. The FD-TD probe and slot models are deviced and classified into two categories: detailed (or fine) models and approximate models. As the last discussion, some convenient techniques to achieve far-field responses or radiation patterns, are introduced; without extending a computational space to the far-field region. Two well-known schemes of zone transformations are reviewed here: frequency-domain and time-domain near-to-far field transformations.

5.1 Detailed Models

Detailed modeling of any FD-TD problems simply means that using *very high resolutions* of volume cells to include some small objects within problem spaces. There is no strict definition for the very high resolution; however, in many practical problems *40 cells/*λ_o is usually taken as the lower limit, while *10* and *20 cells/*λ_o are considered as *normal resolutions*. A scheme in modeling an object is quite simple by allocating many small volume cells to conform to the shape of the object of interest. This modeling style is expected to yield accurate results, and often chosen when comparisons of numerical results with other methods are required. Although this style of modeling is found easy and accurate, excessive computational costs are required for some problem configurations. In the following two sub-sections, the simple detailed models of probe and slot are considered. Additionally, a special method *sub-gridding algorithm* is introduced at the end of the section, which may help to relief the cost constraints.

5.1.1 Probe model

Simple as introduced above, a probe model can be achieved by changing some air-filled volume cells to represent a high-conductivity volume cells, for the entire body of the probe model. The discretized cross-section of the probe model is typically designed and shown in Fig.5.1(a). From the figure, the cross-section of the probe model is bounded within a *5*×*5*-cell region. Thus the approximate resolution for problems that including this probe model should be at least about *5* times the normal case, which is about *50 cells/*λ_o. It is seen that the discretized probe model is not conforming well to the physical circular cross-section that some modeling errors due to discretization are expected. However, the errors can be reduced if volume cell sizes are very small, comparing with the wavelength. Fig.5.1(b) shows the 3-D view of the probe model attaching to the feeding point, which is a

transmission line's aperture. The feeding can be done by distributing a time-dependent voltage to the FD-TD volume cells posing near the aperture.

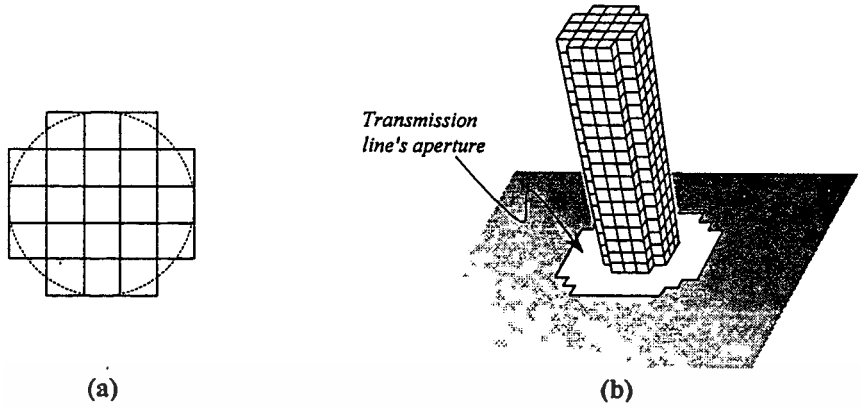

Fig. 5.1 **(a)** Cross-section of the discretized probe model
(b) 3-D view of the model attaching the transmission line's aperture

In addition to the probe model above, it is found that the model may cause instability if it is constructed from only one FD-TD volume cell and the boundary conditions at the air-conductor interfaces are not posed well.

5.1.2 Slot model

In the opposite sense of the probe model, the slot model can be constructed by changing some high-conductivity volume cells on a discretized conducting screen to be air-filled volume cells to represent a slot gap. A typical discretized long slot model is shown in Fig.5.2(a). From the figure, the slot width is conformed within *5* FD-TD volume cells. This leads to the resolution about *50 cells/*λ_o for problems including this slot model. Unlike the probe model, the slot model has no problem about fitting volume cells with the slot edges, except that the inclined slot is to be implemented. The magnification of the model is shown in Fig.5.2(b) to view positions of the FD-TD field components, H_r, E_θ and E_ϕ, in the slot gap. Additionally, if the conducting screen is assumed to be a perfect conductor, the field components E_θ and E_ϕ at the slot edges should be considered to be zero for all time steps of FD-TD simulations.

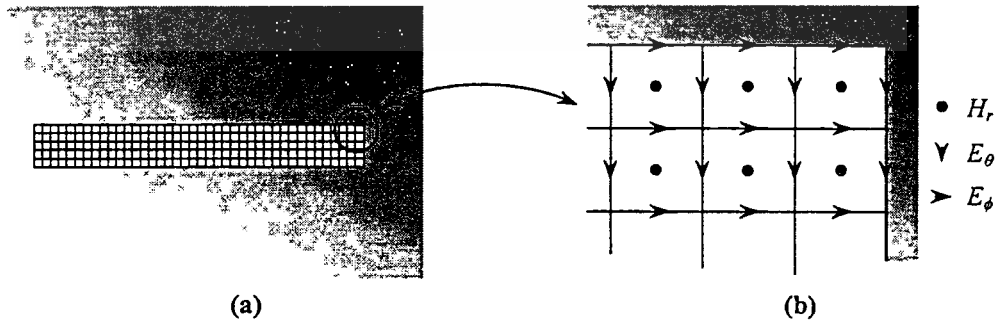

Fig. 5.2 **(a)** Discretization of slot model
(b) Magnification of the model

As mentioned before at the beginning of the chapter, the computational costs grow excessively when the resolution of a problem is increased. Even in some cases, the memory resources are adequate, but unfortunately, computation time required for

processing the FD-TD simulation is very long (e.g. in spherical coordinates). This is stated because the reduction of FD-TD cell sizes also decreases size of the time step, which required for stability condition. These cost constraints can be relieved by using an alternative scheme called sub-gridding algorithm. The algorithm is originally proposed for solving problems in rectangular coordinates; however, it can be useful for spherical spaces. There are two types of algorithms considered in [20], but only the simpler and more stable one will be briefly reviewed here, which is the subgridding algorithm by factor of two.

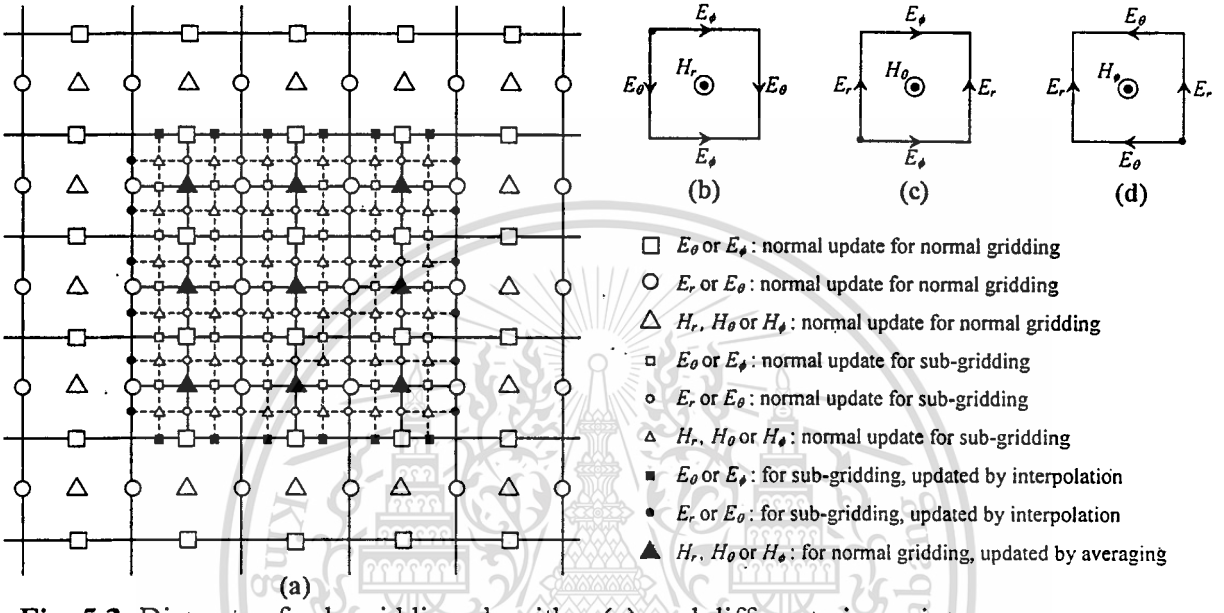

Fig. 5.3 Diagram of sub-gridding algorithm (**a**), and different viewpoints on a FD-TD volume cell: (**b**) top view, (**c**) front view and (**d**) side-view (from right-hand side)

The diagram of the sub-gridding method, in case of the subdivision factor equals *2*, is shown in Fig.5.3(a). In the figure, there are two domains: sub-gridding (small symbolic shapes) and normal gridding (big symbolic shapes). All field components within these domains are updated independently by using normal FD-TD equations, except for the special ones that positioned at the black symbolic shapes are updated by interpolating or averaging. The details of special updating are concluded as follows:

(1) All field components at the big black triangles are updated by averaging their four neighboring small white triangles.

(2) All field components at the boundary of the sub-gridding domain (small black symbolic shapes) are updated by doing spatial and time interpolations. The small black circles are interpolated from their neighboring big white circles. The similar procedure is done for the small black rectangles.

In addition to the FD-TD updating, if the time step (Δt) is used in the normal gridding domain, half of the time step ($\Delta t/2$) must be used in the sub-gridding domain. To this end, the sub-gridding domain can be applied to volume cells near or in the probe or slot model, and elsewhere the normal domain is used. Thus only about half of the memory requirement of the typical resolution above (50 *cells*$/\lambda_o$) is required, which is approximately 25 *cells*$/\lambda_o$.

5.2 Approximate Models

When very small objects are being embedded in the FD-TD solution regions, in case of the detailed models are not preferred, approximate models are often considered as alternate means. The schemes in modeling mostly involves finding physical assumptions (or mathematical models) to describe behaviors of fields near or inside structures of interest. The approximate models can greatly reduce the cost constraints, because the models can be implemented in normal-resolution FD-TD spaces. However, it is much more difficult to achieve the models, and risk of severe modeling errors due to wrong physical assumptions.

5.2.1 Probe model

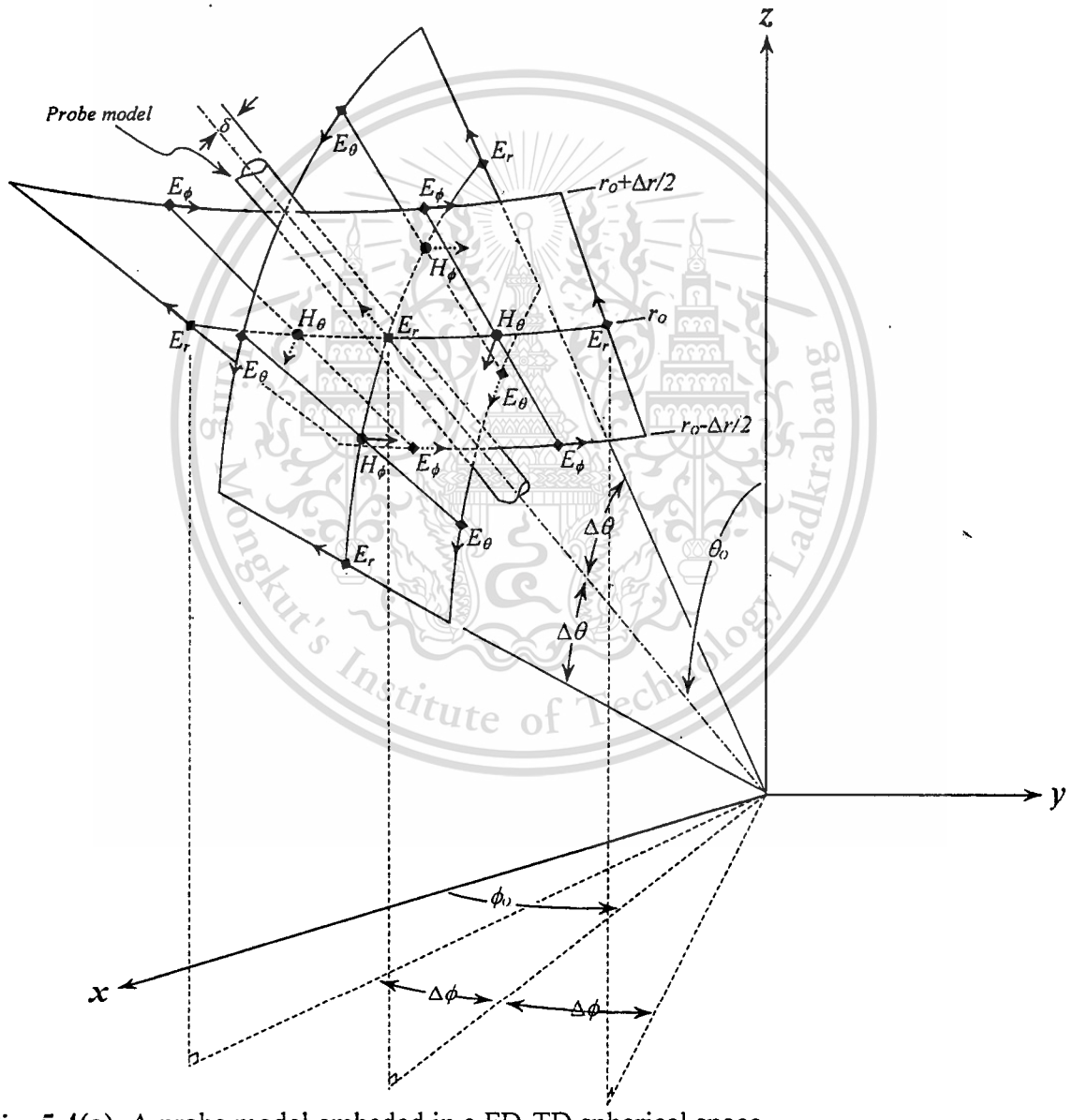

Fig. 5.4(a) A probe model embeded in a FD-TD spherical space

A typical circular cross-section probe model is embeded in a FD-TD space as shown in Fig.5.4(a). The figure shows all neighboring field components, E_r, E_θ . E_ϕ . H_θ and H_ϕ , of one segment of the probe model, which are to be updated by special

FD-TD equations obtained from near-field physical aussumptions. The near-field physical assumptions of the thin wire model are first asserted in [3], which are made in rectangular coordinates. Then, Faraday's law is applied to get the special updating equations for the magnetic fields near the model. The model is used for many typical applications [4, 29-30], which yields good results. Here, for generality, the assumptions are rearranged and to be implemented in spherical coordinates. The behaviors of all fields near the probe model are postulated as follows:

(1) All field components vary as $1/r'$, where r' is the shortest distance measured from the center of the probe model to the point where each of the field components is considered.

(2) All field components on each of integrating surfaces and paths, measured along the probe length can be approximated by linear functions.

To make the derivation easy, Fig.5.4(a) is redrawn into two figures corresponding to the constant surfaces, ϕ_o and θ_o.

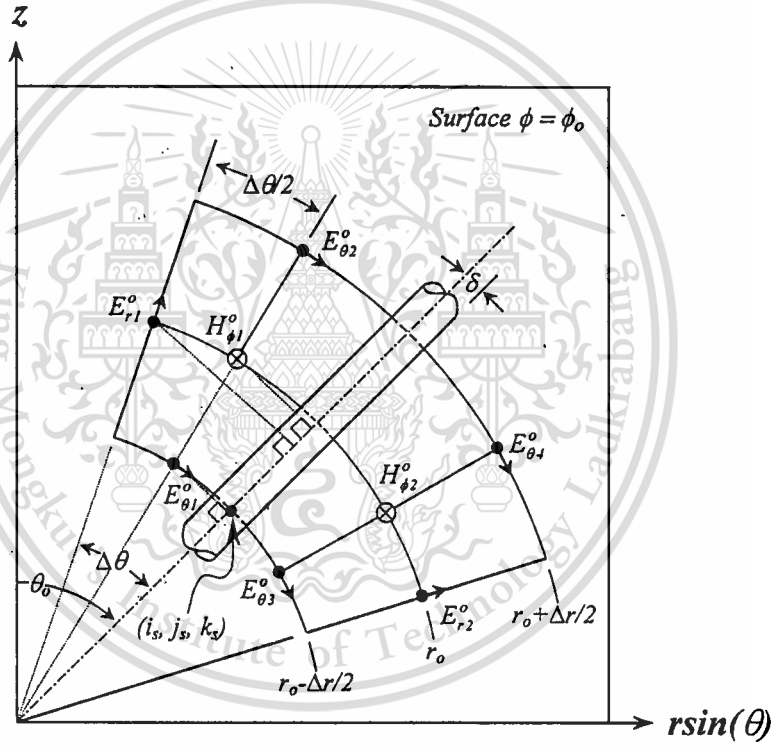

Fig. 5.4(b) The probe model and the neighboring field components viewed on the surface $\phi = \phi_o$.

Fig.5.4(b) shows one cell of the probe model and two integrating surfaces containing eight FD-TD field components, all are viewed on the constant surface $\phi = \phi_o$. From the figure and the near-field assumptions, the field components E_{r1}, E_{r2}, $E_{\theta 1}$, $E_{\theta 2}$, $E_{\theta 3}$, $E_{\theta 4}$, $H_{\phi 1}$ and $H_{\phi 2}$, can be written as function of r and θ as follows:

$$E_{r1}(r,\theta_o-\Delta\theta,\phi_o)=E^o_{r1}\left(\frac{r_o}{r}\right)\{1+c_{er1}\cos(\Delta\theta)[r-r_o]\}, \tag{5.1a}$$

$$E_{r2}(r,\theta_o+\Delta\theta,\phi_o)=E^o_{r2}\left(\frac{r_o}{r}\right)\{1+c_{er2}\cos(\Delta\theta)[r-r_o]\}, \tag{5.1b}$$

$$E_{\theta 1}(r_o - \Delta r/2, \theta, \phi_o) = E^o_{\theta 1} \frac{\sin(\Delta\theta/2)}{\sin(\theta_o - \theta)} \left\{ 1 + c_{e\theta 1} \left(r_o - \frac{\Delta r}{2} \right) \left[\cos(\theta_o - \theta) - \cos\left(\frac{\Delta\theta}{2} \right) \right] \right\}, \tag{5.1c}$$

$$E_{\theta 2}(r_o + \Delta r/2, \theta, \phi_o) = E^o_{\theta 2} \frac{\sin(\Delta\theta/2)}{\sin(\theta_o - \theta)} \left\{ 1 + c_{e\theta 2} \left(r_o + \frac{\Delta r}{2} \right) \left[\cos(\theta_o - \theta) - \cos\left(\frac{\Delta\theta}{2} \right) \right] \right\}, \tag{5.1d}$$

$$E_{\theta 3}(r_o - \Delta r/2, \theta, \phi_o) = E^o_{\theta 3} \frac{\sin(\Delta\theta/2)}{\sin(\theta - \theta_o)} \left\{ 1 + c_{e\theta 3} \left(r_o - \frac{\Delta r}{2} \right) \left[\cos(\theta - \theta_o) - \cos\left(\frac{\Delta\theta}{2} \right) \right] \right\}, \tag{5.1e}$$

$$E_{\theta 4}(r_o + \Delta r/2, \theta, \phi_o) = E^o_{\theta 4} \frac{\sin(\Delta\theta/2)}{\sin(\theta - \theta_o)} \left\{ 1 + c_{e\theta 4} \left(r_o + \frac{\Delta r}{2} \right) \left[\cos(\theta - \theta_o) - \cos\left(\frac{\Delta\theta}{2} \right) \right] \right\}, \tag{5.1f}$$

$$H_{\phi 1}(r, \theta, \phi_o) = H^o_{\phi 1} \frac{r_o \sin(\Delta\theta/2)}{r \sin(\theta_o - \theta)} \left\{ 1 + c_{h\phi 1} \left[r \cos(\theta_o - \theta) - r_o \cos(\Delta\theta/2) \right] \right\}, \tag{5.1g}$$

$$H_{\phi 2}(r, \theta, \phi_o) = H^o_{\phi 2} \frac{r_o \sin(\Delta\theta/2)}{r \sin(\theta - \theta_o)} \left\{ 1 + c_{h\phi 2} \left[r \cos(\theta - \theta_o) - r_o \cos(\Delta\theta/2) \right] \right\}. \tag{5.1h}$$

In the above equations, the constants c_{er1}, c_{er2}, $c_{e\theta 1}$, $c_{e\theta 2}$, $c_{e\theta 3}$, $c_{e\theta 4}$, $c_{h\phi 1}$ and $c_{h\phi 2}$, are slopes of the linear functions (in the brackets, {}), which are functions of time. By substituting (5.1a), (5.1c), (5.1d) and (5.1g) into Faraday's law,

$$\mu \frac{\partial}{\partial t} \oiint_S \bar{H} \cdot d\bar{S} = -\oint_C \bar{E} \cdot d\bar{l}, \tag{5.2}$$

the approximate integral equation for updating the $H_{\phi 1}$ field component can be written as

$$\mu \frac{\partial}{\partial t} \left(H^o_{\phi 1} \right) \oiint_S \tilde{H}_{\phi 1} dS \approx -E^o_{r1} \int \tilde{E}_{r1} dl + E^o_{\theta 1} \int \tilde{E}_{\theta 1} dl - E^o_{\theta 2} \int \tilde{E}_{\theta 2} dl, \tag{5.3a}$$

where

$$\left.\begin{aligned}
\oiint_S \tilde{H}_{\phi 1}\,dS &= \frac{1}{H^o_{\phi 1}} \int_{r_o-\Delta r/2}^{r_o+\Delta r/2} \int_{\theta_o-\Delta\theta}^{\theta_o-\alpha} H_{\phi 1}\, r\, d\theta\, dr \\
\int \tilde{E}_{r1}\,dl &= \frac{1}{E^o_{r1}} \int_{r_o-\Delta r/2}^{r_o+\Delta r/2} E_{r1}\,dr \\
\int \tilde{E}_{\theta 1}\,dl &= \frac{r_o-\Delta r/2}{E^o_{\theta 1}} \int_{\theta_o-\Delta\theta}^{\theta_o-\alpha_1} E_{\theta 1}\,d\theta \\
\int \tilde{E}_{\theta 2}\,dl &= \frac{r_o+\Delta r/2}{E^o_{\theta 2}} \int_{\theta_o-\Delta\theta}^{\theta_o-\alpha_2} E_{\theta 2}\,d\theta
\end{aligned}\right\}. \qquad (5.3b)$$

In (5.3b), the parameters α, α_1 and α_2, are defined as follows:

$$\alpha = \sin^{-1}\left(\frac{\delta}{r}\right), \quad \alpha_1 = \sin^{-1}\left(\frac{\delta}{(r_o-\Delta r/2)}\right), \quad \alpha_2 = \sin^{-1}\left(\frac{\delta}{(r_o+\Delta r/2)}\right). \qquad (5.3c)$$

By applying the central time-derivative formula to approximate (5.3a), rewriting all field components in forms of FD-TD notations (i.e. all superscripts (^{o}) and numbering subscripts can be omitted), the recursive formula for updating the $H_{\phi 1}$ field component near the probe model is found to be

$$H_\phi(i_s, j_s-1, k_s)^{n+1} = H_\phi(i_s, j_s-1, k_s)^n + \frac{\Delta t}{\mu \oiint_S \tilde{H}_{\phi 1}\,dS} \times$$

$$\left\{ \begin{aligned}
&-\left[r_o\left(1 - r_o c_{er1}\cos(\Delta\theta)\right) ln\left(\frac{r_o+\Delta r/2}{r_o-\Delta r/2}\right) + r_o c_{er1}\Delta r\cos(\Delta\theta)\right] E_r(i_s, j_s-1, k_s)^{n+1/2} \\
&+\sin\left(\frac{\Delta\theta}{2}\right)\left\{\left[\left(r_o-\frac{\Delta r}{2}\right)\left(1 - c_{e\theta 1}\left(r_o-\frac{\Delta r}{2}\right)\cos\left(\frac{\Delta\theta}{2}\right)\right) ln\left(\frac{\tan(\Delta\theta/2)}{\tan(\alpha_1/2)}\right)\right.\right. \\
&\qquad \left.\left. + c_{e\theta 1}\left(r_o-\frac{\Delta r}{2}\right)^2 ln\left(\frac{\sin(\Delta\theta)}{\sin(\alpha_1)}\right)\right]\right\} E_\theta(i_s, j_s-1, k_s)^{n+1/2} \\
&-\left[\left(r_o+\frac{\Delta r}{2}\right)\left(1 - c_{e\theta 2}\left(r_o+\frac{\Delta r}{2}\right)\cos\left(\frac{\Delta\theta}{2}\right)\right) ln\left(\frac{\tan(\Delta\theta/2)}{\tan(\alpha_2/2)}\right)\right. \\
&\qquad \left. + c_{e\theta 2}\left(r_o+\frac{\Delta r}{2}\right)^2 ln\left(\frac{\sin(\Delta\theta)}{\sin(\alpha_2)}\right)\right] E_\theta(i_s+1, j_s-1, k_s)^{n+1/2}
\end{aligned} \right\} \qquad (5.4a)$$

Similarly, by using (5.1b), (5.1e), (5.1f) and (5.1h) together with Faraday's law, the recurrence formula for updating the $H_{\phi 2}$ field component near the probe model is obtained as

$$H_\phi(i_s,j_s,k_s)^{n+1} = H_\phi(i_s,j_s,k_s)^n + \frac{\Delta t}{\mu \oiint_S \tilde{H}_{\phi 1} dS} \times$$

$$\left\{ \left[r_o(1 - r_o c_{er2}\cos(\Delta\theta)) ln\left(\frac{r_o + \Delta r/2}{r_o - \Delta r/2}\right) + r_o c_{er2} \Delta r \cos(\Delta\theta) \right] E_r(i_s, j_s + 1, k_s)^{n+1/2} \right.$$

$$+ \sin\left(\frac{\Delta\theta}{2}\right) \left\{ \left[\left(r_o - \frac{\Delta r}{2}\right)\left(1 - c_{e\theta 3}\left(r_o - \frac{\Delta r}{2}\right)\cos\left(\frac{\Delta\theta}{2}\right)\right) ln\left(\frac{\tan(\Delta\theta/2)}{\tan(\alpha_1/2)}\right) \right.\right.$$

$$\left.\left. + c_{e\theta 3}\left(r_o - \frac{\Delta r}{2}\right)^2 ln\left(\frac{\sin(\Delta\theta)}{\sin(\alpha_1)}\right) \right] E_\theta(i_s, j_s, k_s)^{n+1/2} \right\}$$

$$\left. - \left[\left(r_o + \frac{\Delta r}{2}\right)\left(1 - c_{e\theta 4}\left(r_o + \frac{\Delta r}{2}\right)\cos\left(\frac{\Delta\theta}{2}\right)\right) ln\left(\frac{\tan(\Delta\theta/2)}{\tan(\alpha_2/2)}\right) \right.\right.$$

$$\left.\left. + c_{e\theta 4}\left(r_o + \frac{\Delta r}{2}\right)^2 ln\left(\frac{\sin(\Delta\theta)}{\sin(\alpha_2)}\right) \right] E_\theta(i_s + 1, j_s, k_s)^{n+1/2} \right\} \right\}, \quad (5.4b)$$

where

$$\oiint_S \tilde{H}_{\phi 2} dS = \frac{1}{H^o_{\phi 2}} \int_{r_o - \Delta r/2}^{r_o + \Delta r/2} \int_{\theta_o + \alpha}^{\theta_o + \Delta\theta} H_{\phi 2} r d\theta dr . \quad (5.4c)$$

Additionally, the above equations are valid for $\delta < r_o - \Delta r/2$, where r_o is of the first volume cell (bottom end) of the probe model.

Fig.5.4(c) shows the same FD-TD cell of the probe model as in Fig.5.4(b), except that it is viewed on the surface $\theta = \theta_o$. Similar to the equations for updating the H_ϕ field component, ones for updating the H_θ field component lying near the probe model can be obtained by applying Faraday's law. From the figure and the near-field assumptions, the field components E_{r3}, E_{r4}, $E_{\phi 1}$, $E_{\phi 2}$, $E_{\phi 3}$, $E_{\phi 4}$, $H_{\theta 1}$ and $H_{\theta 2}$, can be written as function of r and ϕ as follows:

$$E_{r3}(r, \theta_o, \phi_o - \Delta\phi/2) = E^o_{r3}\left(\frac{r_o}{r}\right)\{1 + c_{er3}\cos(2\beta_o)[r - r_o]\}, \quad (5.5a)$$

$$E_{r4}(r, \theta_o, \phi_o + \Delta\phi/2) = E^o_{r4}\left(\frac{r_o}{r}\right)\{1 + c_{er4}\cos(2\beta_o)[r - r_o]\}, \quad (5.5b)$$

$$E_{\phi 1}(r_o - \Delta r/2, \theta_o, \phi) = E^o_{\phi 1}\frac{\sin(2\beta_o)}{\sin(2\beta_1)}\left\{1 + c_{e\phi 1}\left(r_o - \frac{\Delta r}{2}\right)[\cos(2\beta_1) - \cos(2\beta_o)]\right\}, \quad (5.5c)$$

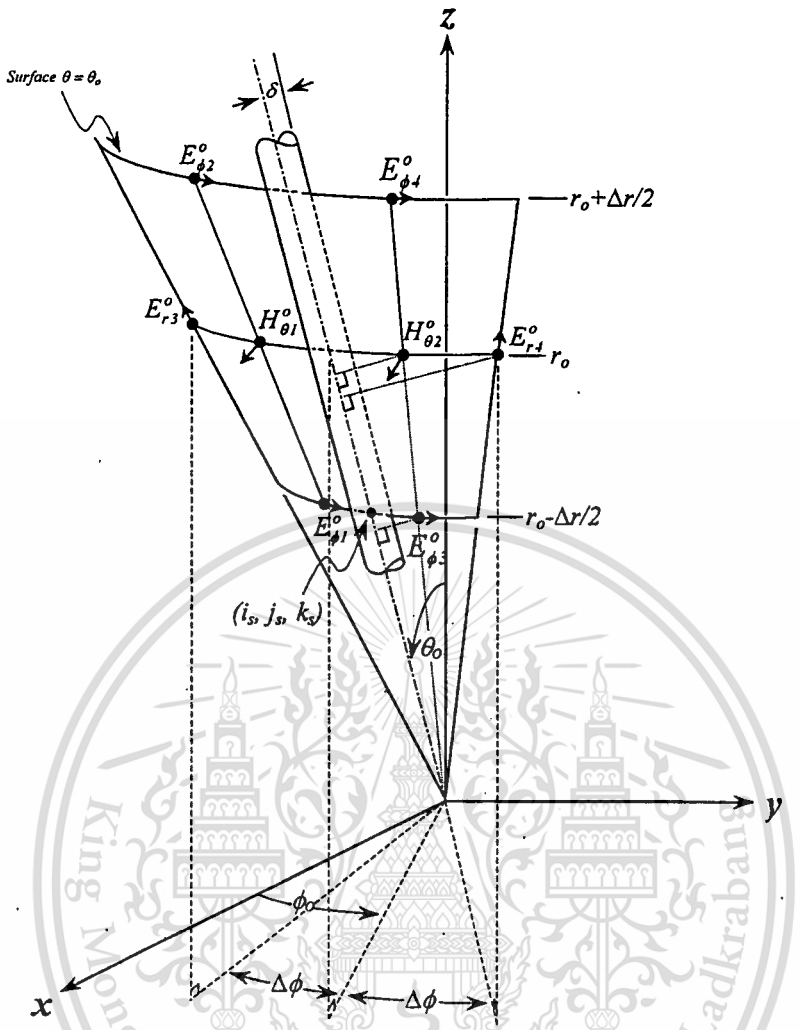

Fig. 5.4(c) The probe model and the neighboring field components on the surface $\theta = \theta_o$.

$$E_{\phi 2}(r_o + \Delta r/2, \theta_o, \phi) = E^o_{\phi 2} \frac{\sin(2\beta_o)}{\sin(2\beta_1)} \left\{ 1 + c_{e\phi 2} \left(r_o + \frac{\Delta r}{2} \right) [\cos(2\beta_1) - \cos(2\beta_o)] \right\}, \quad (5.5d)$$

$$E_{\phi 3}(r_o - \Delta r/2, \theta_o, \phi) = E^o_{\phi 3} \frac{\sin(2\beta_o)}{\sin(2\beta_2)} \left\{ 1 + c_{e\phi 3} \left(r_o - \frac{\Delta r}{2} \right) [\cos(2\beta_2) - \cos(2\beta_o)] \right\}, \quad (5.5e)$$

$$E_{\phi 4}(r_o + \Delta r/2, \theta_o, \phi) = E^o_{\phi 4} \frac{\sin(2\beta_o)}{\sin(2\beta_2)} \left\{ 1 + c_{e\phi 4} \left(r_o + \frac{\Delta r}{2} \right) [\cos(2\beta_2) - \cos(2\beta_o)] \right\}, \quad (5.5f)$$

$$H_{\theta 1}(r, \theta_o, \phi) = H^o_{\theta 1} \frac{r_o \sin(2\beta_o)}{r \sin(2\beta_1)} \{ 1 + c_{h\theta 1} [r \cos(2\beta_1) - r_o \cos(2\beta_o)] \}, \quad (5.5g)$$

$$H_{\theta 2}(r, \theta_o, \phi) = H^o_{\theta 2} \frac{r_o \sin(2\beta_o)}{r \sin(2\beta_2)} \{ 1 + c_{h\theta 2} [r \cos(2\beta_2) - r_o \cos(2\beta_o)] \}. \quad (5.5h)$$

In (5.5a) through (5.5h), the constants c_{er3}, c_{er4}, $c_{e\phi 1}$, $c_{e\phi 2}$, $c_{e\phi 3}$, $c_{e\phi 4}$, $c_{h\theta 1}$ and $c_{h\theta 2}$, are slopes of the linear functions (in the brackets, {}), which are functions of time. The parameters β_o β_1, and β_2 are defined as follows:

$$\left.\begin{aligned}\beta_o &= sin^{-1}\left(sin(\theta_o)sin(\Delta\phi)\right)\\ \beta_1 &= sin^{-1}\left(sin(\theta_o)sin(\phi_o-\phi)\right)\\ \beta_2 &= sin^{-1}\left(sin(\theta_o)sin(\phi-\phi_o)\right)\end{aligned}\right\}. \tag{5.5i}$$

By substituting (5.5a), (5.5c), (5.5d) and (5.5g) into Faraday's law, the approximate integral equation for the $H_{\theta 1}$ field component can be written as

$$\mu\frac{\partial}{\partial t}\left(H^o_{\theta 1}\right)\oiint_S \tilde{H}_{\theta 1}dS \approx E^o_{r3}\int \tilde{E}_{r3}dl - E^o_{\phi 1}\int \tilde{E}_{\phi 1}dl + E^o_{\phi 2}\int \tilde{E}_{\phi 2}dl\,, \tag{5.6a}$$

where

$$\left.\begin{aligned}\oiint_S \tilde{H}_{\theta 1}dS &= \frac{sin(\theta_o)}{H^o_{\theta 1}}\int_{r_o-\Delta r/2}^{r_o+\Delta r/2}\int_{\phi_o-\Delta\phi}^{\phi_o-\gamma} H_{\theta 1}\,r\,d\phi\,dr\\ \int \tilde{E}_{r3}dl &= \frac{1}{E^o_{r3}}\int_{r_o-\Delta r/2}^{r_o+\Delta r/2} E_{r3}dr\\ \int \tilde{E}_{o1}dl &= \frac{(r_o-\Delta r/2)sin(\theta_o)}{E^o_{o1}}\int_{\phi_o-\Delta\phi}^{\phi_o-\gamma_1} E_{o1}d\phi\\ \int \tilde{E}_{o2}dl &= \frac{(r_o+\Delta r/2)sin(\theta_o)}{E^o_{\phi 2}}\int_{\phi_o-\Delta\phi}^{\theta_o-\gamma_2} E_{o2}d\phi\end{aligned}\right\}. \tag{5.6b}$$

In (5.6b), the parameters γ, γ_1 and γ_2, are defined as follows:

$$\left.\begin{aligned}\gamma &= \frac{2\,sin\left[\frac{1}{2}sin^{-1}\left(\frac{\delta}{r}\right)\right]}{sin(\theta_o)}\\ \gamma_1 &= \frac{2\,sin\left[\frac{1}{2}sin^{-1}\left(\frac{\delta}{(r_o-\Delta r/2)}\right)\right]}{sin(\theta_o)}\\ \gamma_2 &= \frac{2\,sin\left[\frac{1}{2}sin^{-1}\left(\frac{\delta}{(r_o+\Delta r/2)}\right)\right]}{sin(\theta_o)}\end{aligned}\right\}. \tag{5.6c}$$

By applying the central time-derivative formula to (5.6a) and rearranging all field components in the form of FD-TD notations, the concurrent formula for updating the $H_{\theta 1}$ field component near the probe model can be obtained as

$$H_\theta(i_s, j_s, k_s - 1)^{n+1} = H_\theta(i_s, j_s, k_s - 1)^n + \frac{\Delta t}{\mu \oiint_S \tilde{H}_{\theta 1} dS} \times$$

$$\left\{ \begin{aligned} &\left[r_o(1 - r_o c_{er3} \cos(2\beta_o)) ln\left(\frac{r_o + \Delta r/2}{r_o - \Delta r/2} \right) + r_o \Delta r c_{er3} \cos(2\beta_o) \right] E_r(i_s, j_s, k_s - 1)^{n+1/2} \\ &+ \sin(2\beta_o) \begin{bmatrix} -(r_o - \Delta r/2)\left(\int \tilde{E}_{\phi 1} dl \right) E_\phi(i_s, j_s, k_s - 1)^{n+1/2} \\ +(r_o + \Delta r/2)\left(\int \tilde{E}_{\phi 2} dl \right) E_\phi(i_s + 1, j_s, k_s - 1)^{n+1/2} \end{bmatrix} \end{aligned} \right\}. \tag{5.7a}$$

Similarly, by using (5.5b), (5.5e), (5.5f) and (5.5h) together with Faraday's law, the recursive formula for updating the $H_{\theta 2}$ field component is obtained as

$$H_\theta(i_s, j_s, k_s)^{n+1} = H_\theta(i_s, j_s, k_s)^n + \frac{\Delta t}{\mu \oiint_S \tilde{H}_{\theta 2} dS} \times$$

$$\left\{ \begin{aligned} &-\left[r_o(1 - r_o c_{er4} \cos(2\beta_o)) ln\left(\frac{r_o + \Delta r/2}{r_o - \Delta r/2} \right) + r_o \Delta r c_{er4} \cos(2\beta_o) \right] E_r(i_s, j_s, k_s + 1)^{n+1/2} \\ &+ \sin(2\beta_o) \begin{bmatrix} -(r_o - \Delta r/2)\left(\int \tilde{E}_{\phi 3} dl \right) E_\phi(i_s, j_s, k_s)^{n+1/2} \\ +(r_o + \Delta r/2)\left(\int \tilde{E}_{\phi 4} dl \right) E_\phi(i_s + 1, j_s, k_s)^{n+1/2} \end{bmatrix} \end{aligned} \right\}, \tag{5.7b}$$

where

$$\left. \begin{aligned} \oiint_S \tilde{H}_{\theta 2} dS &= \frac{\sin(\theta_o)}{H^o_{\theta 2}} \int_{r_o - \Delta r}^{r_o + \Delta r} \int_{\phi_o + \gamma}^{\phi_o + \Delta\phi} H_{\theta 2} r d\phi dr \\ \int \tilde{E}_{\phi 3} dl &= \frac{(r_o - \Delta r/2)\sin(\theta_o)}{E^o_{\phi 3}} \int_{\phi_o + \gamma_1}^{\phi_o + \Delta\phi} E_{\phi 3} d\phi \\ \int \tilde{E}_{\phi 4} dl &= \frac{(r_o + \Delta r/2)\sin(\theta_o)}{E^o_{\phi 4}} \int_{\phi_o + \gamma_2}^{\phi_o + \Delta\phi} E_{\phi 4} d\phi \end{aligned} \right\}. \tag{5.7c}$$

Again, the above equations are valid only when $\delta < r_o - \Delta r/2$. For the above equations, there are some integration terms that cannot be expressed in closed forms, and to be evaluated by using numerical integrations.

5.2.2 Slot model

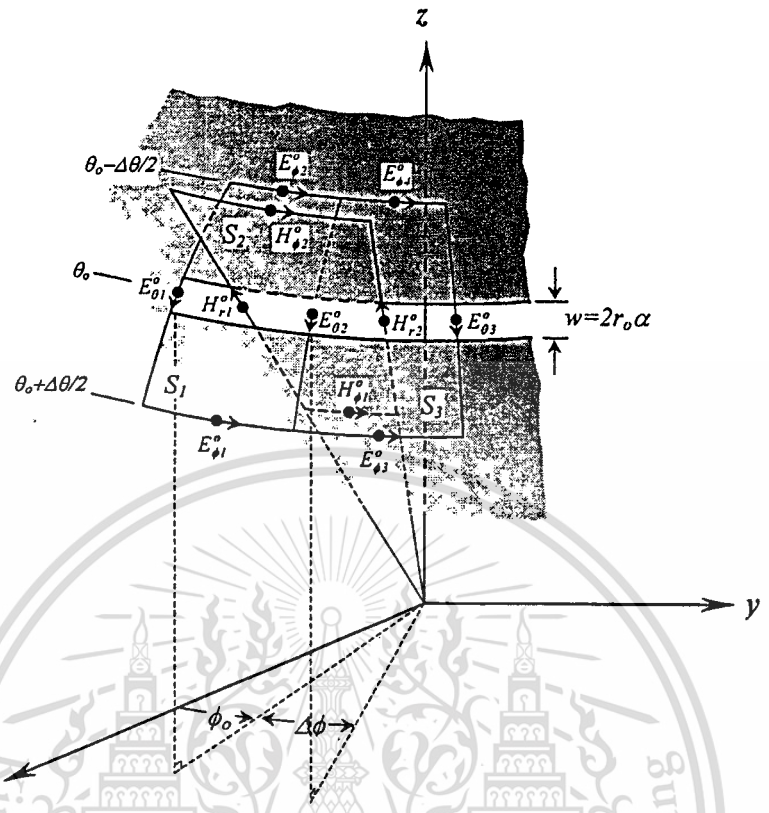

Fig. 5.5 A portion of a slot model embeded in FD-TD spherical space

Approximate FD-TD schemes for analyzing electromagnetic fields penetrating slot (or small hole) have been developed for many years. For example, *thin-slot formalism (TSF)* introduced by J. Gilbert and R.Holland [31], which is implemented by defining *in-cell* capacitance and conductance of a slot model. Another one is proposed by A. Taflove *et al.* [3]. This TSF is derived by making near-field physical assumptions and applying Faraday's law to electric and magnetic fields near a slot model. Others model, an *enhanced thin-slot formalism (ETSF)* and a *small-hole formalism (SHF)* [32-33] conducted by B. Z. Wang. The ETSF is formulated by utilizing both Faraday's and Ampere's laws, which also considered the singularities of field variation near a slot model. For the SHF, Bethe's small hole coupling theory is used to complete the formulation. All of the models above are proposed for implementing in rectangular coordinates; however, good resutls are expected if it is applied correctly in spherical coordinates. The ETSF model is applied to a slot model on a conducting constant-radius surface (r_o), here, because of their similar configurations. Also, the near-field physical assumptions of the ETSF model are adapted for applying in spherical coordinates, as being introduced below.

Fig.5.5 shows a left-end portion of a slot model on a conducting constant-radius surface (r_o). There are three typical integrating surfaces; one is on the $\theta=\theta_o$ surface (S_2) and the others are on the $r=r_o$ surface (S_1 and S_3). Additionally, the slot width is assumed to be very thin ($w << r_o\Delta\theta$), thus only the E_θ and H_r field components can propagate through it. The near-field physical assumptions of all field components lying near the slot model are asserted as follows:

(1) All field components that measured in the radial direction behave as $1/|r-r_o|$.

(2) All field components, on each of integrating surfaces and paths, that measured along the slot length each can be approximated by a linear function.

(3) A H_r field component lying near the slot-end edge has a $1/\sqrt{r_o \sin(\theta_o)(\phi-\phi_o)}$ variation along the ϕ–direction.

(4) All field components are θ-independent, due to the very thin slot assumed.

From the first assumption, it is seen that the function has a singular point at $r=r_o$, thus to avoid the singularity, some means must be considered. In [32], the equivalent antenna radius, $a=w/4$, is assumed in the slot gap. Therefore, all field components, transverse to the slot model and lie in the equivalent antenna region $2a$, can be approximated to be constants in that transverse direction and region. Here, for the slot on the $r=r_o$ surface, the equivalent antenna radius is also assumed to be $a=w/4$, but the equivalent antenna is bent along the slot length. From the assumptions and Fig.5.5, the field components E_θ, H_r and H_ϕ are written as functions of r, θ and ϕ as follows:

$$E_{\theta 2}(r,\theta,\phi)=\begin{cases} E^o_{\theta 2} & ,\text{for patches } S_1 \text{ and } S_3 \\ E^o_{\theta 2}\{1+c_{e\theta 2}\sin(\theta_o)[r\phi-r_o(\phi_o+\Delta\phi)]\} & ,|r-r_o|\le a \\ E^o_{\theta 2}\left(\dfrac{a}{|r-r_o|}\right)\{1+c_{e\theta 2}\sin(\theta_o)[r\phi-r_o(\phi_o+\Delta\phi)]\} & ,|r-r_o|>a \end{cases} \quad , \quad (5.8a)$$

$$H_{r1}(r,\theta,\phi)=\begin{cases} H^o_{r1}\sqrt{\dfrac{\Delta\phi/2}{|\phi-\phi_o|}} & ,\text{for patch } S_1 \\ H^o_{r1}\{1+c_{hr1}\sin(\theta_o)(\phi_o+\Delta\phi/2)[r-r_o]\} & ,|r-r_o|\le a \\ H^o_{r1}\left(\dfrac{a}{|r-r_o|}\right)\{1+c_{hr1}\sin(\theta_o)(\phi_o+\Delta\phi/2)[r-r_o]\} & ,|r-r_o|>a \end{cases} \quad , (5.8b)$$

$$H_{r2}(r,\theta,\phi)=\begin{cases} H^o_{r2}\left\{1+c_{hr2}r_o\sin(\theta_o)\left[\phi-\left(\phi_o+\dfrac{3\Delta\phi}{2}\right)\right]\right\} & ,\text{for patch } S_3 \\ H^o_{r2}\{1+c_{hr2}\sin(\theta_o)(\phi_o+3\Delta\phi/2)[r-r_o]\} & ,|r-r_o|\le a \\ H^o_{r2}\{1+c_{hr2}\sin(\theta_o)(\phi_o+3\Delta\phi/2)[r-r_o]\} & ,|r-r_o|>a \end{cases} \quad , (5.8c)$$

$$H_{\phi 1}\left(r_o-\frac{\Delta r}{2},\theta_o,\phi\right)=H^o_{\phi 1}\left\{1+c_{h\phi 1}\left(r_o-\frac{\Delta r}{2}\right)\sin(\theta_o)[\phi-(\phi_o+\Delta\phi)]\right\}, \quad (5.8d)$$

$$H_{\phi 2}\left(r_o+\frac{\Delta r}{2},\theta_o,\phi\right)=H^o_{\phi 2}\left\{1+c_{h\phi 2}\left(r_o+\frac{\Delta r}{2}\right)sin(\theta_o)[\phi-(\phi_o+\Delta\phi)]\right\}. \quad (5.8e)$$

By applying Ampere's law,

$$\varepsilon\frac{\partial}{\partial t}\oiint_S \bar{E}\cdot d\bar{S}=\oint_C \bar{H}\cdot d\bar{l}\,, \quad (5.9)$$

to the patch S_2, an approximate integral equation for the $E_{\theta 2}$ component is obtained as

$$\varepsilon\frac{\partial}{\partial t}\left(E^o_{\theta 2}\right)\oiint_{S_2}\tilde{E}_{\theta 2}dS\approx -H^o_{r1}\int\tilde{H}_{r1}dl+H^o_{r2}\int\tilde{H}_{r2}dl+H^o_{\phi 1}\int\tilde{H}_{\phi 1}dl-H^o_{\phi 2}\int\tilde{H}_{\phi 2}dl\,, \quad (5.10a)$$

where

$$\left.\begin{aligned}
\oiint_{S_2}\tilde{E}_{\theta 2}dS&=\frac{sin(\theta_o)}{E^0_{\theta 2}}\int_{r_o-\Delta r/2}^{r_o+\Delta r/2}\int_{\phi_o+\Delta\phi/2}^{\phi_o+3\Delta\phi/2}rE_{\theta 2}d\phi dr\\
\int\tilde{H}_{r1}dl&=\frac{1}{H^o_{r1}}\int_{r_o-\Delta r/2}^{r_o+\Delta r/2}H_{r1}dr\\
\int\tilde{H}_{r2}dl&=\frac{1}{H^o_{r2}}\int_{r_o-\Delta r/2}^{r_o+\Delta r/2}H_{r2}dr\\
\int\tilde{H}_{\phi 1}dl&=\frac{(r_o-\Delta r/2)sin(\theta_o)}{H^o_{\phi 1}}\int_{\phi_o+\Delta\phi/2}^{\phi_o+3\Delta\phi/2}H_{\phi 1}d\phi\\
\int\tilde{H}_{\phi 2}dl&=\frac{(r_o+\Delta r/2)sin(\theta_o)}{H^o_{\phi 2}}\int_{\phi_o+\Delta\phi/2}^{\phi_o+3\Delta\phi/2}H_{\phi 2}d\phi
\end{aligned}\right\}. \quad (5.10b)$$

By applying the central time-derivative formula to (5.10a) and representing it in the form of FD-TD notations, the recursive equation for updating the $E_{\theta 2}$ field component in the slot gap is

$$E_\theta(i_s,j_s,k_s+1)^{n+1/2}=E_\theta(i_s,j_s,k_s+1)^{n-1/2}+\frac{\Delta t}{\varepsilon}\frac{1}{(2a)sin(\theta_o)}$$

$$\times\frac{1}{\left\{r_o\left[\Delta\phi+ln\left(\frac{\Delta r/2}{a}\right)\right]+c_{e\theta 2}\,sin(\theta_o)\Delta\phi(\phi_o+\Delta\phi)\left[\frac{\Delta r^2}{8}-\frac{a^2}{6}+(r_o+r_o^2)ln\left(\frac{\Delta r/2}{a}\right)\right]\right\}}$$

$$\times\left\{\begin{aligned}&(2a)\left[1+r_o\,ln\left(\frac{\Delta r/2}{a}\right)\right]\left[H_r(i_s,j_s,k_s+1)^n-H_r(i_s,j_s,k_s)^n\right]\\&+sin(\theta_o)\Delta\phi\left[\left(r_o-\frac{\Delta r}{2}\right)H_\phi(i_s-1,j_s,k_s)^n-\left(r_o+\frac{\Delta r}{2}\right)H_\phi(i_s,j_s,k_s)^n\right]\end{aligned}\right\} \quad (5.10c)$$

Similarly, by applying Faraday's law to the patch S_1, yields

$$\mu\frac{\partial}{\partial t}\left(H_{r1}^{o}\right)\iint_{S_1}\tilde{H}_{r1}dS \approx E_{\theta 2}^{o}\int\tilde{E}_{\theta 2}dl\,, \tag{5.11a}$$

where

$$\left.\begin{aligned}\iint_{S_1}\tilde{H}_{r1}dS &= \frac{r_o^2}{H_{r1}^{o}}\int_{\theta_o-\alpha}^{\theta_o+\alpha}\int_{\phi_o}^{\phi_o+\Delta\phi}\sin(\theta)H_{r1}d\phi d\theta\\ \int\tilde{E}_{\theta 2}dl &= \frac{r_o}{E_{\theta 2}^{o}}\int_{\theta_o-\alpha}^{\theta_o+\alpha}E_{\theta 2}d\theta\end{aligned}\right\}. \tag{5.11b}$$

After integrating (5.11b) and rewriting it in the form of FD-TD notations, the equation for updating the H_{r1} field component is obtained as

$$H_r(i_s,j_s,k_s)^{n+1} = H_r(i_s,j_s,k_s)^{n-1} + \frac{\Delta t}{\mu}\times \frac{\sqrt{2}\alpha}{r_o\left[\cos(\theta_o-\alpha)-\cos(\theta_o+\alpha)\right]\Delta\phi}E_\theta(i_s,j_s,k_s+1)^{n+1/2}\,. \tag{5.11c}$$

Finally, an integral equation over the patch S_3 can be done, again by using Faraday's law, which can be written as

$$\mu\frac{\partial}{\partial t}\left(H_{r2}^{o}\right)\iint_{S_3}\tilde{H}_{r2}dS \approx E_{\theta 3}^{o}\int\tilde{E}_{\theta 3}dl - E_{\theta 2}^{o}\int\tilde{E}_{\theta 2}dl\,, \tag{5.12a}$$

where

$$\left.\begin{aligned}\iint_{S_3}\tilde{H}_{r2}dS &= \frac{r_o^2}{H_{r2}^{o}}\int_{\theta_o-\alpha}^{\theta_o+\alpha}\int_{\phi_o+\Delta\phi}^{\phi_o+2\Delta\phi}\sin(\theta)H_{r2}d\phi d\theta\\ \int\tilde{E}_{\theta 2}dl &= \frac{r_o}{E_{\theta 2}^{o}}\int_{\theta_o-\alpha}^{\theta_o+\alpha}E_{\theta 2}d\theta\\ \int\tilde{E}_{\theta 3}dl &= \frac{r_o}{E_{\theta 3}^{o}}\int_{\theta_o-\alpha}^{\theta_o+\alpha}E_{\theta 3}d\theta\end{aligned}\right\}. \tag{5.12b}$$

After the integration, (5.12a) can be represented in FD-TD notations as

$$H_r(i_s,j_s,k_s+1)^{n+1} = H_r(i_s,j_s,k_s+1)^{n} + \frac{\Delta t}{\mu}\times \frac{4\alpha}{r_o\left[\begin{aligned}&-(\phi_o+\Delta\phi)(-2+c_{hr2}r_o\sin(\theta_o)(\phi_o+2\Delta\phi))\cos(\alpha-\theta_o)\\ &+(\phi_o+2\Delta\phi)(-2+c_{hr2}r_o\sin(\theta_o)(\phi_o+\Delta\phi))\cos(\alpha+\theta_o)\end{aligned}\right]}\times \left[E_\theta(i_s,j_s,k_s+2)^{n+1/2}-E_\theta(i_s,j_s,k_s+1)^{n+1/2}\right]. \tag{5.12c}$$

An equation for updating the H_r field component near the right-end edge of the slot can be achieved in the similar manner as done for the H_{r1} component. Also, ones for updating all other H_r and E_θ components lying somewhere else between the two slot edges can be similarly derived as shown for the H_{r2} and E_θ field components, respectively.

5.3 Near-to-Far Field Transformations

As illustrated in the previous chapters, the FD-TD method accurately computes electromagnetic fields inside or near objects of interests. However, the method becomes an inconvenient tool for direct far-field analysis, by directly extending a computational space to reach the far-field region. This is a restriction of the method because of the computational costs and the numerical phase velocity errors that mentioned before, in chapter 2. Thus, one needs auxiliary schemes to achieve the far-field responses. Many FD-TD schemes of transforming zones of fields are proposed [11, 34]. In this section, two standard schemes are introduced. The first classical one is called *frequency-domain near-to-far field transformation (FD-NFFF)*, which is usually useful for obtaining single-frequency radiation patterns. Another new one is known as *time-domain near-to-far field transformation (TD-NFFF)*, which is frequently used to obtain antenna gain (broadband) and time-dependent radiation patterns (e.g. an antenna excited by a pulse source). Although the purposes of the two methods are different, the basic idea about zone transformations is the same.

The idea of transforming zones of fields, specifically for a transmitting antenna model, can be illustrated in Fig.5.6(a). Referring to the figure, an arbitrary antenna structure is enclosed by a virtual surface (dashed lines) and an ABC (or RBC). Usually, the virtual surface is placed somewhere between the antenna and the ABC. Then, field transformations are performed on the virtual surface to obtain the far-zone responses.

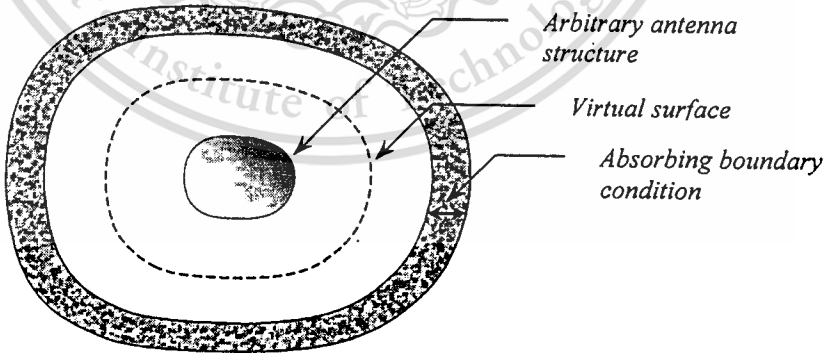

Fig. 5.6(a) Configuration of a problem that a zone transformation is to be performed.

Details of zone transformations over the virtual surface are shown in Fig.5.6(b). From the figure, $\bar{r}'$ is a radial vector originated at an arbitrary reference point (inside the virtual surface) to a point on the virtual surface. For each point on the surface, there is a unit normal vector, $\bar{a}_n$. To transform fields on the surface, a far-field observing point is selected, (r, θ, ϕ); a distance r is measured from the reference point to the far-field point or magnitude of a vector, $\bar{r}$. A distance mesured

from a point on the virtual surface to the far-field point, magnitude of $\bar{r}-\bar{r}'$, causes a delay time that waves need to reach the far-field point, $|\bar{r}-\bar{r}'|/c$, where c is the speed of light. Distributions of all tangential fields on the surface to the far-field observation point are integrated over the entire virtual surface. Then, a new observation point is selected and field distributions are integrated again, and so on. Finally, far-field responses are obtained, for example, radiation patterns. As mentioned before, the two methods of transformations have different purposes. They also have some different procedures in computations, and will be presented in the following sub-sections.

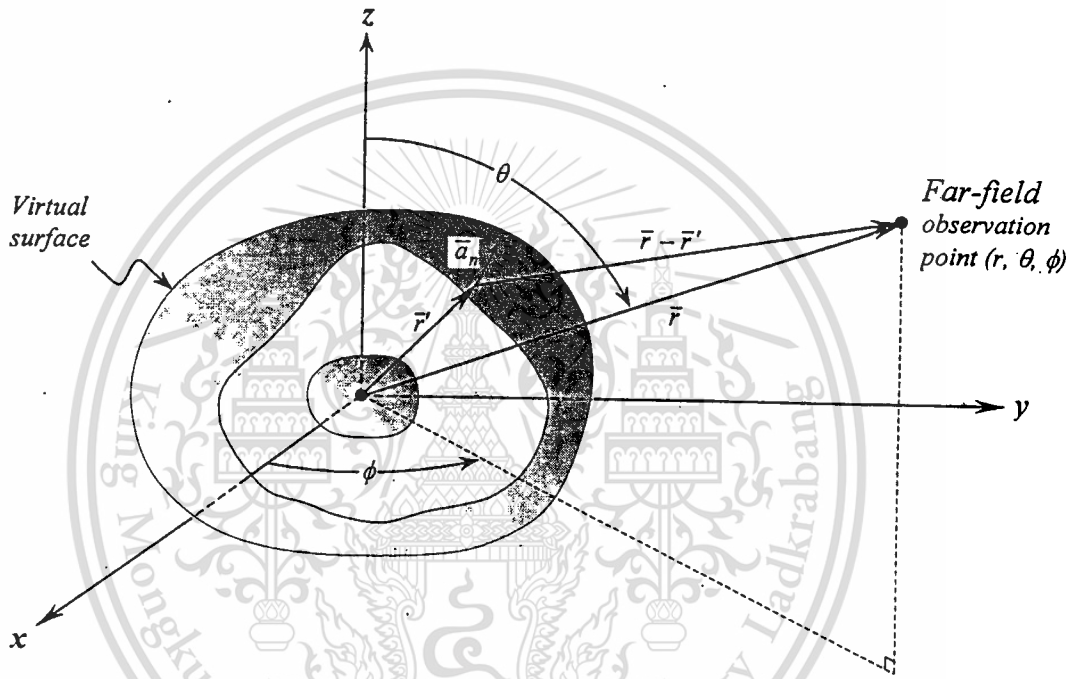

Fig. 5.6(b) Details of zone transformations over the virtual surface.

5.3.1 Frequency-domain near-to-far field transformation

One analytic form of Huygens' principle, in frequency-domain, is written as

$$\bar{E}^r(\bar{r},\omega)=\frac{j\omega\mu_o}{4\pi r}\iint_S\left\{\bar{a}_r\times\left[\bar{a}_r\times\left[\bar{a}_n\times\bar{H}(\bar{r}',\omega)\right]\right]-\frac{1}{\eta_o}\bar{a}_r\times\left[\bar{a}_n\times\bar{E}(\bar{r}',\omega)\right]\right\}\times exp\left(-j\omega t_{delay}\right)dS', \tag{5.13a}$$

where t_{delay} is defined as

$$t_{delay}=\frac{r-\bar{a}_r\cdot\bar{r}'}{c}. \tag{5.13b}$$

From (5.13a), electric and magnetic fields are crossed with a unit normal vector (at each point on the virtual surface) to ensure that only their tangential components are left for the transformations. If the resultant cross products are not already in spherical coordinates, a coordinate transformation (to spherical coordinates) is required. Even

the fields are in spherical coordinates but the origin of the coordinates does not coincide with the reference point of the zone transformations, the coordinate transformation is still required. Thus, for general, the coordinate transformation of the above primary cross-product terms are assumed to be

$$\left[\bar{a}_n \times \bar{H}(\bar{r},\omega)\right]_{spherical} = \bar{a}_r\left[\bar{a}_n \times \bar{H}\right]_r + \bar{a}_\theta\left[\bar{a}_n \times \bar{H}\right]_\theta + \bar{a}_\phi\left[\bar{a}_n \times \bar{H}\right]_\phi \qquad (5.14a)$$

and

$$\left[\bar{a}_n \times \bar{E}(\bar{r},\omega)\right]_{spherical} = \bar{a}_r\left[\bar{a}_n \times \bar{E}\right]_r + \bar{a}_\theta\left[\bar{a}_n \times \bar{E}\right]_\theta + \bar{a}_\phi\left[\bar{a}_n \times \bar{E}\right]_\phi . \qquad (5.14b)$$

By subsituting (5.14a) and (5.14b) to (5.13a) and rearranging terms, it is found that only the θ and ϕ components are remaining as shown below,

$$rE_\theta^r(\bar{r},\omega) = \frac{j\omega\mu_o\Delta S'}{4\pi}\sum_{\substack{entire\\surface}}\left(-\left[\bar{a}_n \times \bar{H}\right]_\theta + \frac{1}{\eta_o}\left[\bar{a}_n \times \bar{E}\right]_\phi\right)\times exp\left(-j\omega t_{delay}\right) \qquad (5.15a)$$

and

$$rE_\phi^r(\bar{r},\omega) = \frac{j\omega\mu_o\Delta S'}{4\pi}\sum_{\substack{entire\\surface}}\left(-\left[\bar{a}_n \times \bar{H}\right]_\phi - \frac{1}{\eta_o}\left[\bar{a}_n \times \bar{E}\right]_\theta\right)\times exp\left(-j\omega t_{delay}\right). \qquad (5.15b)$$

In (5.15a) and (5.15b), $\Delta S'$ is an area of each of the discretized FD-TD patches on the virtual surface. It should be noted that all field components in the above equations are in frequency-domain, thus the Discrete Fourier Transformation (DFT) is needed. The DFT is defined as follows:

$$U(\bar{r},\omega) = \sum_{n=1}^{N} U\big|_{\bar{r}}^{n}\, exp(-j\omega n\Delta t), \qquad (5.16a)$$

where U can be any field component, N is a maximum number of time steps. Hence, one cannot apply (5.15a) and (5.15b), before the FD-TD calculation has finished. In other words, the FD-NFFF is the postprocessing method. The simplest way to achieve the DFT of fields is storing full-time history of all fields on the entire virtual surface, and then (5.16a) is applied. For example, if there are M discretized patches on the virtual surface (each containing four tangential field components), the required amount of storage is about $4MN$ (real numbers) per transforming frequency. In some situations, a large number of N is needed to make the FD-TD simulation reach its steady-state, then the storage space may be excessive. An alternate means, which can reduce the amount of storage, is doing the DFT *on-the-fly* in step with the FD-TD calculation. The idea is that each field component on each discretized patch is summed in the recursive manner as shown below,

$$U(\bar{r},\omega) + U\big|_{\bar{r}}^{n} exp(-j\omega n\Delta t) \rightarrow U(\bar{r},\omega), \qquad (5.16b)$$

where the arrow indicates that the resultant summing of the left-hand-side is stored back to the same variable, $U(\bar{r},\omega)$. Thus, this can reduce the amount of storage to be about only $4M$ (complex numbers) or $8M$ (real numbers). Finally, (5.15a) and (5.15b) are applied to get the radiated fields, E_θ^r and E_ϕ^r.

5.3.2 Time-domain near-to-far field transformation

As a counterpart of the FD-NFFF method, time-domain Huygen's principal can be written as follows:

$$\bar{E}^r(\bar{r},t)=\frac{j\omega\mu_o}{4\pi r}\oiint_S\left\{\bar{a}_r\times\left[\bar{a}_r\times\frac{\partial}{\partial t'}\left[\bar{a}_n\times\bar{H}(\bar{r}',t')\right]\right]-\frac{1}{\eta_o}\bar{a}_r\times\frac{\partial}{\partial t'}\left[\bar{a}_n\times\bar{E}(\bar{r}',t')\right]\right\}_{t'=t_r}dS', \tag{5.17a}$$

where t_r is the retarded time, which is defined as

$$t_r=t-t_{delay}. \tag{5.17b}$$

Similar to the FD-NFFF method, the radiated electric field components are obtained as

$$rE_\theta^r(\bar{r},\omega)=\frac{\mu_o\Delta S'}{4\pi}\sum_{\substack{entire\\surface}}\left(-\frac{\partial}{\partial t'}\left[\bar{a}_n\times\bar{H}\right]_\theta+\frac{1}{\eta_o}\frac{\partial}{\partial t'}\left[\bar{a}_n\times\bar{E}\right]_\phi\right)_{t'=t_r} \tag{5.18a}$$

and

$$rE_\phi^r(\bar{r},\omega)=\frac{\mu_o\Delta S'}{4\pi}\sum_{\substack{entire\\surface}}\left(-\frac{\partial}{\partial t'}\left[\bar{a}_n\times\bar{H}\right]_\phi-\frac{1}{\eta_o}\frac{\partial}{\partial t'}\left[\bar{a}_n\times\bar{E}\right]_\theta\right)_{t'=t_r}. \tag{5.18b}$$

As mentioned in the previous sub-section, storing all tangential fields at every time step is prohibitive, thus only the recursive approach is considered, here. For illustrating the idea, (5.18a) is selected as an example and can be rewritten as

$$rE_\theta^r(\bar{r},\omega)=\frac{\mu_o}{4\pi}\left(-\frac{\partial}{\partial t}U_\theta^H+\frac{1}{\eta_o}\frac{\partial}{\partial t}U_\theta^E\right). \tag{5.19a}$$

In (5.19a), there are two new variables, U_θ^H and U_θ^E, which are defined by

$$U_\theta^H(t)=\Delta S'\sum_{\substack{entire\\surface}}\left(\left[\bar{a}_n\times\bar{H}\right]_\theta\right)_{t'=t_r} \tag{5.19b}$$

and

$$U_\theta^E(t)=\Delta S'\sum_{\substack{entire\\surface}}\left(\left[\bar{a}_n\times\bar{E}\right]_\phi\right)_{t'=t_r} \tag{5.19c}$$

In the above function, $U_\theta^H(t)$ and $U_\theta^E(t)$, are computed incrementally each time step for each of the discretized patches during the FD-TD simulation. On some patches, the being calculated t_r's may not coincide with the known time step $n\Delta t$, thus the time interpolation should be considered. A typical linear interpolation is implemented as follows:

$$U_\theta^H\Big|^n = \Delta S'\left\{\left(1-q^H\right)\left[\bar{a}_n \times \bar{H}\right]_\theta^{n-n_{delay}^H} + \left(q^H\right)\left[\bar{a}_n \times \bar{H}\right]_\theta^{n-n_{delay}^H+1}\right\}, \quad (5.20a)$$

$$U_\theta^E\Big|^n = \Delta S'\left\{\left(1-q^E\right)\left[\bar{a}_n \times \bar{E}\right]_\phi^{n-n_{delay}^E} + \left(q^E\right)\left[\bar{a}_n \times \bar{E}\right]_\phi^{n-n_{delay}^E+1}\right\}. \quad (5.20b)$$

where

$$n_{delay}^i = Int\left(t_{delay}/\Delta t\right), \quad q^i = \left(t_{delay}/\Delta t\right) - n_{delay}^i. \quad (5.20c)$$

In (5.20c), i can be either E or H, and $Int(\cdot)$ is the greatest integer function. After the FD-TD calculation has finished, the stored $U_\theta^H\Big|^n$ and $U_\theta^E\Big|^n$ on all patches are used as the distributions to the radiated field $E_\theta^r\Big|^n$. The discretized time-domain field, $E_\theta^r\Big|^n$, can be derived from (5.19a) as

$$rE_\theta^r\Big|_{\bar{r}}^n = \frac{\mu_o}{4\pi\Delta t}\left(-\left[U_\theta^H\Big|^{n+1} - U_\theta^H\Big|^n\right] + \frac{1}{\eta_o}\left[U_\theta^E\Big|^{n+1} - U_\theta^E\Big|^n\right]\right). \quad (5.21a)$$

In the similar manner, $rE_\phi^r\Big|^n$ can be derived as

$$rE_\phi^r\Big|_{\bar{r}}^n = \frac{\mu_o}{4\pi\Delta t}\left(-\left[U_\phi^H\Big|^{n+1} - U_\phi^H\Big|^n\right] - \frac{1}{\eta_o}\left[U_o^E\Big|^{n+1} - U_o^E\Big|^n\right]\right), \quad (5.21b)$$

where the new variables, U_ϕ^H and U_o^E, are defined by

$$U_\phi^H(t) = \Delta S' \sum_{\substack{entire \\ surface}} \left(\left[\bar{a}_n \times \bar{H}\right]_\phi\right)_{t'=t_r} \quad (5.21c)$$

and

$$U_\phi^E(t) = \Delta S' \sum_{\substack{entire \\ surface}} \left(\left[\bar{a}_n \times \bar{E}\right]_\theta\right)_{t'=t_r}. \quad (5.21d)$$

Equation (5.21a) and (5.21b) are used to construct time-domain radiation patterns for pulse-excited antennas. If broadband gains are required, the discretized time-domain fields, $E_\theta^r\Big|^n$ and $E_\phi^r\Big|^n$, must be firstly transformed into frequency-domain by using (5.16a); and then the gains are computed. The definitions and formulas of gains will be typically introduced in the next chapter.

5.4 Conclusions

In this chapter, the FD-TD models for feeding an antenna by a probe and penetrating through a slot, in spherical coordinates, are developed. The modeling schemes are classified into two categories: (1) detailed or fine model and (2) approximate model.

The detailed models are found easy to achieve by using very high resolutions for FD-TD gridding. Then, the very small volume cells are allocated to conform to the shapes of the designed probe and slot models. Some discretization errors are expected for the probe model, while there is no problem in modeling the slot, except that the slot's alignment is inclined. Although the detailed modeling is easy and accurate, the computational costs may be excessive for some applications. The subgridding algorithm by factor of *2* is also introduced, which can reduce the computational costs to be about half of that required for the very high resolution.

For approximate models, physical assumptions of fields near objects of interests must firstly be postulated. Then, integral forms of Faraday's law and/or Ampere's law are applied. Evidently, the approximate models are more difficult to obtain than the detailed models, and risk of modeling errors due to wrong physical assumptions. However, the advantage of this modeling style is that any model can be implemented in a normal-resolution FD-TD space.

As the last topic, the methods of transforming zones of fields are discussed. There are two standard zone transformations introduced: (1) frequency-domain near-to-far field transformation (FD-NFFF) and (2) time-domain near-to-far field transformation (TD-NFFF). The FD-NFFF method is used to construct a complete radiation pattern for a selected frequency. The TD-NFFF is conveniently applied to obtain time-domain radiation patterns and broadband gains for pulse-excited antennas. Usually, both of them are often used in FD-TD simulations for antenna problems.

Chapter 6

An Antenna Using a Probe Excited Slotted Hemispherical Cavity

As mentioned in the preliminary part of the previous chapter, all the knowledge about the FD-TD algorithm in spherical coordinates, cavity and slot models will be integrated to construct an antenna model in this chapter. A selected antenna model is slots on a hemispherical cavity. The antenna is analyzed in two cases, with and without ground plane. The deviced FD-TD probe and slot models are implemented for approximate models. Four antenna parameters are considered: (1) input impedance, (2) radiation pattern, (3) gain and (4) directivity. Here, the first two parameters are to be calculated by using the FD-TD method in spherical coordinates. Details in modeling the antenna and analyzing its parameters are discussed step by step in the following sub-sections.

6.1 Antenna Model

The configuration of the antenna model is shown in Fig.6.1. In the figure, the antenna is excited by a conical probe having a half-cone angle α and length R_f. The raduis of the conducting hemispherical cavity is R_b. There are four zonal slots on the cavity wall, each has length l and width w. The slots are arranged such that their centers are at azimuth angles (ϕ_s). Each of them is at the elevation angle (θ_s). The values of antenna dimensional parameters are shown in Table 6.1.

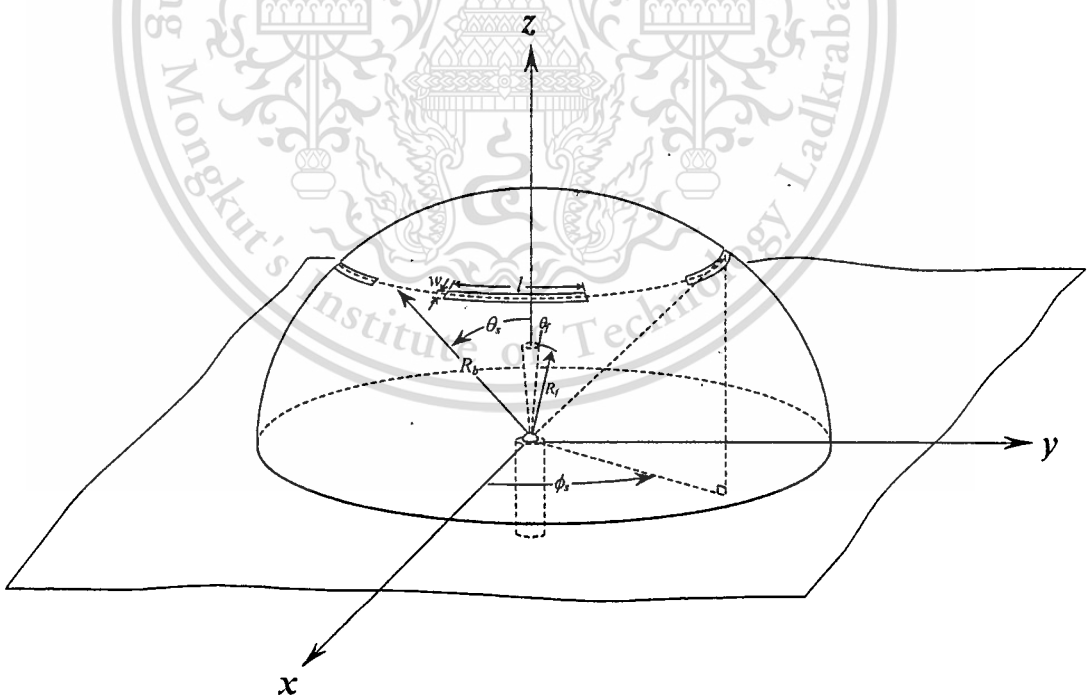

Fig. 6.1 A slotted hemispherical antenna model

Table 6.1 Values of the antenna dimensional parameters

Dimensional parameters	Values
Operating frequency	*3.18* GHz
R_b	*7.50* m ($0.80\lambda_o$)
R_f	*2.34* cm ($0.25\lambda_o$)
θ_f	*2.45°*
l	*4.72* cm ($0.50\lambda_o$)
w	*1.89* mm ($0.02\lambda_o$)
θ_s	*45°*
ϕ_s	*45°, 135°, 225°* and *315°*

In FD-TD analysis, the above antenna model is considered into two cases, with and without infinite ground plane. Also, the elevation angle of the slot models (θ_s) and the probe length are varied to study behaviours of the antenna parameters. Details in analyzing the antenna by using the FD-TD method are considered in the following sections.

6.2 FD-TD Model

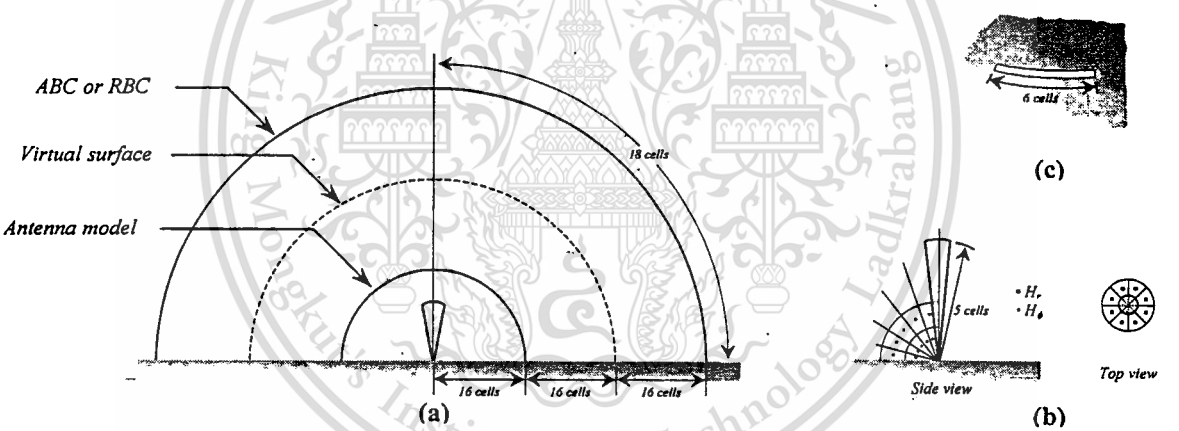

Fig. 6.2 **(a)** Problem configuration after discretizing
(b) Details of field components near the probe model
(c) Discretized slot model

As mentioned in chapter 4, the first step in modeling any problem by using the FD-TD method, after problem dimensions are obtained, is subdividing a problem space. In subdividing the antenna model above, it is importnant to fit the discretized volume cells to shapes of the modeling objects. All the models, hemisphrical cavity, probe and slot models, are considered at the same time to obtain the constant incremental space parameters, Δr, $\Delta\theta$ and $\Delta\phi$, otherwise non-uniform FD-TD space parameters are required. From Table 6.1, the hemisphrical cavity, probe and slot models are best fitted when the FD-TD incremental space parameters are as follows: $\Delta r = 0.075/16 = 0.0046875$ *m*, $\Delta\theta = (\pi/2)/18 = 0.0872665$ *radain* and $\Delta\phi = (2\pi)/44 = 0.1428000$ *radain*. The above radial increment, Δr, is also satisfying the normal resolution, as discussed in the previous chapter. In radial direction, the FD-TD space must be extended out to handle the virtual surface and the ABC or RBC, as shown in

Fig.5.6, thus additional cells (extended out from the antenna) are designed to be *32* cells. Then, the FD-TD maximum space indices are $I_{max} = 48$, $J_{max} = 18$ and $K_{max} = 44$. The cross-section view of the antenna model, after discretization, is shown in Fig.6.2(a). From the figure, the feed point and the slot model are magnified in Fig.6.2(b) and Fig.6.2(c), respectively. In Fig.6.2(b), the H_r and H_ϕ field components that lie along the probe model and near the transmission line's aperture are updated by applying Faraday's law, as described in section 5.2. It is seen that the probe model is discretized into *5* FD-TD cells, in radial direction. For the discretized slot model (Fig.6.2(c)), the slot is subdivided into *6* FD-TD cells, in ϕ-direction. The updating equations for the E_θ and H_r field components are presented in section 5.2.2.

For source excitation, the *magnetic frill* [11, 27] model is used to distribute the time-harmonic voltage at the base of the probe model as shown in Fig.6.3(a). In general antenna modeling, two time-harmonic voltage functions are often used, the ramped sinusoidal function (4.12b) and Gaussian pulse functions. The ramped sinusoidal function is usually used to analyze an antenna at a single frequency and rather unpopular. The gaussian pulse functions are more frequently used to obtain antenna responses at broadband frequency. There are two Gaussian pulse functions introduced here, a normal Gaussian pulse

$$V = V_o e^{\left[-(t/\tau_p)^2/2\right]}, \tag{6.1a}$$

and a differentiated Gaussian pulse

$$V = -V_o \left(\frac{t}{\tau_p}\right) e^{\left\{-\left[(t/\tau_p)^2-1\right]/2\right\}}, \tag{6.1b}$$

where τ_p is the characteristic time. The Gaussian pulses, (6.1a) and (6.1b), are plotted in Fig.6.3(b) and Fig.6.3(c), respectively. In Fig.6.3(b), the normal Gaussian pulse has high spectrum content near a low frequency range, sometimes, it is not disired for applications involving high frequency ranges. As an alternative, the differentiated Gaussian pulse is implemented in such applications because the pulse peaks at the frequency, $\omega_p = 1/\tau_p$, which can be selected by users.

The boundary conditions for the FD-TD electric and magnetic fields, at the conducting hemispherical cavity's wall are similar to that discussed in section 4.4 (spherical conducting cavity model). Additionally, the E_r and E_ϕ or H_θ field components must be set to be zero on the ground plane as shown below,

$$E_r\big|_{j=J\,max} = 0, \tag{6.2a}$$

$$E_\phi\big|_{j=J\,max} = 0, \tag{6.2b}$$

$$H_\theta\big|_{j=J\,max} = 0, \tag{6.2c}$$

where the J_{max} index is exactly truncated at the ground plane. For the outermost surface, $r(I_{max})$, the two schemes of radiation boundary conditions (RBCs), discussed in section 3.3, can be implemented. However, it is found that the two schemes require

additional storage space in computations. As an alternative means, the first-order Bayliss-Turkel annihilator [11] for spherical coordiantes can be applied, without additional storage space required in computations. The Bayliss-Turkel annihilator of order n (for spherical coordiantes) is defined by

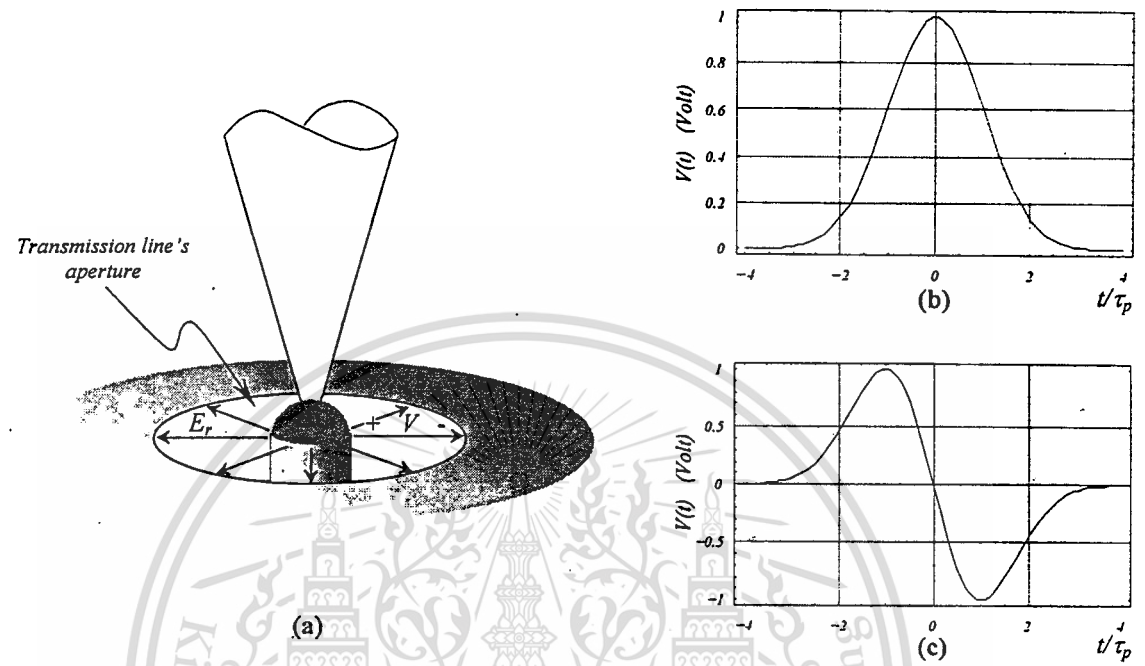

Fig. 6.3 (a) Details at feed point
(b) Gaussian pulse waveform
(c) Differentiated Gaussian pulse waveform

$$B_n = \prod_{k=1}^{n}\left(L+\frac{2k-1}{r}\right) = \left(L+\frac{2n-1}{r}\right)\cdots\left(L+\frac{5}{r}\right)\left(L+\frac{3}{r}\right)\left(L+\frac{1}{r}\right), \qquad (6.3a)$$

where L is the partial derivative operator,

$$L \equiv \frac{1}{c}\frac{\partial}{\partial t}+\frac{\partial}{\partial r}. \qquad (6.3b)$$

When one applies this annihilator to any field component, $\psi(r, \theta, \phi, t)$, which is a function of angular position and radiating (outward) in radial direction, significant terms of $\psi(r, \theta, \phi, t)$ are all annihilated, leaving only less-significant terms. This means that almost all of the fields radiate outward at the outermost surface, permitting only less-significant reflected waves; which can be thought as being zero. From (6.3a), the first-order Bayliss-Turkel annihilator is obtained as

$$B_1 = L+\frac{1}{r}. \qquad (6.4a)$$

By applying (6.4a) to the field component $\psi(r, \theta, \phi; t)$, one obtains

$$B_1\psi = \frac{1}{c}\frac{\partial \psi}{\partial t} + \frac{\partial \psi}{\partial r} + \frac{\psi}{r} \approx 0, \tag{6.4b}$$

By using the space derivative (3.4a) and time derivative (3.4b) approximations with each term at the right-hand-side of (6.4b) and rewriting them in form of the FD-TD notations, this yields

$$\left.\begin{aligned} \frac{1}{c}\frac{\partial \psi}{\partial t} &= \frac{1}{2c\Delta t}\left[\psi\big|_{Ro}^{n} - \psi\big|_{Ro}^{n-1} + \psi\big|_{Rp}^{n} - \psi\big|_{Rp}^{n-1}\right] \\ \frac{\partial \psi}{\partial R} &= \frac{1}{2\Delta r}\left[\psi\big|_{Ro}^{n} - \psi\big|_{Rp}^{n} + \psi\big|_{Ro}^{n-1} - \psi\big|_{Rp}^{n-1}\right] \\ \frac{\psi}{r} &= \frac{1}{4}\left[\frac{\psi\big|_{Ro}^{n} + \psi\big|_{Ro}^{n-1}}{Ro} + \frac{\psi\big|_{Rp}^{n} + \psi\big|_{Rp}^{n-1}}{Rp}\right] \end{aligned}\right\}, \tag{6.4c}$$

where Ro and Rp are the radial distance at the outermost surface $r(I_{max})$ and at one-cell inner surface $r(I_{max}\text{-}1)$. Addtionally, the above equation is not only approximated by simple finite-difference approximations but also averaged in space and time to obtain good stability in calculations. By substituting (6-4c) to (6.4b), the annihilating equation that is used to cancel out fields on the outermost boundary is obtained as,

$$\begin{aligned} \psi\big|_{Ro}^{n} = {} & \frac{Ro}{Rp}\left(\frac{2c\Delta tRp - c\Delta r\Delta t - 2\Delta rRp}{S}\right)\psi\big|_{Rp}^{n} \\ & -\left(\frac{2c\Delta tRo + c\Delta r\Delta t - 2\Delta rRo}{S}\right)\psi\big|_{Ro}^{n-1} \\ & +\frac{Ro}{Rp}\left(\frac{2c\Delta tRp - c\Delta r\Delta t + 2\Delta rRp}{S}\right)\psi\big|_{Rp}^{n-1}, \end{aligned} \tag{6.4d}$$

where S is defined by

$$S = 2c\Delta tRo + c\Delta r\Delta t + 2\Delta rRo\,. \tag{6.4e}$$

At the outermost surface, (6.4d) is used to update the tangential field components, E_θ and E_ϕ, while the other field components lying inside the outermost surface are updated by the normal FD-TD algorithm.

At this point, the FD-TD antenna model is ready for simulations, to analyze near field responses. If the far field responses are wanted, the field transformations presented in the previous chapter are required. As discussed in section 5.3, the near-field data can be efficiently transformed to the far field region by using either the FD-NFFF or TD-NFFF. From Fig.6.2(a), if the origin point is selected as a reference point of field transformations, it is evident that the coordinate transformation is not required. Moreover, only four tangential field components (E_θ, E_ϕ, H_θ and H_ϕ) on the virtual surface are needed for calculating far-field transformations. Thus, (5.14a) and (5.14b) yield

$$\left[\bar{a}_n \times \bar{H}(\bar{r},\omega)\right]_{spherical} = \bar{a}_\phi H_\theta - \bar{a}_\theta H_\phi \tag{6.5a}$$

and

$$\left[\bar{a}_n \times \bar{E}(\bar{r},\omega)\right]_{spherical} = \bar{a}_\phi E_\theta - \bar{a}_\theta E_\phi . \tag{6.5b}$$

By subsituting (6.5a) and (6.5b) to (5.13a) and rearranging terms, one obtains

$$rE_\theta^r(\bar{r},\omega) = \frac{j\omega\mu_o \Delta S'}{4\pi} \sum_{\substack{entire \\ surface}} \left(H_\phi + \frac{1}{\eta_o} E_\theta \right) \times exp\left(-j\omega t_{delay}\right) \tag{6.6a}$$

and

$$rE_\phi^r(\bar{r},\omega) = \frac{j\omega\mu_o \Delta S'}{4\pi} \sum_{\substack{entire \\ surface}} \left(-H_\theta + \frac{1}{\eta_o} E_\phi \right) \times exp\left(-j\omega t_{delay}\right). \tag{6.6b}$$

It should be noted again that the tangential field components, E_θ, E_ϕ, H_θ and H_ϕ, are in frequency domain. Thus, the recursive DFT (5.16b) is used while the FD-TD simulation is running. Then, (6.6a) and (6.6b) are applied to obtain far-field responses, after the FD-TD simulation has finished. For the TD-NFFF, the procedures that have been discussed in sub-section 5.3.2 are similarly used. In addition to the recursive DFT procedure, the time-discretized tangential field components, E_θ, E_ϕ, H_θ and H_ϕ, must be calculated at the same point on each of the discretized patch. Thus, the averages of fields are required as follows:

$$E_\theta{}^n = \frac{1}{2}\left[E_\theta(I_v,j,k)^n + E_\theta(I_v,j,k+1)^n\right], \tag{6.7a}$$

$$E_\phi{}^n = \frac{1}{2}\left[E_\phi(I_v,j,k)^n + E_\phi(I_v,j+1,k)^n\right], \tag{6.7b}$$

$$H_\theta{}^n = \frac{1}{4}\left[H_\theta(I_v-1,j,k)^n + H_\theta(I_v,j,k)^n + H_\theta(I_v-1,j+1,k)^n + H_\theta(I_v-1,j+1,k)^n\right], \tag{6.7c}$$

$$H_{\phi\theta}{}^n = \frac{1}{4}\left[H_\phi(I_v-1,j,k)^n + H_\phi(I_v,j,k)^n + H_\phi(I_v-1,j,k+1)^n + H_\phi(I_v-1,j,k+1)^n\right], \tag{6.7d}$$

where I_v indicates that the index 'i' is at the virtual surface.

As introduced at the preliminary part of this chapter, there are four antenna characteristic parameters being discussed, here. The first one is the input impedance, which can be calculated by taking the ratio of frequency-domain voltage and frequency-domain current as

$$Z(\omega) = \frac{V(\omega)}{I(\omega)}. \tag{6.8a}$$

The recursive DFT is applied again to achieve the frequency-domain current on the probe's surface, this yields

$$I(\omega)+I(n\Delta t)\times e^{(-j\omega n\Delta t)} \rightarrow I(\omega), \tag{6.8b}$$

where $I(n\Delta t)$ is the discretized time-domain current at time step n. For the conical probe model, $I(n\Delta t)$ is determined by summing the H_ϕ field components around the probe model (Ampere's law (5.9)), given by

$$I(n\Delta t)=\frac{\Delta r}{2}sin\left(\frac{\Delta\theta}{2}\right)\Delta\phi\sum_{k=1}^{K_{max}}H_\phi(1,J_{max}-1,k)^n . \tag{6.8c}$$

In the similar manner, the recursive DFT for the applied voltage source is defined by

$$V(\omega)+V(n\Delta t)\times e^{(-j\omega n\Delta t)} \rightarrow V(\omega), \tag{6.8d}$$

where $V(n\Delta t)$ is the discretized time-domain voltage at time step n. To obtain the second antenna parameter, radiation pattern, a far-field distance r is determined and substituted into (6.6a) and (6.6b). When an antenna structure is excited by a pulse waveform, the broadband gain of the antenna model can be obtained. The definitions of the braodband gains are defined [11], separately, in θ and ϕ directions,

$$G_\theta(\omega)=\frac{4\pi\left|rE_\theta^r(\omega)\right|^2}{2\eta_o P_{ant}(\omega)}, \tag{6.9a}$$

$$G_\phi(\omega)=\frac{4\pi\left|rE_\phi^r(\omega)\right|^2}{2\eta_o P_{ant}(\omega)}, \tag{6.9b}$$

where $P_{ant}(\omega)$ is the net power that enter the feeding point (input) of the antenna. The net power $P_{ant}(\omega)$ can be determined from the incident (input) voltage, $V_{inc}(\omega)$, and the reflected voltage, $V_{refl}(\omega)$, as follows:

$$P_{ant}(\omega)=\left|V_{inc}(\omega)\right|^2\left(1-\left|\Gamma(\omega)\right|^2\right)/2Z_o , \tag{6.9c}$$

where

$$\Gamma(\omega)=V_{refl}(\omega)/V_{inc}(\omega). \tag{6.9d}$$

The DFT is used again to obtain the above frequency-domain parameters. As the last antenna parameter considered here, the directivity can be computed by a numerical method. The definition of the directivity is given [38]

$$D_o=\frac{4\pi U_{max}}{P_{rad}}, \tag{6.10a}$$

where U_{max} is the maximum radiation intensity, which can be approximately calculated from the far-zone field as follows:

$$U(\theta,\phi)_{max} \approx \frac{r^2}{2\eta}\left(\left|E_\theta^r(\theta,\phi)\right|_{max}^2 + \left|E_\phi^r(\theta,\phi)\right|_{max}^2\right). \tag{6.10b}$$

The numerical formular of the radiated power P_{rad} is

$$P_{rad} = \left(\frac{\pi}{J_{max}}\right)\left(\frac{2\pi}{K_{max}}\right)\sum_{k=1}^{K_{max}}\sum_{j=1}^{J_{max}}\left[U(\theta_j,\phi_k)sin(\theta_j)\right], \tag{6.10c}$$

where θ_j, ϕ_k are defined as follows:

$$\left.\begin{aligned}\theta_j &= \frac{\pi}{2J_{max}} + (j-1)\frac{\pi}{J_{max}}, \quad j = 1,2,3,...,J_{max} \\ \phi_k &= \frac{\pi}{2K_{max}} + (k-1)\frac{\pi}{K_{max}}, \quad k = 1,2,3,...,K_{max}\end{aligned}\right\}, \tag{6.10d}$$

and $U(\theta_j,\phi_k)$ is the discretized radiation intensity, given by

$$U(\theta_j,\phi_k) \approx \frac{r^2}{2\eta}\left(\left|E_\theta^r(\theta_j,\phi_k)\right|^2 + \left|E_\phi^r(\theta_j,\phi_k)\right|^2\right). \tag{6.10e}$$

6.3 Numerical Results

By implementing the FD-TD antenna model of the previous section and analyzing, results of two antenna parameters are shown here, which are the input impedance and radiation pattern. The 4-slot antenna model is analyzed by varying the slot elevation-angle θ_s and the probe length R_f. The slot elevation-angle θ_s is varied from $30°$ to $60°$ with $15°$ increment. The probe length R_f is varied from *1.40* cm to *5.16* cm with *0.94*-cm approximate increment, to get the probe lengths that conform well to the radial increment Δr. The CPU time required for processing the FD-TD calculations, for each value of R_f or θ_s, is about *45* minutes on the Pentium *133* MHz personal computer with *16* MB random access memory.

After analyzing the antenna model by varying R_f and θ_s, the results of the input resistance and reactance at the operating frequency are gathered and shown in Fig.6.4(a) and Fig.6.4(b), respectively. All of the curves are constructed by using the second-order polynomial interpolation ($a_2 \cdot x^2 + a_1 \cdot x + a_0$) from the three-point data at $\theta_s = 30°$, $45°$ and $60°$. From the figures, it is evident that both the input resistance and reactance are increased when the probe length are extended. Also, it is found that when the slot angle θ_s is increased the input resistance and reactance are decreased. Moreover, the figures show that the input resistance and reactance change abruptly when the probe length is longer, and when the slot angle θ_s is smaller.

The radiation pattern results of the antenna model are selected for illustrating, here, only the case when all the antenna dimensional parameters are the same as shown in Table 6.1. The results of the principle E-plane and H-plane are shown in

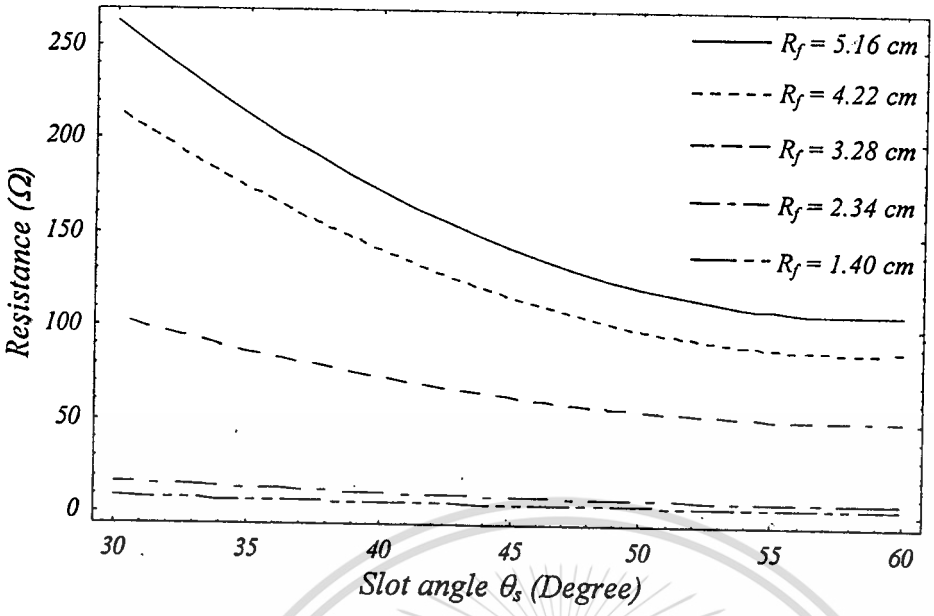

Fig. 6.4(a) Input resistance of the antenna model at the frequency *3.18* GHz as function of probe length R_f and slot elevation-angle θ_s

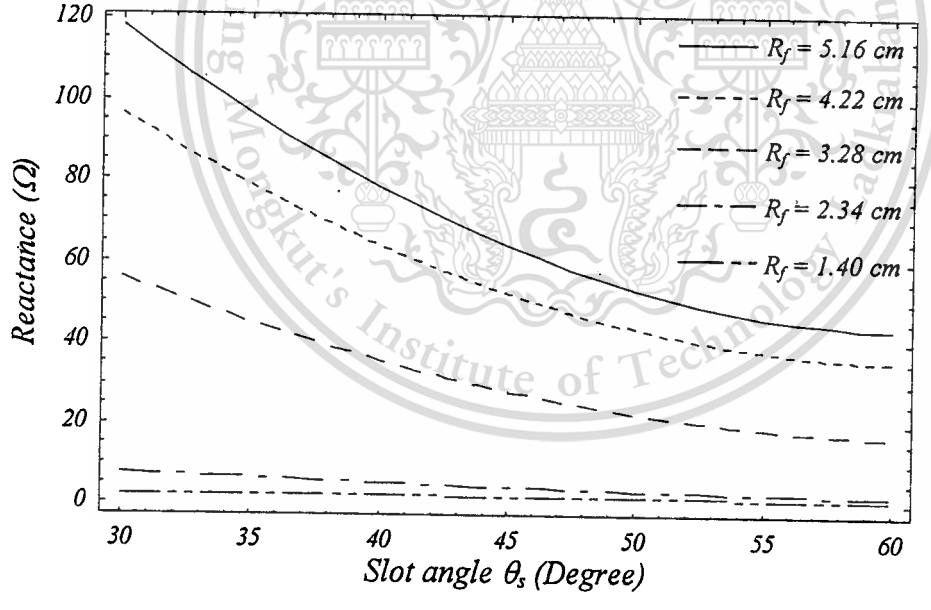

Fig. 6.4(b) Input reactance of the antenna model at the frequency *3.18* GHz as function of probe length R_f and slot elevation-angle θ_s

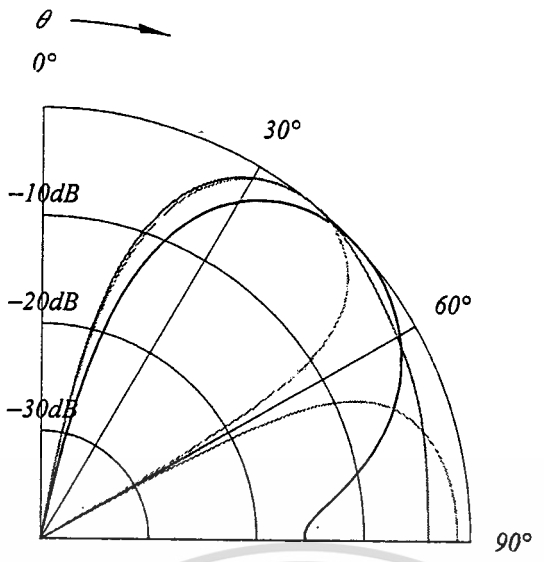

Fig. 6.5(a) E-plane radiation patterns of the antenna model:
—— at frequency of *2.68* GHz
—— at frequency of *3.18* GHz
—— at frequency of *3.68* GHz

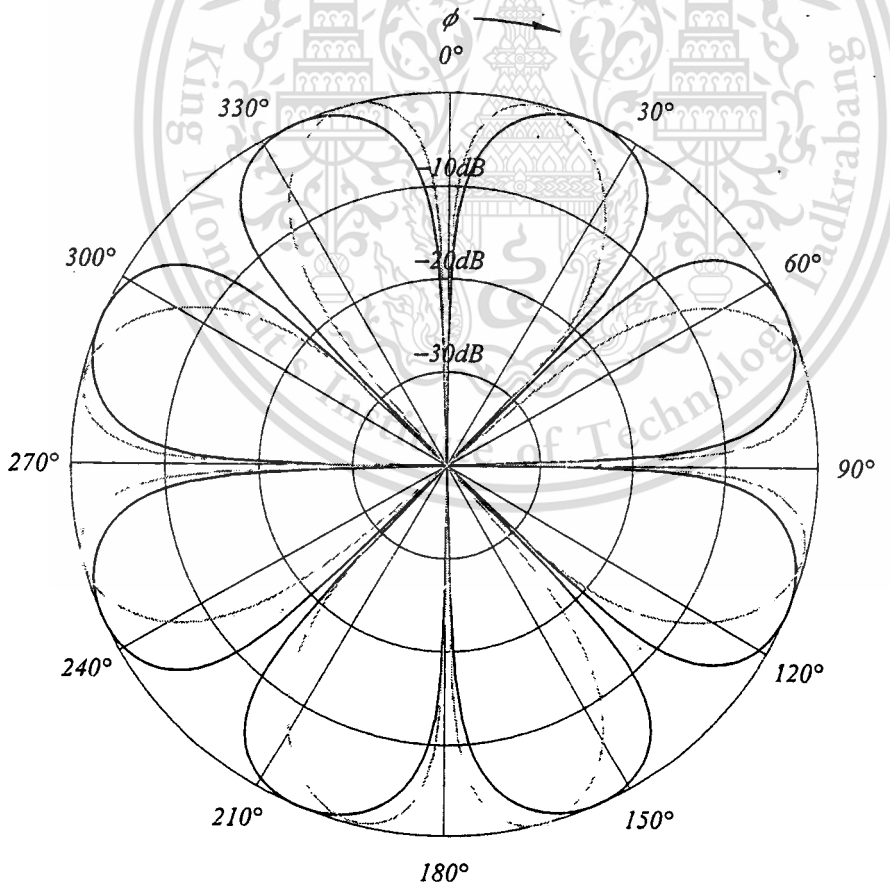

Fig. 6.5(b) H-plane radiation patterns of the antenna model:
—— at frequency of *2.68* GHz
····· at frequency of *3.18* GHz
—— at frequency of *3.68* GHz

Fig.6.5(a) and Fig.6.5(b), respectively. From the figures, it is seen that the E-plane radiation patterns change significantly when the frequencies change, while the H-plane radiation patterns only slightly change.

6.4 Experimental Results

To verify the principle of the FD-TD method for applying to the antenna using the slotted hemispherical cavity, the antenna was fabricated, as shown in Fig.6.6, to operate at the frequency of *3.18* GHz (available equipment). The fabricated antenna consists of a slot on the surface of the hemispherical cavity of the radius *7.50* cm at the angle 45°, the width and length of the slot are *1.89* mm and *4.72* cm, respectively. The hemispherical cavity covers the circular conductor disk of radius *8.50* cm at the bottom of the cavity ($\theta = 90^{\circ}$). The linear electric probe, made of good conductor (copper), is excited at the center of the cavity. The diameter and the length of the probe are approximately *1.00* mm and *1.40* cm, respectively.

Fig. 6.6 Photograph of the fabricated antenna

For measuring the input impedance of this antenna structure, the antenna was connected to 8720C Vector Network Analyzer via N-type connector. The experimental results of input resistance and reactance are illustrated in the same graph of the numerical ones as shown in Fig.6.7(a) and Fig.6.7(b), respectively. From the compared results, it is apparent that these two results are in the same trend, both the resistance and the reactance. At the operating frequency of *3.18* GHz, the measured result of input impedance is $0.871\Omega - j2.068\Omega$. The shifted values between numerical and experimental results about 4Ω is observed. It is also evident that for the resistance characteristic, the experimental results possess lower sensitive to the frequency than that of the reactance characteristic. This might be due to the consideration of perfect conductor assumption in calculation of the probe material. Accordingly, the imperfectness of the conductor material is not taken into account in the calculation; therefore, the calculated results of reactance seem to be smoother than that one expected. Additionally, there are some other errors occurred because the approximations of the integral equations in calculating the magnetic fields near the probe model and the fields near the singular points, and the simplifications of the fields in and near the slot model in addition to the neglect of the cavity thickness in the FD-TD calculation. However, from the consequence of these compared results, it

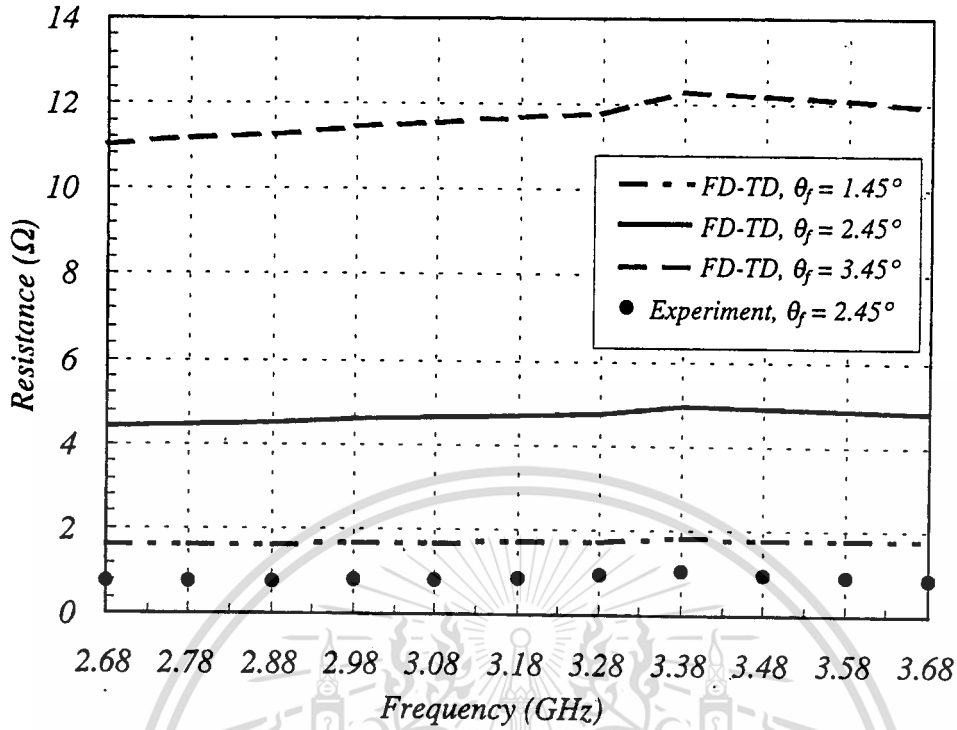

Fig. 6.7(a) Comparison of numerical and experimental input resistance results, $R_f = 1.40$ cm

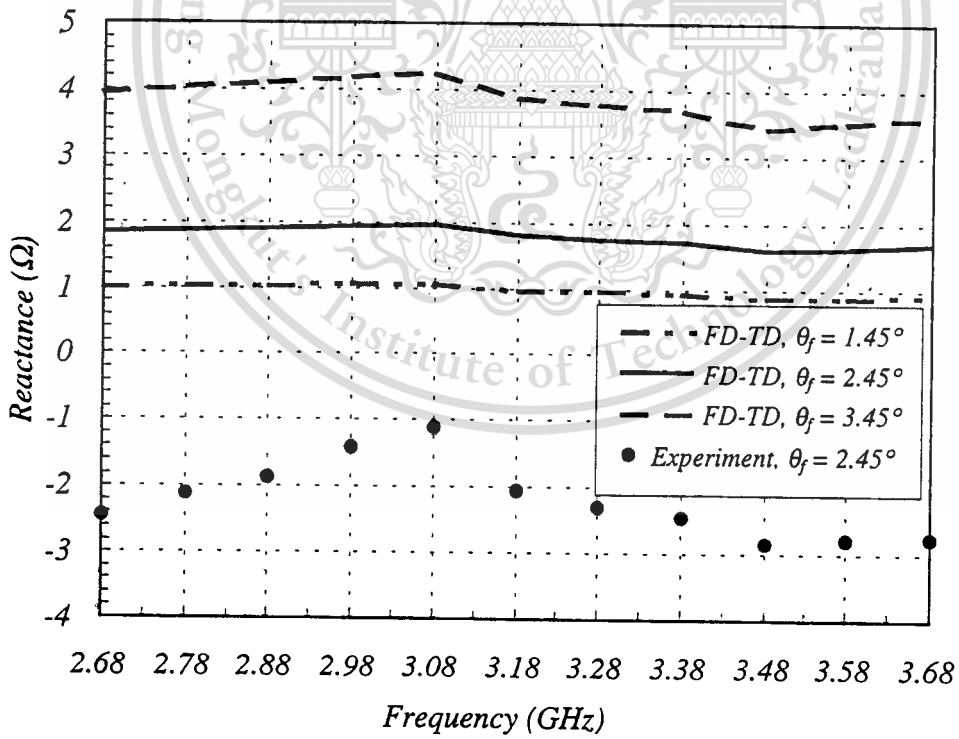

Fig. 6.7(b) Comparison of numerical and experimental input reactance results, $R_f = 1.40$ cm

can confirm that the proposed principle can be applied to the antenna using the slotted hemispherical cavity. Also shown in Fig.6.7(a) and Fig.6.7(b), the numerical input resistance and reactance results of the antenna model when the probe's half-cone angle is adjusted to get the closer results to the expermental ones. It can be concluded that when the half-cone angle is smaller ($\theta_f = 1.45°$), the results get closer to the experimental ones.

6.5 Conclusions

In this chapter, the slotted hemispherical antenna is considered and analyzed by using the FD-TD algorithm in spherical coordinates. All the details of antenna modeling using the derived FD-TD agorithm are discussed thoroughly. The first discussion is about discretizing the FD-TD solution region to fit to the antenna model. The second point, the feeding algorithm, magnetic frill, at the base of the probe model is illustrated. Also, two pulse waveforms for antenna excitations are introduced to efficiently analyze the broadband responses of the antenna. Additionally, an alternate convenient scheme, the first-order Bayliss-Turkel RBC, is briefly derived and used as the radiation condition at the outermost surface of the problem space. The equations for obtaining the far-field responses, from the tengential fields on the spherical virtual surface having the reference point at the origin, is also given. Details and formulas for atenna parameter computations are discussed, consisting of impedance, broadband gain, radiation pattern and directivity. In case of the impedance calculation, numerical results are compared with the experimental results. The results are in good agreement. Then, additional FD-TD results are illustrated in many cases, such as with and without ground plane, varying probe length, slot number and positions. The results show behaviors of the antenna when these parameters have been changed.

Chapter 7

Discussions and Conclusions

In this chapter, all the main knowledges obtained in the preceeding chapters are summarized. Finally, the discussions of future studies are presented.

7.1 Summary of the Preceeding Chapters

As mentioned in chapter 1, this thesis involves deriving of the FD-TD algorithm in spherical coordinates. The derived FD-TD algorithm, probe and slot models are applied to analyze an antenna model of spherical geometry. The slotted hemispherical antenna is selected as the model under test.

The discussed materials in chapter 2 are about the basis of general finite-difference schemes, different types of errors and a stability criterion. Also, the FD-TD in rectangular coordinates is reviewed and analyzed about the stability criterion and numerical dispersion. By using the similar procedures in deriving the FD-TD in rectangular coordinates, the FD-TD algorithm in spherical coordinates can be derived in chapter 3. The stability criterion of spherical coordinates is obtained by using the derived stabilty criterion in general curvilinear coordinates. There are two easy-to-implement RBC's introduced, second-order extrapolation and linear interpolation. Finally, the numerical tests of the FD-TD algorithm in spherical coordinates are done for problems involving the known-solution electric and magnetic dipoles. Good results are obtained. In chapter 4, the derived FD-TD algorithm is applied to simulate field inside three configurations of cavities: (1) a conducting spherical segmented cavity, (2) a concentric conducting spherical cavity enclosed by a conducting conical surface and (3) a conducting spherical cavity. The derivations of mathematical porbe and slot models are discussed in chapter 5. There are two types of modeling that have been considered, detailed (fine) and approximate models. It is found that the detailed models are simple, but the cost constraints grow excessively when the resolution is increased. Instead, the approximate models are prefered if the costs are excessive. However, the approximate models are more difficult to obtain, and risk of severe modeling errors. As the last material discusssed in chapter 5, two convenient schemes are introduced to obtain far-field responses, which are the frequency-domain near-to-far field transformation (FD-NFFF) and the time-domain near-to-far field transformation (TD-NFFF). Both schemes of field transformations are used in antenna analyses. In chapter 6, all the knowledge of the previous chapters are integrated to analyze the slotted hemispherical antenna model. There are four antenna parameters considered, input impedance, broadband gain, radiation pattern and directivity. The numerical analysis by using the FD-TD method can be done for many cases, such as varying probe length, increasing or decreasing slot number and/or varying slot positions. Some of the numerical and experimental results are selected to present in this thesis.

7.2 Ramark for Future Studies

There are three points in the presented works that can degrade the accuracy of the FD-TD simulation. First, the hemispherical cavity, the approximate probe and slot models are assumed to be perfect conductors, which produce some unrealized effects in numerical calculations. For example, the simulation of wave resonanting in the perfect conducting cavity model yeilds strong resonance, i.e. fields inside the cavity grow abruptly and yield the near-to-infinity quality factor. The second area of

the future studies, the RBC's that presented in this research still have some non-physical reflections back into the solution regions, thus this limits the maximum time steps in the FD-TD calculations. If the maximum time step is taken to be too long, the accumulated or late-time reflections can degrade the numerical results. Presently, there is the theoritical ABC called *uniaxial perfectly match layer* (*UPML*) [1], which can be implemented for spherical coordinates. However, todate, no numerical results in using the UPML in spherical coordinates has been conducted. Moreover, the time-domain closed form of the UPML in spherical coordinates can be determined only when the absorption in the radial direction is considered. If the absorption in θ- and ϕ- directions are to be implemented, the discretized time-convolutions are required. As mentioned in the preceeding chapters, all field components of the integral equations, (3.9a) through (3.11b), are assumed the be constant over their integrating surfaces and paths, thus this results in modeling errors. Although the errors can be reduced by increasing the FD-TD resolution, specifically, this choice is inconvenient for the FD-TD algorithm in spherical coordinates. The study of behaviors of fields near the singular points can be utilized to obtain more efficient near-field physical assumptions, which may provide better results.

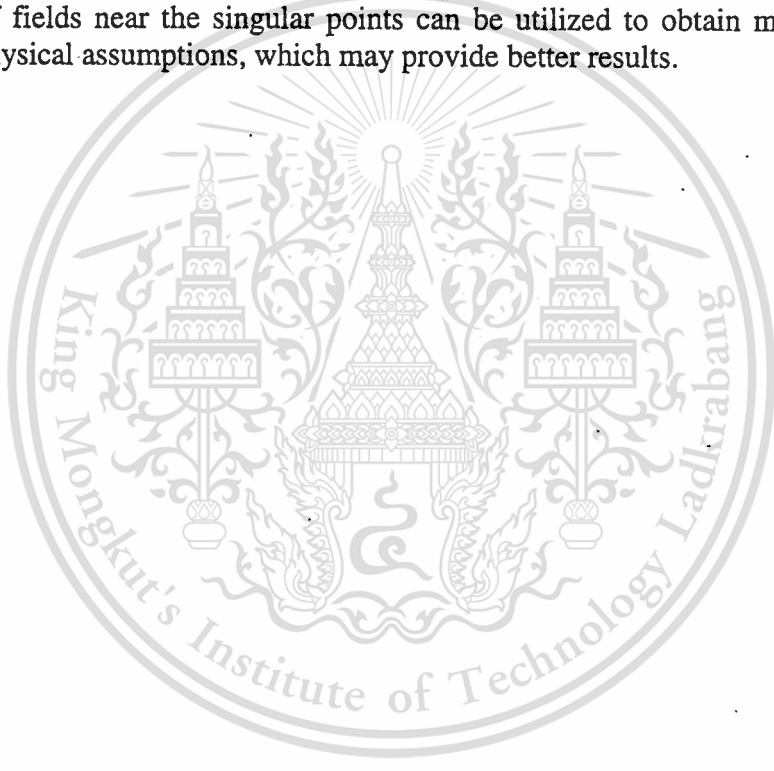

REFERENCES

[1] Yee K.S. "Numerical solution of initial boundary value problems involving Maxwell's equations in isotropic media." IEEE Trans. Antennas Propagat., vol. 14, May 1966. pp. 302-307.

[2] Taflove A. and Brodwin M.E. "Numerical solution of steady-state electromagnetic scattering problems using the time-dependent Maxwell's equations." IEEE Trans. Microwave Theory Tech., vol. 23, Aug. 1975. pp. 623-630.

[3] Taflove A., Umashankar K.R., Beker B., Hartoush F. and Yee K.S. "Detailed FD-TD analysis of electromagnetic fields penetrating narrow slot and laped joints in thick conducting screens," IEEE Trans. Antennas Propagat., vol. 36, Feb. 1988. pp. 247-257.

[4] Umashankar K.R., Taflove A. and Beker B. "Calculation and experimental validation of induced currents on coupled wires in an arbitrary shaped cavity." IEEE Trans. Antennas Propagat., vol. 35, Nov. 1987. pp. 1248-1257.

[5] Holland R. "THREDE: A free-field EMP coupling and scattering code." IEEE Trans. Nucl. Sci., vol. 24, Dec. 1977. pp. 2416-2421.

[6] Holland R., Simpson L. and Kunz K.S. "Finite-difference analysis of EMP coupling to lossy dielectric structures." IEEE Trans. Electromagn. Compat., vol. 22, Aug. 1980. pp. 203-209.

[7] Holland R. "THREDS: A finite-difference time-domain EMP code in 3D spherical coordinates." IEEE Trans. Nucl. Sci., vol. 30, Dec. 1983. pp. 4592-4595.

[8] Olivier J.C. and McNamara D.A. "Finite-difference time-domain (FDTD) analysis of discontinuities in homogeneous, dispersive waveguides." Electron. Lett., vol. 25, July 1989. pp. 1006-1007.

[9] Ko W.L., and Mittra R. "A combination of FDTD and Proney's methods for analyzing microwave integrated circuit." IEEE Trans. Microwave Theory Tech., vol. 39, Dec. 1991. pp. 2176-2181.

[10] Malony J.G., Smith G.S. and Scott W.R. "Accurate computation of the radiation from simple antennas using the finite-difference time-domain method." IEEE Trans. Antennas Propagat., vol. 38, July 1990. pp. 1059-1086.

[11] Taflove A., Editor. **Advances in Computational Electrodynamics: The Finite-Difference Time-Domain Method.** Boston: Artech House, Inc. 1998.

[12] Sadiku M.N.O. **Numerical Techniques in Electromagnetics.** Boca Raton: CRC Press, Inc. 1992.

[13] Taflove A. **Computational Electrodynamics the Finite-Difference Time-Domain Method.** Boston: Artech House, Inc. 1995.

[14] Kunz K.S. and Luebbers R.J. **Finite Difference Time Domain Method for Electromagnetics.** Boca Raton: CRC Press, Inc. 1993.

[15] Berenger J.P. "A perfectly matched layer for the absorption of electromagnetic waves." J. Computational Physics, vol. 114, Oct. 1994. pp. 185-200.

[16] Umashankar K. and Taflove A. "A novel method to analyze electromagnetic scattering of complex objects." IEEE Trans. Electromagn. Compat., vol. 24, Nov. 1982. pp. 397-405.

[17] Luebbers R. J. "Three-dimensional cartesian-mesh finite-difference time-domain codes." IEEE Antenna Propagat. Magazine, vol. 36, Dec. 1994. pp. 66-71.

[18] Fusco M. "FDTD algorithm in curvilinear coordinates." IEEE Trans. Antennas Propagat., vol. 38, Jan. 1990. pp. 76-89.

[19] Fusco M. A., Smith M. V. and Gordon L. W. "A three-dimensional FDTD algorithm in curvilinear coordinates." IEEE Trans. Antennas Propagat., vol. 39, Oct. 1991. pp. 1463-1471.

[20] Zivanovic S. S., Yee K. S. and Mei K. K. "A subgridding method for the time-domain finite-difference method to solve Maxwell's equations." IEEE Trans. Microwave Theory Tech., vol. 39, Mar. 1991. pp. 471-479.

[21] Luebbers R. J., Kunz K. S., Schneider M. and Hunsberger F. "A finite-difference time-domain near zone to far zone transformation." IEEE Trans. Antennas Propagat., vol. 39, Apr. 1991. pp. 429-433.

[22] Aoyagi P. H., Lee J. F. and Mittra R. "A hybrid Yee algorithm/scalar-wave equation approach." IEEE Trans. Microwave Theory Tech., vol. 41, Sep. 1993. pp. 1593-1600.

[23] Joseph R. M. and Taflove A. "FD-TD Maxwell's equations models for nonlinear electrodynamics and optics." IEEE Trans. Antennas Propagat., vol. 45, Mar. 1997. pp. 364-374.

[24] Balanis C. A. **Antenna Theory: Analysis and Design.** New York: John Wiley & Sons, Inc. 1982. pp. 100-103 and 164-169.

[25] Stratton J. A. **Electromagnetic Theory.** New York: McGraw-Hill, Inc. 1941.

[26] Harrington R. F. **Time-Harmonic Electromagnetic Fields.** New York: McGraw-Hill, Inc. 1961.

[27] Balanis C. A. **Advanced Engineering Electromagnetics.** New York: John Wiley & Sons, Inc. 1989.

[28] Phongcharoenpanich C. "Electromagnetic field analysis of the conducting spherical cavity and segment." Master Thesis of Faculty of Engineering, King Mongkut's Institute of Technology Ladkrabang. 1997.

[29] Jarem J. M. "A method of moments analysis and a finite-difference time-domain analysis of a prove-sleeve fed rectangular waveguide cavity." IEEE Trans. Microwave Theory Tech., vol. 39, Mar. 1991. pp. 444-451.

[30] Boonzaaier J. J. and Pistorius C. W. I. "Thin wire dipoles — a finite-difference time-domain approach." Electron. Lett., vol. 26, no. 22, Oct. 1990. pp.1981-1982.

[31] Gilbert J. and Holland R. "Implementation of the thin-slot formalism in the finite-difference EMP code THREDII." IEEE Trans. Nucl. Sci., vol. 28, Dec. 1981. pp. 4269-4274.

[32] Wang B. Z. "Small-hole formalism for the FD-TD simulation of small-hole coupling." IEEE Microwave and Guided Wave Lett., vol. 5, Jan. 1995. pp. 15-17.

[33] Wang B. Z. "Enhanced thin-slot formalism for the FDTD analysis of thin-slot penetration." IEEE Microwave and Guided Wave Lett., vol. 5, May 1995. pp. 142-143.

[34] Luebbers R. J.,Kunz K. S., Schneider M. and Hunsberger F. "A finite-difference time-domain near zone to far zone transformation." IEEE Trans. Antennas Propagat., vol. 39, Apr. 1991. pp. 429-433.

[35] Luebbers R. J., Ryan D. and Beggs J. "A two-dimensional finite-difference time-domain near zone to far zone transformation." IEEE Trans. Antennas Propagat., vol. 40, July 1992. pp. 848-851.

[36] Yee K. S., Ingham D. and Shlager K. "Time-domain extrapolation to the far field based on FDTD calculations." IEEE Trans. Antennas Propagat., vol. 39, Mar. 1991. pp. 410-413.

[37] Shlager K. L. and Smith G. S. "Near-field to near-field transformation for use with FDTD method for use with FDTD method and its application to pulsed antenna problems." Electron. Lett., vol. 30, Aug. 1994. pp. 1262-1264.

[38] Balanis C. A. **Antenna Theory: Analysis and Design.** 2nd Ed. New York: John Wiley & Sons, Inc. 1997.

[39] Teixeira F. L. and Chew W. C. "PML-FDTD in cylindrical and spherical coordinates." IEEE Microwave and Guided Wave Lett., vol. 7, Sept. 1997. pp. 184-186.

APPENDICES

Appendix A

Vector Analysis in Spherical Coordinates

A.1 Vector Transformations Involving Spherical Coordinates

A.1.1 Cylindrical ↔ Spherical

The cylindrical and spherical coordinates are related by

$$\left.\begin{aligned}\rho &= r\sin\theta\\ z &= r\cos\theta\end{aligned}\right\}. \tag{A.1a}$$

The cylindrical-to-spherical transformation of vector components is given by

$$\left.\begin{aligned}A_r &= A_\rho \sin\theta + A_z \cos\theta\\ A_\theta &= A_\rho \cos\theta - A_z \sin\theta\\ A_\phi &= A_\phi\end{aligned}\right\}, \tag{A.1b}$$

or in matrix form by

$$\begin{bmatrix}A_r\\ A_\theta\\ A_\phi\end{bmatrix} = \begin{bmatrix}\sin\theta & 0 & \cos\theta\\ \cos\theta & 0 & -\sin\theta\\ 0 & 1 & 0\end{bmatrix}\begin{bmatrix}A_\rho\\ A_\phi\\ A_z\end{bmatrix}. \tag{A.1c}$$

Thus, the cylindrical-to-spherical transformation matrix is obtained as

$$[A]_{cs} = \begin{bmatrix}\sin\theta & 0 & \cos\theta\\ \cos\theta & 0 & -\sin\theta\\ 0 & 1 & 0\end{bmatrix}. \tag{A.1d}$$

The inverse of the $[A]_{cs}$ matrix yields the reversed transformation matrix, from spherical to cylindrical,

$$[A]_{sc} = \begin{bmatrix}\sin\theta & \cos\theta & 0\\ 0 & 0 & 1\\ \cos\theta & -\sin\theta & 0\end{bmatrix}. \tag{A.2a}$$

Hence, spherical-to-cylindrical transformation is derived as

$$\begin{bmatrix}A_\rho\\ A_\phi\\ A_z\end{bmatrix} = \begin{bmatrix}\sin\theta & \cos\theta & 0\\ 0 & 0 & 1\\ \cos\theta & -\sin\theta & 0\end{bmatrix}\begin{bmatrix}A_r\\ A_\theta\\ A_\phi\end{bmatrix} \tag{A.2b}$$

or

$$\left.\begin{aligned} A_\rho &= A_r \sin\theta + A_\theta \cos\theta \\ A_\phi &= A_\phi \\ A_z &= A_r \cos\theta + A_\theta \sin\theta \end{aligned}\right\}. \tag{A.2c}$$

A.1.2 Rectangular ↔ Spherical

The rectangular and spherical coordinates are related by

$$\left.\begin{aligned} x &= r\sin\theta\cos\phi \\ y &= r\sin\theta\sin\phi \\ z &= r\cos\theta \end{aligned}\right\}, \tag{A.3a}$$

and the rectangular and spherical components by

$$\left.\begin{aligned} A_r &= A_x \sin\theta\cos\phi + A_y \sin\theta\sin\phi + A_z \cos\theta \\ A_\theta &= A_x \cos\theta\cos\phi + A_y \cos\theta\sin\phi - A_z \sin\theta \\ A_\phi &= -A_x \sin\phi + A_y \cos\phi \end{aligned}\right\}. \tag{A.3b}$$

In matrix form, (A.3b) can be written as

$$\begin{bmatrix} A_r \\ A_\theta \\ A_\phi \end{bmatrix} = \begin{bmatrix} \sin\theta\cos\phi & \sin\theta\sin\phi & \cos\theta \\ \cos\theta\cos\phi & \cos\theta\sin\phi & -\sin\theta \\ -\sin\phi & \cos\phi & 0 \end{bmatrix} \begin{bmatrix} A_x \\ A_y \\ A_z \end{bmatrix}. \tag{A.3c}$$

Thus, the rectangular-to-spherical transformation matrix is obtained as

$$[A]_{rs} = \begin{bmatrix} \sin\theta\cos\phi & \sin\theta\sin\phi & \cos\theta \\ \cos\theta\cos\phi & \cos\theta\sin\phi & -\sin\theta \\ -\sin\phi & \cos\phi & 0 \end{bmatrix}. \tag{A.3d}$$

The inverse of the above matrix can be written as

$$[A]_{sr} = \begin{bmatrix} \sin\theta\cos\phi & \cos\theta\cos\phi & -\sin\phi \\ \sin\theta\sin\phi & \cos\theta\sin\phi & \cos\phi \\ \cos\theta & -\sin\theta & 0 \end{bmatrix}, \tag{A.4a}$$

which yields the reverse tranformation from spherical to rectangular coordinates, or

$$\begin{bmatrix} A_x \\ A_y \\ A_z \end{bmatrix} = \begin{bmatrix} \sin\theta\cos\phi & \cos\theta\cos\phi & -\sin\phi \\ \sin\theta\sin\phi & \cos\theta\sin\phi & \cos\phi \\ \cos\theta & -\sin\theta & 0 \end{bmatrix} \begin{bmatrix} A_r \\ A_\theta \\ A_\phi \end{bmatrix}. \tag{A.4b}$$

The above equation can be written in vector components form as

$$\left.\begin{aligned} A_x &= A_r \sin\theta\cos\phi + A_\theta \cos\theta\cos\phi + A_\phi \sin\phi \\ A_y &= A_r \sin\theta\sin\phi + A_\theta \cos\theta\sin\phi - A_\phi \cos\phi \\ A_z &= -A_r \cos\theta + A_\theta \sin\theta \end{aligned}\right\}. \tag{A.4c}$$

A.2 Vector Operations in Spherical Coordinates

Gradient: ∇

$$\nabla\psi = \hat{a}_r \frac{\partial\psi}{\partial r} - \hat{a}_\theta \frac{1}{r}\frac{\partial\psi}{\partial\theta} + \hat{a}_\phi \frac{1}{r\sin\theta}\frac{\partial\psi}{\partial\phi} \tag{A.5}$$

Divergence: $\nabla\cdot$

$$\nabla\cdot\overline{A} = \frac{1}{r^2}\frac{\partial}{\partial r}\left(r^2 A_r\right) + \frac{1}{r\sin\theta}\frac{\partial}{\partial\theta}\left(A_\theta \sin\theta\right) + \frac{1}{r\sin\theta}\frac{\partial A_\phi}{\partial\phi} \tag{A.6}$$

Curl: $\nabla\times$

$$\begin{aligned} \nabla\times\overline{A} = &\frac{\hat{a}_r}{r\sin\theta}\left[\frac{\partial}{\partial\theta}\left(A_\phi \sin\theta\right) - \frac{\partial A_\theta}{\partial\phi}\right] \\ &+ \frac{\hat{a}_\theta}{r}\left[\frac{1}{\sin\theta}\frac{\partial A_r}{\partial\phi} - \frac{\partial}{\partial r}\left(rA_\phi\right)\right] \\ &+ \frac{\hat{a}_\phi}{r}\left[\frac{\partial}{\partial r}\left(rA_\theta\right) - \frac{\partial A_r}{\partial\theta}\right] \end{aligned} \tag{A.7}$$

Laplacian: ∇^2

$$\nabla^2\psi = \frac{1}{r^2}\frac{\partial}{\partial r}\left(r^2\frac{\partial\psi}{\partial r}\right) + \frac{1}{r^2\sin\theta}\frac{\partial}{\partial\theta}\left(\sin\theta\frac{\partial\psi}{\partial\theta}\right) + \frac{1}{r^2\sin^2\theta}\frac{\partial^2\psi}{\partial\phi^2} \tag{A.8}$$

Appendix B

Spherical Bessel Functions

One set of the Bessel and Hankel functions which are refered to as the ordinary spherical Bessel and Hankel functions are satisfied the ordinary spherical Bessel's differential equation

$$\frac{d^2}{dx^2}[xb_n(x)]+\left[1-\frac{n(n+1)}{x^2}\right]xb_n(x)=0, \tag{B.1}$$

where $b_n(x)$ can be any of the following functions,

$j_n(x)$; ordinary spherical Bessel function of the first kind of order n,

$y_n(x)$, ordinary spherical Bessel function of the second kind of order n,

$h_n^{(1)}(x)$; ordinary spherical Hankel function of the first kind of order n

and $h_n^{(2)}(x)$ ordinary spherical Hankel function of the second kind of order n.

The ordinary spherical Bessel and Hankel functions are related to the regular (cylindrical) Bessel function as

$$b_n(x)=\sqrt{\frac{\pi}{2x}}B_{n+1/2}(x), \tag{B.2}$$

where $B_n(x)$ is the regular Bessel function of order n.

Another set of the Bessel and Hankel functions which are usually used in determining the electromagnetic field in the spherical geometry are refered to as the Schelkunoff spherical Bessel and Hankel functions are satisfied the Schelkunoff spherical Bessel's differential equation

$$\frac{1}{\tilde{B}_n(x)}\left[x^2\frac{d^2\tilde{B}_n(x)}{dx^2}\right]+x^2-n(n+1)=0, \tag{B.3}$$

where $\tilde{B}_n(x)$ are

$\tilde{J}_n(x)$: Schelkunoff spherical Bessel function of the first kind of order n,

$\tilde{Y}_n(x)$: Schelkunoff spherical Bessel function of the second kind of order n,

$\tilde{H}_n^{(1)}(x)$: Schelkunoff spherical Hankel function of the first kind of order n

and $\tilde{H}_n^{(2)}(x)$: Schelkunoff spherical Hankel function of the second kind of order n.

The Schelkunoff spherical Bessel and Hankel functions are related to the regular Bessel function and the ordinary spherical Bessel function as

$$\tilde{B}_n(x)=\sqrt{\frac{\pi x}{2}}B_{n+1/2}(x)=xb_n(x), \tag{B.4}$$

Appendix C

Associated Legendre Functions

Associated Legendre functions are the function which satisfied the associated Legendre's differential equation as

$$(1-x^2)\frac{d^2L_n^m(x)}{dx^2}-2x\frac{dL_n^m(x)}{dx}+\left[n(n+1)-\frac{m^2}{1-x^2}\right]L_n^m(x)=0, \qquad \text{(C.1)}$$

where the solution $L_n^m(x)$ is

$$L_n^m(x)=A_1P_n^m(x)+B_1Q_n^m(x). \qquad \text{(C.2)}$$

In (C.2), $P_n^m(x)$ is the associated Legendre function of the first kind of order (n,m), and $Q_n^m(x)$ is the associated Legendre function of the second kind of order (n,m).

The relationship between the associated Legendre function and the ordinary Legendre function is defined by

$$L_n^m(x)=(-1)^m(1-x^2)^{m/2}\frac{d^mL_n(x)}{dx^m}, \qquad \text{(C.3)}$$

where $L_n(x)$ can be either $P_n(x)$; ordinary Legendre function of the first kind of order n and $Q_n(x)$; the ordinary Legendre function of the second kind of order n.

Appendix D

Derivations of the Stability Criterion and Numerical Dispersion

D.1 Stability

Consider a system satisfying

$$\frac{d\bar{u}}{dt} = L\bar{u}\,, \tag{D.1a}$$

where L is a spatial differential operator and $\bar{u}(r,t)$ is the state vector know at time $t = 0$ (i.e. $\bar{u}(r,0)=\bar{u}_0$), so the equation is an initial value equation. In difference from this can be written

$$\bar{u}^{n+1} = T(\Delta t, \Delta x)\bar{u}^n \tag{D.1b}$$

or

$$\bar{u}^{n+1} = \bar{u}^n + \int_{t^n}^{t^{n+1}} L\bar{u}\,dt' \tag{D.1c}$$

or using a Taylor series expansion

$$\begin{aligned} RHS &= \bar{u}^n + \int_{t^n}^{t^{n+1}} \left\{ \sum_{r=0}^{p-1} \left[\frac{d^r}{dt^r}(L\bar{u}) \right]_{t^n} \frac{t'^r}{r!} + O(t'^p) \right\} dr' \\ &\approx \bar{u}^n + L\bar{u}\Delta t = (I + \Delta t L)\bar{u}^n \equiv T(\Delta t, \Delta x)\bar{u}^n \end{aligned}, \tag{D.1d}$$

where I is the unitary matrix. The final result is the expression for an explicit difference scheme.

Now assume a system where linear superposition. Solutions can be expressed in terms of Fourier modes, for compactness position is given by x_j rather than $x(J)$,

$$\bar{u}_j^n = \hat{u}^n e^{ikx_j}\,. \tag{D.2a}$$

By substitution (D.2a) into (D.1b), the result is

$$\hat{u}^{n+1} e^{ikx_j} = T(\Delta t, \Delta x)\hat{u}^n e^{ikx_j} \tag{D.2b}$$

or

$$\hat{u}^{n+1} = e^{-ikx_j} T(\Delta t, \Delta x)\hat{u}^n e^{ikx_j} \hat{u}^n = G(\Delta t, \Delta x)\hat{u}^n\,, \tag{D.2c}$$

where G is the amplification matrix of the difference scheme for the Fourier mode of wave number k.

The Fourier modes can be expressed as an expansion in the eigenvectors of the amplification matrix G. In particular let $\hat{u}_\mu^o$ be the amplitude of the vector Fourier mode along the eigenvector $\bar{S}^{(\mu)}$ at time step zero, then

$$\hat{u}^o = \sum_\mu \hat{u}^o_\mu \bar{S}^{(\mu)} \tag{D.3a}$$

From $\hat{u}^o$ and (D.2c), one can find $\hat{u}^n$ as

$$\hat{u}^n = (G)^n \hat{u}^o = (G)^n \sum_\mu \hat{u}^o_\mu \bar{S}^{(\mu)} \tag{D.3b}$$

Now $\bar{S}^{(\mu)}$ as an eigenvector of G satisfies

$$(G - g_\mu) S^{(\mu)} = 0 \text{ or } GS^{(\mu)} = g_\mu S^{(\mu)} \tag{D.3c}$$

Thus, from (D.3b)

$$\hat{u}^n = \sum \hat{u}^o_\mu (g_\mu)^n S^{(\mu)} \tag{D.3d}$$

For $|g_\mu| \le 1$ this behavior for $\hat{u}^n$ is stable. Equivalently, it is required that

$$g^*_\mu g_\mu = |g_\mu|^2 \le 1 \tag{D.4}$$

Now, the time centered leapfrog method is being recasted into a form with G, finding the g_μ and determining under what conditions that yield $|g_\mu| < 1$.

The difference equations in 1-D are of the form

$$u_j^{n+1/2} = u_j^{n-1/2} - \frac{\Delta t}{\Delta x}\left(f^n_{j+1} - f^n_{j-1}\right) \tag{D.5a}$$

or

$$E_j^{n+1/2} = E_j^{n-1/2} - \frac{\Delta t}{\varepsilon \Delta x}\left(H^n_{j+1/2} - H^n_{j-1/2}\right) \text{from} \left(\frac{\partial D}{\partial t} + \frac{\partial H}{\partial x}\right) = 0, \tag{D.5b}$$

$$H_{j+1/2}^n = H_{j+1/2}^{n-1} - \frac{\Delta t}{\mu \Delta x}\left(E^{n-1/2}_{j+1} - E_j^{n-1/2}\right) \text{from} \left(\frac{\partial B}{\partial t} + \frac{\partial E}{\partial x}\right) = 0. \tag{D.5c}$$

By substituting (17.6) into (17.5) and rearranging, one obtains

$$E_j^{n+1/2} = E_j^{n-1/2} + \left(\frac{v\Delta t}{\Delta x}\right)^2 \left(E^{n-1/2}_{j+1} - 2E_j^{n-1/2} + E^{n-1/2}_{j-1}\right) - \frac{\Delta t}{\varepsilon \Delta x}\left(H^{n-1}_{j+1/2} - H^{n-1}_{j-1/2}\right), \tag{D.5d}$$

$$H_{j+1/2}^n = H_{j+1/2}^{n-1} - \frac{\Delta t}{\mu \Delta x}\left(E^{n-1/2}_{j+1} - E_j^{n-1/2}\right). \tag{D.5e}$$

Now let

$$\hat{u}^n = \begin{pmatrix} \hat{E}^{n-1/2} e^{ikx} \\ \hat{H}^{n-1} e^{ik(x+\Delta x/2)} \end{pmatrix}. \tag{D.6a}$$

Hence, $\hat{u}^{n+1} = G\hat{u}^n$ can be written as

$$\hat{u}^{n+1} = \begin{bmatrix} 1 + \left(\frac{v\Delta t}{\Delta x}\right)\left(e^{ik\Delta x} - 2 + e^{-ik\Delta x}\right) & -\frac{\Delta t}{\varepsilon \Delta x}\left(1 - e^{-ik\Delta x}\right) \\ -\frac{\Delta t}{\mu \Delta x}\left(e^{-ik\Delta x} - 1\right) & 1 \end{bmatrix} \hat{u}^n \tag{D.6b}$$

where the following equation have been used

$$\left.\begin{aligned} E_{j+1}^{n-1/2} - E_j^{n-1/2} &= \left(\hat{E}^{n-1/2} e^{ikx_j}\right) \cdot \left(e^{ik\Delta x} - 1\right) \\ E_{j+1}^{n-1/2} - 2E_j^{n-1/2} + E_{j-1}^{n-1/2} &= \left(\hat{E}^{n-1/2} e^{ikx_j}\right) \cdot \left(e^{ik\Delta x} - 2 + e^{-ik\Delta x}\right) \end{aligned}\right\}. \tag{D.6c}$$

Thus, the eigenvalues of (D.3c) may be found from the determinant of $|G - g|$, by setting the determinant to zero so that

$$\begin{aligned} &\left\{\left[1 + \left(\frac{v\Delta t}{\Delta x}\right)\right]^2 \left(e^{ik\Delta x} - 2 + e^{-ik\Delta x}\right) - g\right\} \cdot (1 - g) \\ &- \left(\frac{v\Delta t}{\Delta x}\right)^2 \left(e^{ik\Delta x} - 2 + e^{-ik\Delta x}\right) = 0 \end{aligned}, \tag{D.6d}$$

this simplifies to

$$g^2 - \left[2t\left(\frac{v\Delta t}{\Delta x}\right)^2 \left(e^{ik\Delta x} - 2 + e^{-ik\Delta x}\right)\right] g + 1 = 0. \tag{D.6e}$$

For $(v\Delta t)/(\Delta x) = 1$ or equivalently $\Delta t = \Delta x/v$ the expression further simplifies to

$$g^2 - 2(\cos k\Delta x)g + 1 = 0 \tag{D.6f}$$

and

$$\begin{aligned} g &= \frac{2(\cos k\Delta x) \pm \sqrt{4\cos^2 k\Delta x - 4}}{2} \\ &= \cos k\Delta x \pm \sqrt{\cos^2 k\Delta x - 1} \\ &= \cos k\Delta x \pm i \sin k\Delta x \end{aligned} \tag{D.6g}$$

Therefore $|g| = 1$ and the scheme is stable for $\Delta t = \Delta x/v$ in 1-D. In 3-D and for cubical cells the stability condition generalizes to $\Delta t = \Delta x/\sqrt{3}v$.

D.2 Numerical Dispersion

Starting with the six free-space finite difference equations,

$$E_x^{n+1/2}(I,J,K) = E_x^{n-1/2}(I,J,K) + \frac{\Delta t}{\varepsilon_0}\left[\frac{H_z^n(I,J,K) - H_z^n(I,J-1,K)}{\Delta y} - \frac{H_y^n(I,J,K) - H_y^n(I,J,K-1)}{\Delta z}\right], \quad \text{(D.7a)}$$

$$E_y^{n+1/2}(I,J,K) = E_y^{n-1/2}(I,J,K) + \frac{\Delta t}{\varepsilon_0}\left[\frac{H_x^n(I,J,K) - H_x^n(I,J,K-1)}{\Delta z} - \frac{H_z^n(I,J,K) - H_z^n(I-1,J,K)}{\Delta x}\right], \quad \text{(D.7b)}$$

$$E_z^{n+1/2}(I,J,K) = E_z^{n-1/2}(I,J,K) + \frac{\Delta t}{\varepsilon_0}\left[\frac{H_y^n(I,J,K) - H_y^n(I-1,J,K)}{\Delta x} - \frac{H_x^n(I,J,K) - H_x^n(I,J-1,K)}{\Delta y}\right], \quad \text{(D.7c)}$$

$$H_x^n(I,J,K) = H_x^{n-1}(I,J,K) + \frac{\Delta t}{\mu_0}\left[\frac{E_y^{n-1/2}(I,J,K+1) - E_y^{n-1/2}(I,J,K)}{\Delta z} - \frac{E_z^{n-1/2}(I,J+1,K) - E_z^{n-1/2}(I,J,K)}{\Delta y}\right], \quad \text{(D.7d)}$$

$$H_y^n(I,J,K) = H_y^{n-1}(I,J,K) + \frac{\Delta t}{\mu_0}\left[\frac{E_z^{n-1/2}(I+1,J,K) - E_z^{n-1/2}(I,J,K)}{\Delta x} - \frac{E_x^{n-1/2}(I,J,K) - E_x^{n-1/2}(I,J,K+1)}{\Delta z}\right], \quad \text{(D.7e)}$$

and

$$H_z^n(I,J,K) = H_z^{n-1}(I,J,K) + \frac{\Delta t}{\mu_0}\left[\frac{E_x^{n-1/2}(I,J+1,K) - E_x^{n-1/2}(I,J,K)}{\Delta y} - \frac{E_y^{n-1/2}(I+1,J,K) - E_y^{n-1/2}(I,J,K)}{\Delta x}\right]. \quad \text{(D.7f)}$$

The Fourier modes for each component of the above equations are

$$E_{x;a,b,c}^{n+1/2}(I,J,K) = e_{x;a,b,c}\, e^{j\{\omega(n+1/2)\Delta t - (a(I+1/2)\Delta x + bJ\Delta y + cK\Delta z)\}}, \quad \text{(D.8a)}$$

$$E_{y;a,b,c}^{n+1/2}(I,J,K) = e_{y;a,b,c}\, e^{j\{\omega(n+1/2)\Delta t - (aI\Delta x + b(J+1/2)\Delta y + cK\Delta z)\}}, \quad \text{(D.8b)}$$

$$E^{n+1/2}_{z;a,b,c}(I,J,K) = e_{z;a,b,c}e^{j\{\omega(n+1/2)\Delta t-(aI\Delta x+bJ\Delta y+c(K+1/2)\Delta z)\}}, \quad \text{(D.8c)}$$

$$H^{n}_{x;a,b,c}(I,J,K) = h_{x;a,b,c}e^{j\{\omega n\Delta t-(aI\Delta x+b(J+1/2)\Delta y+c(K+1/2)\Delta z)\}}, \quad \text{(D.8d)}$$

$$H^{n}_{y;a,b,c}(I,J,K) = h_{y;a,b,c}e^{j\{\omega n\Delta t-(a(I+1/2)\Delta x+bJ\Delta y+c(K+1/2)\Delta z)\}}, \quad \text{(D.8e)}$$

and

$$H^{n}_{z;a,b,c}(I,J,K) = h_{z;a,b,c}e^{j\{\omega n\Delta t-(a(I+1/2)\Delta x+b(J+1/2)\Delta y+cK\Delta z)\}}. \quad \text{(D.8f)}$$

By direct substitution of the appropriate Fourier mode into the six free space finite difference equations, (D.7a) through (D.7f), one obtains the requisite six equations and six unknowns. Further, it will be assumed that $e_{x;a,b,c}$ is given along with *a, b, c*; then the five remaining Fourier mode amplitudes and ω are unknown. After rearranging terms, the six equations are obtained in forms of

$$e_x[2\sin(\omega\Delta t/2)] = \frac{\Delta t}{\varepsilon_0}\left\{h_y\left[\frac{2\sin(c\Delta z/2)}{\Delta z}\right] - h_z\left[\frac{2\sin(b\Delta y/2)}{\Delta y}\right]\right\}, \quad \text{(D.9a)}$$

$$e_y[2\sin(\omega\Delta t/2)] = \frac{\Delta t}{\varepsilon_0}\left\{h_z\left[\frac{2\sin(a\Delta x/2)}{\Delta x}\right] - h_x\left[\frac{2\sin(c\Delta z/2)}{\Delta z}\right]\right\}, \quad \text{(D.9b)}$$

$$e_z[2\sin(\omega\Delta t/2)] = \frac{\Delta t}{\varepsilon_0}\left\{h_x\left[\frac{2\sin(b\Delta y/2)}{\Delta y}\right] - h_y\left[\frac{2\sin(a\Delta x/2)}{\Delta x}\right]\right\}; \quad \text{(D.9c)}$$

$$h_x[2\sin(\omega\Delta t/2)] = \frac{\Delta t}{\mu_0}\left\{e_z\left[\frac{2\sin(b\Delta y/2)}{\Delta y}\right] - e_y\left[\frac{2\sin(c\Delta z/2)}{\Delta z}\right]\right\}, \quad \text{(D.9d)}$$

$$h_y[2\sin(\omega\Delta t/2)] = \frac{\Delta t}{\mu_0}\left\{e_x\left[\frac{2\sin(c\Delta z/2)}{\Delta z}\right] - e_z\left[\frac{2\sin(a\Delta x/2)}{\Delta x}\right]\right\}, \quad \text{(D.9e)}$$

and

$$h_z[2\sin(\omega\Delta t/2)] = \frac{\Delta t}{\mu_0}\left\{e_y\left[\frac{2\sin(a\Delta x/2)}{\Delta x}\right] - e_x\left[\frac{2\sin(b\Delta y/2)}{\Delta y}\right]\right\}. \quad \text{(D.19f)}$$

This set of coupled equations can be solved using conventional linear algebra. A solution requires the determinant to be zero and this condition allows *W* to be found in terms of *a*, *b*, and *c*. Consider some new variables to simplify the derivations as follows:

$$W = \frac{2\sin(\omega\Delta t/2)}{\Delta t}$$
$$A = \frac{2\sin(a\Delta x/2)}{\Delta x}$$
$$B = \frac{2\sin(b\Delta y/2)}{\Delta y} \qquad \text{(D.10a)}$$
$$C = \frac{2\sin(c\Delta z/2)}{\Delta z}$$

Then (D.9a) through (D.9f) can be rewritten in form of matrix equation as

$$\begin{bmatrix} W & 0 & 0 & 0 & -\left[\frac{C}{\varepsilon_0}\right] & \left[\frac{B}{\varepsilon_0}\right] \\ 0 & W & 0 & \left[\frac{C}{\varepsilon_0}\right] & 0 & -\left[\frac{A}{\varepsilon_0}\right] \\ 0 & 0 & W & -\left[\frac{B}{\varepsilon_0}\right] & \left[\frac{A}{\varepsilon_0}\right] & 0 \\ 0 & \left[\frac{C}{\mu_0}\right] & -\left[\frac{B}{\mu_0}\right] & W & 0 & 0 \\ -\left[\frac{C}{\mu_0}\right] & 0 & \left[\frac{A}{\mu_0}\right] & 0 & W & 0 \\ \left[\frac{B}{\mu_0}\right] & -\left[\frac{A}{\mu_0}\right] & 0 & 0 & 0 & W \end{bmatrix} \begin{bmatrix} e_x \\ e_y \\ e_z \\ h_x \\ h_y \\ h_z \end{bmatrix} = 0 \equiv M \qquad \text{(D.10b)}$$

By setting $|M| = 0$ yields

$$W^6 - W^4\left(A^2 + B^2 + C^2\right)/\varepsilon_0\mu_0 = 0 \qquad \text{(D.10c)}$$

or

$$W^2 - \left(A^2 + B^2 + C^2\right)/\varepsilon_0\mu_0 = 0. \qquad \text{(D.10d)}$$

Finally, the numerical dispersion of waves propagating in FD-TD discretized spaces is

$$\left(\frac{2\sin(\omega\Delta t/2)}{\Delta t}\right)^2 = \frac{1}{\varepsilon_0\mu_0}\left[\left(\frac{2\sin(a\Delta x/2)}{\Delta x}\right)^2 + \left(\frac{2\sin(b\Delta y/2)}{\Delta y}\right)^2 + \left(\frac{2\sin(c\Delta z/2)}{\Delta z}\right)^2\right]. \qquad \text{(D.10e)}$$

AUTHOR BIOGRAPHY

Mr.Ekajit Khoomwong was born on September 24th 1974 in Chaiyaphum Province, Thailand. He received the B.Eng. degree from Suranaree University of Technology in Telecommunication Engineering since 1997.

His research interests involve numerical analyses of electromagnetic problems, especially, the finite-difference time-domain (FD-TD) method.